STATUS REPORTS

to the

PAPERMAKING

PROJECT ADVISORY COMMITTEE

VOLUME II

March 25, 1997

INSTITUTE OF PAPER SCIENCE AND TECHNOLOGY

Atlanta, Georgia

ANNUAL RESEARCH REVIEW

PAPERMAKING

VOLUME II

March 25, 1997

February 13, 1997

TO: MEMBERS OF THE PAPERMAKING PROJECT ADVISORY COMMITTEE

Attached for your review are the Status Reports for the projects to be discussed at the Papermaking Project Advisory Committee meeting. The Program Review is scheduled for Tuesday, March 25, 1997, at 8:00 a.m. to 12:00 p.m. and the PAC Committee Meeting will meet from 1:00 p.m. to 5:00 p.m.

Please note that the meeting is being held at the Institute of Paper Science and Technology.

We look forward to seeing you at this time.

Sincerely,

David I. Orloff, Ph.D.
Professor of Engineering & Director
Engineering and Paper Materials Division

DIO/map

Attachments

Institute of Paper Science and Technology, Inc.

500 10th Street, N.W.
Atlanta, GA 30318-5794

Telephone 404-894-5700
FAX# 404-894-IPST (4778)

PAPERMAKING
PROJECT ADVISORY COMMITTEE

IPST Liaison: Dr. David Orloff (404) 894-6649; FAX (404) 894-1496
RAC Liaison: Mr. John Bergin (715) 422-2239; FAX (715) 422-2227

Mr. James Buob *(1998)
Assistant Paper Mill Manager
Temple-Inland Inc.
Post Office Box 816
Silsbee, TX 77656
(409) 276-1411
(409) 276-3296 FAX

Mr. Jack Burke *(1999)
Principle Project Manager
Radian International LLC
1979 Lakeside Parkway
Suite 800
Tucker, GA 30084
(770) 414-4522
(770) 414-4919 FAX

Mr. William O. Burns *(1999)
Director, Manufacturing Technology
James River Corporation
1915 Marathon Avenue
Post Office Box 899
Neenah, WI 54957-0899
(414) 729-8437
(414) 729-8144 FAX

Dr. Partha S. Chaudhuri *(1999)
Senior Scientist, Papermaking
Champion International Corporation
Technical Center
West Nyack Road
West Nyack, NY 10994
(914) 578-7123
(914) 578-7175 FAX

Mr. Karl Christianson *(1998)
General Superintendent
Repap Wisconsin Inc.
433 North Main Street
Kimberly, WI 54136-1490
(414) 788-3511
(414) 788-5368 FAX

Dr. Barry W. Crouse *(1999)
Director, Academic Affairs
Institute of Paper Science and Technology
500 10th Street, NW
Atlanta, GA 30318
(404) 894-5735
(404) 894-4778 FAX

Mr. Frank Cunnane *(1999)
Vice President, Marketing
Asten, Inc.
Asten Press Fabrics, Inc.
Post Office Box 118001
Charleston, SC 29423
(803) 747-7800
(803) 747-3856 FAX

Mr. Marcel Dauth *(1998)
St. Laurent Paperboard Inc.
630 Rene Levesque Blvd, West
Suite 3000
Montreal, Quebec H3B 5C7, CANADA
(514) 864-5108
(514) 861-9559 FAX

Dr. Jack Firkins *(1999)
Manager, Technology Development
Boise Cascade Corporation
Research & Development
4435 North Channel Avenue
Portland, OR 97217-7652
(503) 286-7405
(503) 286-7467 FAX

Mr. William Haskins *(1998)
Market Development Manager
Specialty Minerals Inc.
35 Highland Avenue
Bethlehem, PA 18017
(610) 882-8652
(610) 882-8760 FAX

Dr. Eugene V. Hoefs *(1997) (Vice Chairman)
Senior Research Associate
Appleton Papers Inc.
Post Office Box 359
Appleton, WI 54912-0359
(414) 730-7178
(414) 730-7243 FAX

Mr. George Iverson *(1996)
Supervisor, Papermaking Technology
Eastman Kodak Company
Polymer Processing Division
1669 Lake Avenue
Rochester, NY 14652-3622
(716) 588-3870
(716) 588-2680 FAX

Papermaking PAC (cont.)

Dr. Charles Kramer *(1998)
Director
Albany International Research Company
Post Office Box 9114
Mansfield, MA 02048
(508) 337-9541
(508) 339-4996 FAX

Mr. Joseph P. MacDowell *(1999)
Research Project Supervisor - Coated and Uncoated
P.H. Glatfelter Co.
228 South Main Street
Spring Grove, PA 17362-1000
(717) 225-4711
(717) 225-7454 FAX

Dr. Michael Marziale *(1999)
Technical Assistant to the Wickliffe Mill Manager
Westvaco Corporation
1724 Westvaco Road
Post Office Box 278
Wickliffe, KY 42087-0278
(502) 335-4203
(502) 335-4101 FAX

Dr. Franco Palumbo *(1997)
Riverwood International Corporation
Post Office Box 35800
West Monroe, LA 71294-5800
(318) 362-2000
(318) 362-2133 FAX

Mr. Richard Reese *(1996)
Senior Paper Machine Engineer
Georgia-Pacific Corporation
Post Office Box 105605
133 Peachtree Street, NE
Atlanta, GA 30303-5605
(404) 652-4000
(404) 584-1466 FAX

Mr. John Rogers *(1997)
Technical Director
Sandusky International Inc.
Post Office Box 5012
Sandusky, OH 44870-8012
(419) 626-5340
(419) 626-8674 FAX

Dr. Jay A. Shands *(1997)
Manager, Forming Systems
Beloit Corporation
Rockton Research Center
1165 Prairie Hill Road
Rockton, IL 61072-1595
(608) 364-8501
(608) 364-8600 FAX

Mr. Stephen G. Simmons *(1998)
The Mead Corporation
Mead Central Research
8th & Hickory Streets
Chillicothe, OH 45601-0000
(614) 772-3051
(614) 772-3595 FAX

Mr. Benjamin A. Thorp *(1999)
Vice President, Manufacturing Technology Corporation
Chesapeake Corporation
Post Office Box 2350
1021 East Cary Street
Richmond, VA 23218-2350
(804) 697-1000
(804) 697-1199 FAX

Mr. Louis M. Vance *(1998)
Manufacturer Manager
Weyerhaeuser Company
WTC 2F42
Tacoma, WA 98477
(206) 924-6613
(206) 924-6016 FAX

Mr. Lloyd O. Westling *(1999)
Vice President, Production Planning
Longview Fibre Company
Post Office Box 639
Longview, WA 98632
(360) 425-1550
(360) 578-9304 FAX

Dr. David White *(1997) (Chairman)
Research Associate
Union Camp Corporation
Post Office Box 3301
Princeton, NJ 08543-3301
(609) 896-1200
(609) 844-7366 FAX

PAPERMAKING
PROJECT ADVISORY COMMITTEE

IPST Liaison: Dr. David Orloff (404) 894-6649; FAX (404) 894-1496
RAC Liaison: Mr. John Bergin (715) 422-2239; FAX (715) 422-2227

Dr. Guyton Wilkinson *(1999)
Director, Product & Process Technology
Stone Container Corporation
1979 Lakeside Parkway
Suite 300
Tucker, GA 30084
(770) 621-6725
(770) 621-6733

PAPERMAKING
PROJECT ADVISORY COMMITTEE MEETING

March 25, 1997

Institute of Paper Science and Technology
Atlanta, Georgia

PROGRAM REVIEW AGENDA

Seminar Room

8:00 a.m. - 8:05 a.m.	Opening Remarks and Antitrust Statement		David White
8:05 a.m. - 8:10 a.m.	Welcome from Vice President of Research		Gary Baum
8:10 a.m. - 8:20 a.m.	Overview of IPST Papermaking Research		David Orloff
8:20 a.m. - 8:30 a.m.	Student Research		Barry Crouse
8:30 a.m. - 9:00 a.m.	Project F004	Approach Flow Systems	Xiaodong Wang
9:00 a.m. - 9:10 a.m.	Project F006	Air/Sheet Interactions	Xiaodong Wang
9:10 a.m. - 9:50 a.m.	Project F005	Headbox and Forming Hydrodynamics	Cyrus Aidun
9:50 a.m. - 10:00 a.m.	Break		
10:00 a.m. - 10:30 a.m.	Project F003	Fundamentals of Coating Systems	Cyrus Aidun
10:30 a.m. - 11:00 a.m.	Project F002	Review of Results and Current Work in Web Heating and Pressing of Heated Webs	Tim Patterson
11:00 a.m. - 11:50 a.m.	Project F001	Status of Impulse Drying Commercialization	David Orloff
11:50 a.m. - 12:00 p.m.	Applications of Scanning Laser Microscope		Hiroki Nanko

Seminar Room (Room 114)

12:45 p.m. - 1:45 p.m.	Tour of IRF	D. Orloff, C. Aidun
2:00 p.m. - 6:00 p.m.	Papermaking Committee Discussions	David Orloff

PAPERMAKING
PROJECT ADVISORY COMMITTEE MEETING

March 25, 1997

Institute of Paper Science and Technology
Atlanta, Georgia

COMMITTEE DISCUSSIONS AGENDA

Seminar Room (Room 114)

2:00 p.m. - 2:10 p.m.	Convene - Antitrust statement - New Members - Acceptance of Fall, 1996 minutes - Review of agenda	White
2:10 p.m. - 3:00 p.m.	Subcommittee discussion of projects	By subcommittee
3:00 p.m. - 3:30 p.m.	Approach Flow Systems (F004-Wang)	**Reese**, Thorp, Vance, Crouse
3:30 p.m. - 4:00 p.m.	Runnability (F006-Wang)	**Chaudhuri**, Marziale, Burke, Firkins
4:00 p.m. - 4:30 p.m.	Headbox and Forming Hydrodynamics (F005- Aidun)	**Shands**, Westling, Burns, Dauth
4:30 p.m. - 5:00 p.m.	Fundamentals of Coating Systems (F03-Aidun)	**Simmons**, Hoefs, Haskins
5:00 p.m. - 5:30 p.m.	Web Heating and Pressing of Heated Webs (F002-Patterson)	**Iverson**, Cunnane, MacDowell, Buob
5:30 p.m. - 6:00 p.m.	Impulse Drying (F001- Orloff)	**Kramer**, Rogers, Wilkinson. Palumbo, White

Subcommittee chairs are indicated in underlined bold characters above.

TABLE OF CONTENTS

		Page
Volume I:		
Project F005	Headbox and Forming Hydrodynamics	1
Project F003	Fundamentals of Coating Systems	25
Project F002	Review of Results and Current Work in Web Heating and Pressing of Heated Webs	31
Volume II:		
Project F006	Air/Sheet Interactions	1
Project F004	Approach Flow Systems	25
Project F001	Status of Impulse Drying Commercialization	57

AIR-SHEET INTERACTIONS

STATUS REPORT

FOR

PROJECT F006

Xiaodong Wang

March 25, 1997

Institute of Paper Science and Technology
500 10th Street, N.W.
Atlanta, Georgia 30318

Project Title:	**Air-Sheet Interactions**
Project Code:	**AIRPA**
Project Number:	**F006**
PAC:	**Papermaking**
Division:	**Engineering and Paper Materials**
Project Leader:	**Xiaodong Wang**
Budget (FY95-FY96):	**$164,200.00**
Budget (FY96-FY97):	**$121,233.00**

This status report serves as a summary of the research between Fall 95 and Spring 97 PAC meetings (the period when I worked on this project originally proposed by Dr. Aidun). The initial air-sheet interactions project (F006) needs to be redirected to the runnability issues associating with the papermaking process.

Finite Element Analysis of Air-Sheet Interactions and Flutter Suppression Devices

Abstract

A computational procedure is developed to analyze the vibration of an axially moving web, controlled through self-acting air bearings. The Galerkin finite element method is employed for the spatial discretization of both the moving web and thin air layers. The predictor-corrector method is also implemented along with the Newton-Raphson iteration for the time integration. It is shown that the pressurized air layers between the moving web and bearing surfaces can significantly reduce the transverse web deflection and provide an effective means of stabilization. Some comparisons with results obtained using ADINA are presented. The computational algorithm introduced in this paper can be used to optimize both bearing geometry designs and spatial locations.

1 Introduction

With the increase in the machine speed and higher precision requirements in paper, thin film, and textile manufacturing and other technical processes in which flexible materials are pulled at high speeds over fixed points, transverse oscillations have received much attention. Such oscillations are often introduced by the aerodynamic instability of the surrounding air, roll eccentricity, material basis weight, and tension variations. The existence and persistence of the excessive vibrations will contribute to wrinkling, sheet breakage, and other runnability problems. To reduce the vibration with minimal modification of existing machine designs, researchers have proposed to stabilize the moving structure at various locations with self-acting air bearings or frictionless guides [1] [2]. The similar control of vibration by means of a viscous fluid has also been discussed by Ingard and Akay [3]. In fact, such dynamic systems are very much the same as those associated with high-speed magnetic tapes and flexible disk drives interacting with their recording heads [4]. In the paper industry, the initial ideas of using lubrication effects to help handle moving paper webs were proposed by Page [5] and Müftü and Benson [6].

For the analysis of such complex nonlinear coupling dynamic systems, the transfer function method was introduced to model the linearized solutions, and the bearing effects were described by the bearing impedance function [2] [7]. Some modification to include fluid inertia effects was discussed by Murray and Mote [8]. However, to incorporate more sophisticated bearing geometries and optimize the dynamic system designs, it is necessary to apply numerical methods for the fully coupled air-sheet systems. In this paper, we will present a finite element algorithm to analyze the dynamic behavior of the moving web coupled with a series of air bearings. We assume that the traveling material is a porous medium, and the tension T within the

web provides the dominant restoring force, i.e., $TL^2 \gg \frac{Ed^3}{12(1-\nu^2)}$ and $T/L \gg mg$, where E, m, g, ν, L, and d stand for the Young's modulus, the mass density, the gravity, the Poisson ratio, the web length, and thickness, respectively. Based on these assumptions, it is clear that the moving web can be modeled as a moving string. Furthermore, as pointed out by Pramila [9] [10] and Chang and Moretti [11], to analyze the moving paper web, we need to incorporate the surrounding air added mass effects. In this paper, the added mass terms are introduced as a function of the web width B.

2 Governing Equations

The air bearings used to suppress the web vibration consist of two rigid surfaces, positioned close to the axially moving web of a constant speed V. The gap formed between the moving web and two rigid surfaces is filled by a two-dimensional, laminar, and incompressible viscous air with the dynamic viscosity μ. All thermal effects and slipping of the fluid are ignored. The air bearings shown in Fig. 1 are located in the region $x \in [a_i, b_i]$, and the coupled governing equations are constructed as follows:

$$m\frac{\partial^2 w}{\partial t^2} + 2mV\frac{\partial^2 w}{\partial x \partial t} + (mV^2 - T)\frac{\partial^2 w}{\partial x^2} = f + p_2 - p_1 \qquad x \in [0, L] \tag{1}$$

$$-\frac{\partial}{\partial x}\left(\frac{1}{12\mu}\frac{\partial p_1}{\partial x}h_1^3\right) + \frac{\partial h_1}{\partial t} + \frac{V}{2}\frac{\partial h_1}{\partial x} + v_d = 0 \qquad x \in [a_i, b_i] \tag{2}$$

$$-\frac{\partial}{\partial x}\left(\frac{1}{12\mu}\frac{\partial p_2}{\partial x}h_2^3\right) + \frac{\partial h_2}{\partial t} + \frac{V}{2}\frac{\partial h_2}{\partial x} - v_d = 0 \qquad x \in [a_i, b_i] \tag{3}$$

with the boundary conditions

$$w(0,t) = w(L,t) = 0 \quad \text{and} \quad p_1(x,t) = p_2(x,t) = 0 \quad x \in [0, L]/(a_i, b_i)$$

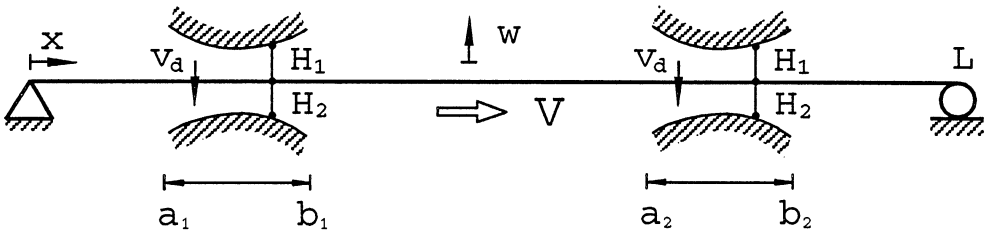

Figure 1: The coupled system of the moving web and two-sided suppression devices.

where w, f, v_d, h_j, and p_j $(j = 1, 2)$ stand for the transverse web deflection, the external force, the net downward velocity of the diffusive flow through the porous web surface, the air bearing clearances, and pressures, respectively. For the two air bearing surface profiles H_1 and H_2, the upper and lower clearances are defined by

$$h_1 = H_1 - w \tag{4}$$

$$h_2 = H_2 + w. \tag{5}$$

Assuming that the web thickness d is small, from the Darcy's law, we obtain

$$v_d = \frac{k}{\mu}\frac{(p_1 - p_2)}{d} \tag{6}$$

where k is the paper permeability.

In the nonlinear coupled equations (1), (2), and (3), we have three unknowns w, p_1, and p_2. To introduce the surrounding air effects, we introduce $m_j = \rho\beta L$ $(j = 1, 2, 3)$ to the inertia, Coriolis, and centrifugal mass terms, respectively, where β is a function of the web width.

3 Finite Element Formulation

The variations of the internal energy and external work are defined as $\delta\mathbf{W}$ and $\delta\mathbf{R}$. At any time t, the standard variational form of Eqs. (1), (2), and (3) can be written as

$$\delta^t\mathbf{W} = \delta^t\mathbf{R} \tag{7}$$

where $\delta\mathbf{W} = (\delta W_w, \delta W_{p_1}, \delta W_{p_2})^T$, $\delta\mathbf{R} = (\delta R_w, 0, 0)^T$, and

$$\begin{aligned}
\delta W_w &= \int_0^L \{\delta w(m\frac{\partial^2 w}{\partial t^2} + 2mV\frac{\partial^2 w}{\partial x \partial t}) - \frac{\partial \delta w}{\partial x}(mV^2 - T)\frac{\partial w}{\partial x} \\
&\quad + \delta w(p_1 - p_2)\}\, dx \qquad (8) \\
\delta W_{p_1} &= \int_{a_i}^{b_i} \{\frac{\partial \delta p_1}{\partial x}\frac{1}{12\mu}(H_1 - w)^3\frac{\partial p_1}{\partial x} - \delta p_1\frac{\partial w}{\partial t} \\
&\quad + \delta p_1\frac{k}{\mu}\frac{(p_1 - p_2)}{d} + \delta p_1\frac{V}{2}\frac{\partial H_1}{\partial x} - \delta p_1\frac{V}{2}\frac{\partial w}{\partial x}\}\, dx \qquad (9) \\
\delta W_{p_2} &= \int_{a_i}^{b_i} \{\frac{\partial \delta p_2}{\partial x}\frac{1}{12\mu}(H_2 + w)^3\frac{\partial p_2}{\partial x} + \delta p_2\frac{\partial w}{\partial t} \\
&\quad + \delta p_2\frac{k}{\mu}\frac{(p_2 - p_1)}{d} + \delta p_2\frac{V}{2}\frac{\partial H_2}{\partial x} + \delta p_2\frac{V}{2}\frac{\partial w}{\partial x}\}\, dx \qquad (10) \\
\delta R_w &= \int_0^L \delta w f\, dx. \qquad (11)
\end{aligned}$$

Note that the displacement variation δw is the arbitrary admissible out-of-plane displacement, i.e., $\delta w = 0$, at $x = 0, L$, and the pressure variations δp_1 and δp_2 are arbitrary within the interval $a_i < x < b_i$, but for which $\delta p_1 = \delta p_2 = 0$ at $x = a_i, b_i$.

From the Taylor's expansion, we have

$$\delta\Delta^t\mathbf{W} = \delta^t\dot{\mathbf{W}}\Delta t \simeq \delta^{t+\Delta t}\mathbf{R} - \delta^t\mathbf{W} \tag{12}$$

where

$$\delta\dot{W}_w\Delta t = \int_0^L \{\delta w(m\frac{\partial^2\Delta w}{\partial t^2} + 2mV\frac{\partial^2\Delta w}{\partial x\partial t}) - \frac{\partial\delta w}{\partial x}(mV^2 - T)\frac{\partial\Delta w}{\partial x} + \delta w(\Delta p_1 - \Delta p_2)\}\, dx \tag{13}$$

$$\delta\dot{W}_{p_1}\Delta t = \int_{a_i}^{b_i} \{\frac{\partial\delta p_1}{\partial x}\frac{1}{12\mu}(H_1 - w)^3\frac{\partial\Delta p_1}{\partial x} - \frac{\partial\delta p_1}{\partial x}\frac{1}{4\mu}(H_1 - w)^2\Delta w\frac{\partial p_1}{\partial x} - \delta p_1\frac{\partial\Delta w}{\partial t} + \delta p_1\frac{k}{\mu}\frac{(\Delta p_1 - \Delta p_2)}{d} - \delta p_1\frac{V}{2}\frac{\partial\Delta w}{\partial x}\}\, dx \tag{14}$$

$$\delta\dot{W}_{p_2}\Delta t = \int_{a_i}^{b_i} \{\frac{\partial\delta p_2}{\partial x}\frac{1}{12\mu}(H_2 + w)^3\frac{\partial\Delta p_2}{\partial x} + \frac{\partial\delta p_2}{\partial x}\frac{1}{4\mu}(H_2 + w)^2\Delta w\frac{\partial p_2}{\partial x} + \delta p_2\frac{\partial\Delta w}{\partial t} + \delta p_2\frac{k}{\mu}\frac{(\Delta p_2 - \Delta p_1)}{d} + \delta p_2\frac{V}{2}\frac{\partial\Delta w}{\partial x}\}\, dx. \tag{15}$$

It is clear that, when Eqs. (8), (9), and (10) are expanded, we retain those terms that are linear in the small increments of $\boldsymbol{\theta} = (w, p_1, p_2)^T$ ($\Delta\boldsymbol{\theta} = \dot{\boldsymbol{\theta}}\Delta t$); i.e., we neglect all squares, products, and higher powers of those small increments.

We introduce the nodal unknowns $\Theta = (\widehat{\mathbf{W}}, \widehat{\mathbf{P}}_1, \widehat{\mathbf{P}}_2)^T$, and by applying the standard Galerkin finite element procedure, we obtain

$$\mathbf{M}\Delta\ddot{\Theta} + \mathbf{C}\Delta\dot{\Theta} + \mathbf{K}\Delta\Theta = \Delta\mathbf{R} \tag{16}$$

where

$$\mathbf{M} = \begin{bmatrix} \mathbf{M}_{ww} & 0 & 0 \\ 0 & 0 & 0 \\ 0 & 0 & 0 \end{bmatrix} \qquad \mathbf{C} = \begin{bmatrix} \mathbf{C}_{ww} & 0 & 0 \\ \mathbf{C}_{p_1w} & 0 & 0 \\ \mathbf{C}_{p_2w} & 0 & 0 \end{bmatrix},$$

$$\mathbf{K} = \begin{bmatrix} \mathbf{K}_{ww} & \mathbf{K}_{wp_1} & \mathbf{K}_{wp_2} \\ \mathbf{K}_{p_1w} & \mathbf{K}_{p_1p_1} & \mathbf{K}_{p_1p_2} \\ \mathbf{K}_{p_2w} & \mathbf{K}_{p_2p_1} & \mathbf{K}_{p_2p_2} \end{bmatrix} \quad \Delta\mathbf{R} = \begin{Bmatrix} \mathbf{R}_w \\ 0 \\ 0 \end{Bmatrix} - \begin{Bmatrix} \mathbf{F}_w \\ \mathbf{F}_{p_1} \\ \mathbf{F}_{p_2} \end{Bmatrix},$$

$$\delta\mathbf{W}^T\mathbf{F}_w = \delta W_w, \quad \delta\mathbf{P}_1{}^T\mathbf{F}_{p_1} = \delta W_{p_1}, \quad \delta\mathbf{P}_2{}^T\mathbf{F}_{p_2} = \delta W_{p_2}, \quad \delta\mathbf{W}^T\mathbf{R}_w = \delta R_w;$$

and

$$\begin{aligned}
\delta\mathbf{W}^T\mathbf{K}_{wp_1}\Delta\widehat{\mathbf{P}}_1 &= \int_{a_i}^{b_i}\delta w\Delta p_1\,dx & \delta\mathbf{W}^T\mathbf{C}_{ww}\Delta\dot{\widehat{\mathbf{W}}} &= \int_0^L 2mV\delta w\frac{\partial^2\Delta w}{\partial x\partial t}\,dx,\\
\delta\mathbf{P}_1{}^T\mathbf{K}_{p_1p_2}\Delta\widehat{\mathbf{P}}_2 &= -\int_{a_i}^{b_i}\delta p_1\frac{k}{\mu}\frac{\Delta p_2}{d}\,dx & \delta\mathbf{W}^T\mathbf{M}_{ww}\Delta\ddot{\widehat{\mathbf{W}}} &= \int_0^L m\delta w\frac{\partial^2\Delta w}{\partial t^2}\,dx,\\
\delta\mathbf{W}^T\mathbf{K}_{wp_2}\Delta\widehat{\mathbf{P}}_2 &= -\int_{a_i}^{b_i}\delta w\Delta p_2\,dx & \delta\mathbf{P}_1{}^T\mathbf{C}_{p_1w}\Delta\dot{\widehat{\mathbf{W}}} &= -\int_{a_i}^{b_i}\delta p_1\frac{\partial\Delta w}{\partial t}\,dx,\\
\delta\mathbf{P}_2{}^T\mathbf{K}_{p_2p_1}\Delta\widehat{\mathbf{P}}_1 &= -\int_{a_i}^{b_i}\delta p_2\frac{k}{\mu}\frac{\Delta p_1}{d}\,dx & \delta\mathbf{P}_2{}^T\mathbf{C}_{p_2w}\Delta\dot{\widehat{\mathbf{W}}} &= \int_{a_i}^{b_i}\delta p_2\frac{\partial\Delta w}{\partial t}\,dx,
\end{aligned}$$

$$\begin{aligned}
\delta\mathbf{W}^T\mathbf{K}_{ww}\Delta\widehat{\mathbf{W}} &= -\int_0^L\frac{\partial\delta w}{\partial x}(mV^2-T)\frac{\partial\Delta w}{\partial x}\,dx,\\
\delta\mathbf{P}_1{}^T\mathbf{K}_{p_1p_1}\Delta\widehat{\mathbf{P}}_1 &= \int_{a_i}^{b_i}\{\frac{\partial\delta p_1}{\partial x}\frac{1}{12\mu}(H_1-w)^3\frac{\partial\Delta p_1}{\partial x}+\delta p_1\frac{k}{\mu}\frac{\Delta p_1}{d}\}\,dx,\\
\delta\mathbf{P}_1{}^T\mathbf{K}_{p_1w}\Delta\widehat{\mathbf{W}} &= -\int_{a_i}^{b_i}\{\frac{\partial\delta p_1}{\partial x}\frac{1}{4\mu}(H_1-w)^2\Delta w\frac{\partial p_1}{\partial x}+\delta p_1\frac{V}{2}\frac{\partial\Delta w}{\partial x}\}\,dx,\\
\delta\mathbf{P}_2{}^T\mathbf{K}_{p_2p_2}\Delta\widehat{\mathbf{P}}_2 &= \int_{a_i}^{b_i}\{\frac{\partial\delta p_2}{\partial x}\frac{1}{12\mu}(H_2+w)^3\frac{\partial\Delta p_2}{\partial x}+\delta p_2\frac{k}{\mu}\frac{\Delta p_2}{d}\}\,dx,\\
\delta\mathbf{P}_2{}^T\mathbf{K}_{p_2w}\Delta\widehat{\mathbf{W}} &= \int_{a_i}^{b_i}\{\frac{\partial\delta p_2}{\partial x}\frac{1}{4\mu}(H_2+w)^2\Delta w\frac{\partial p_2}{\partial x}+\delta p_2\frac{V}{2}\frac{\partial\Delta w}{\partial x}\}\,dx.
\end{aligned}$$

For the direct time integration along with the Newton-Raphson iteration, we apply the following predictor-corrector procedure

$$\begin{aligned}
{}^{t+\Delta t}\widetilde{\mathbf{M}}^{(i)}\Delta\ddot{\Theta}^{(i+1)} &= \Delta\mathbf{R}^{(i)}\\
{}^{t+\Delta t}\ddot{\Theta}^{(i+1)} &= {}^{t+\Delta t}\ddot{\Theta}^{(i)}+\Delta\ddot{\Theta}^{(i+1)}\\
{}^{t+\Delta t}\dot{\Theta}^{(i+1)} &= {}^{t+\Delta t}\dot{\Theta}^{(0)}+\gamma\Delta t\;{}^{t+\Delta t}\ddot{\Theta}^{(i+1)}\\
{}^{t+\Delta t}\Theta^{(i+1)} &= {}^{t+\Delta t}\Theta^{(0)}+\beta\Delta t^2\;{}^{t+\Delta t}\ddot{\Theta}^{(i+1)}
\end{aligned}\qquad(17)$$

where the effective mass matrix $\widetilde{\mathbf{M}}=\mathbf{M}+\Delta t\gamma\mathbf{C}+\Delta t^2\beta\mathbf{K}$ (in this paper, $\gamma=0.5$, $\beta=0.25$) and the initial iteration steps ($i=0$) are given as

$$
\begin{aligned}
{}^{t+\Delta t}\Theta^{(0)} &= {}^{t}\Theta + \Delta t\,{}^{t}\dot{\Theta} + \frac{\Delta t^2}{2}(1-2\beta)\,{}^{t}\ddot{\Theta} \\
{}^{t+\Delta t}\dot{\Theta}^{(0)} &= {}^{t}\dot{\Theta} + \Delta t(1-\gamma)\,{}^{t}\ddot{\Theta} \\
{}^{t+\Delta t}\ddot{\Theta}^{(0)} &= 0.
\end{aligned}
$$

Note that because the convective terms $\frac{V}{2}\frac{\partial w}{\partial x}$ and $2mV\frac{\partial^2 w}{\partial x \partial t}$ introduce nonsymmetric $\mathbf{K}$ and $\mathbf{C}$ matrices, an effective nonsymmetric column solver is implemented [12]. However, it is found that these nonsymmetric terms do not introduce spatial oscillations that need to be treated with upwinding discretizations.

4 Numerical Results

The proposed algorithm is implemented to analyze a typical moving paper web traveling at different velocities (V = 0, 4.85, and 9.7 m/s). A set of cylindrical surface air bearings (depicted in Fig. 2) is located at $x = 0.5$ and $x = 1.9$ as suppression devices.

The physical parameters are given as follows: $H_{min} = 0.0002\ m$; $H_{max} = 0.02\ m$; $m = 0.0355\ kg/m^2$; $T = 280\ N/m$; $k = 5.0 \times 10^{-13}\ m^2$; $d = 5.0 \times 10^{-5}\ m$; $\mu = 2.0 \times 10^{-5}\ Pa \cdot s$; $\rho = 1.2\ kg/m^3$; $l_j = b_j - a_j = 0.2\ m$; and $L = 2.4\ m$. The added mass coefficient β is assumed to be 0.34 with the web length/width ratio $L/B = 5.0$.

For this fluid-structure coupling system, the lubrication effects are achieved by the slide and squeeze motions (i.e., the web transverse and axial motions). To verify the implementation of the proposed finite element algorithm, in Figures 3 and 4, the computed pressure distributions are compared with the analytical results published by Hamrock [13] as well as the ADINA solutions. The pressures are normalized by $\mu UR/H_{min}^2$, where R and U stand for the cylindrical surface radius and the slide or squeeze velocity. As can be seen, the results are in good agreement.

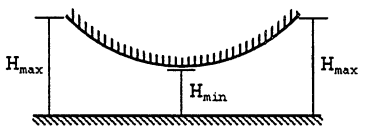

Figure 2: The cylindrical surface air bearing profile.

It is interesting to note that in this case, the ADINA CFD results match well with the Reynolds equation solutions. Nevertheless, if the air bearing inertia effects are significant, i.e., the Reynolds number $Re = \frac{UH_{min}^2}{\nu l_j} \sim O(1)$, the Reynolds equation used in this paper can no longer describe accurately the lubrication zones, see Fig. 5.

Because the purposes of using these suppression devices are to reduce oscillations and to stabilize the moving web, it is of interest to calculate the time history of the following measures of average positive and negative nodal displacements (W_i^+ and W_i^-) along with the mid-span nodal displacement,

$$\bar{W}^+ = \sum_{i=1}^{N^+} W_i^+ / N^+ \tag{18}$$

$$\bar{W}^- = \sum_{i=1}^{N^-} W_i^- / N^- \tag{19}$$

where N^+ and N^- are the total numbers of positive and negative nodal displacements.

For the concentrated dynamic load applied at the mid-span node with the time functions shown in Fig. 6, the salient features of the mid-span dynamic responses with and without suppression devices shown in Figs. 7 to 10, demonstrate the stabilizing effects of such suppression devices. The average positive and negative displacement measures shown in Fig. 11 confirm the conclusions drawn based on the

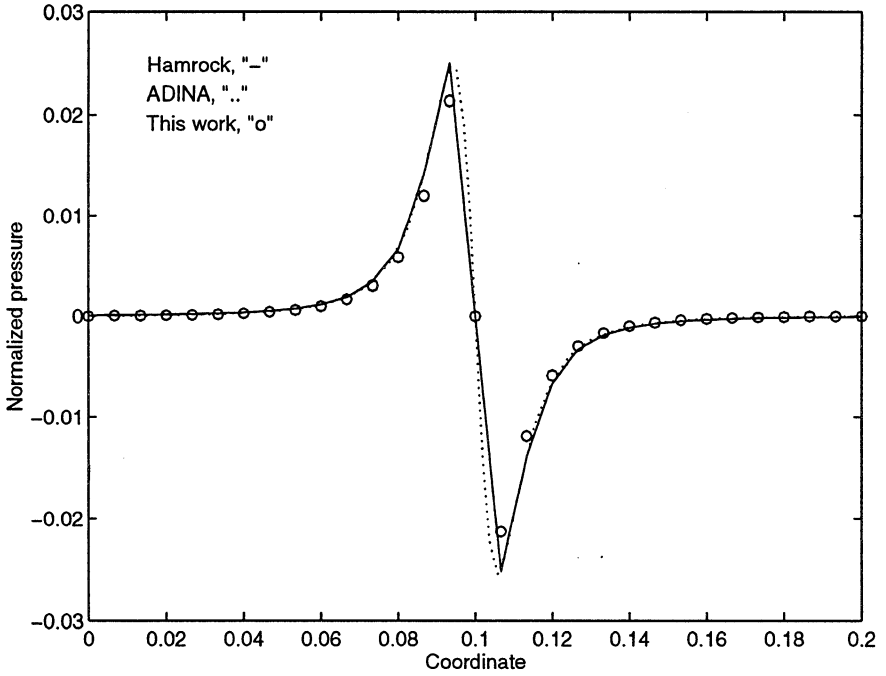

Figure 3: Pressure distribution comparisons of cylindrical surface bearing with the slide motion.

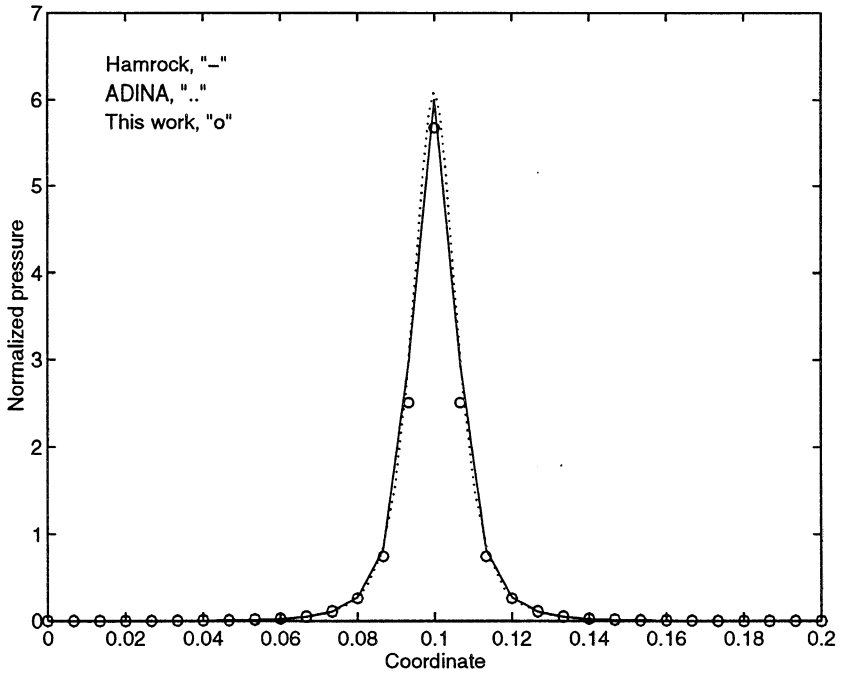

Figure 4: Pressure distribution comparisons of cylindrical surface bearing with the squeeze motion.

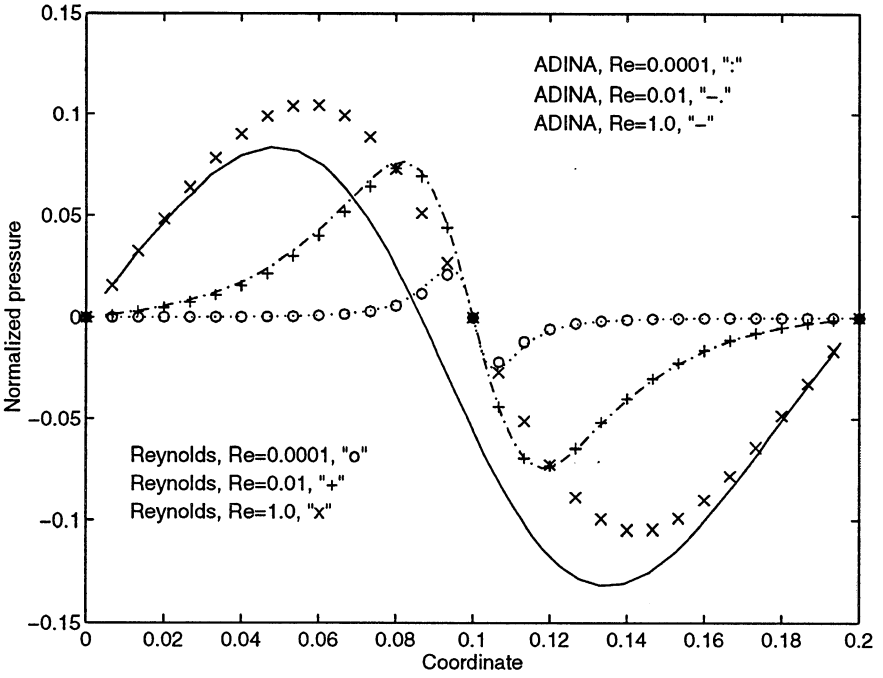

Figure 5: The Reynolds equation approximations.

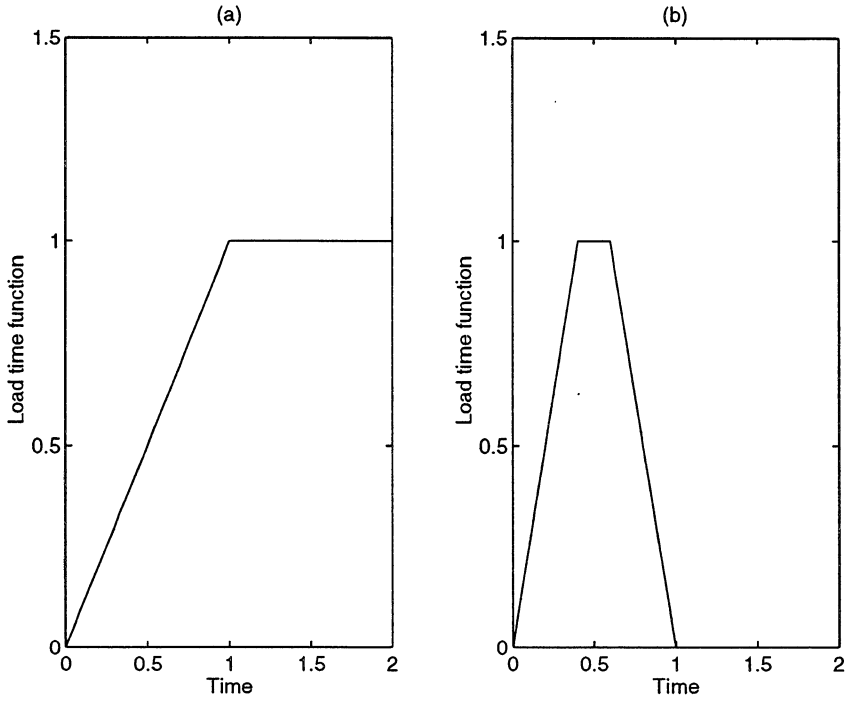

Figure 6: Load time functions.

mid-span displacement responses.

Two points may be noticed: first, the suppression devices provide the damping needed to stabilize the traveling web; second, the suppression devices alter the steady response of the moving web. For the web traveling at the velocity V, the stiffness of the steady response is reduced to $T - mV^2$.

Figures 12 and 13 illustrate the paper web porosity effects on suppression devices. Because the moving paper web travels through the upper and lower air bearings, the porosity effects are minimized due to the fact that the air mass is always preserved within the bearing couples.

Three modifications of suppression devices are made separately: first, the bearing location ($x = 0.7$ and $x = 1.7$); second, the bearing clearance ($H_{min} = 0.0001\ m$ and $H_{max} = 0.0199\ m$); and third, the bearing profile ($R = 0.1\ m$ and $l_j = 0.1\ m$). The comparisons of their dynamic responses are shown in Fig. 14. It is confirmed that both the steady response and damping effects can be modified by varying the bearing locations, clearances, and profiles. More specifically, we observe the following:

- the reduction of clearances will increase the damping and stiffness of the air bearings;
- by shifting the bearings to the middle of the moving web, the mid-span deflection can be reduced significantly; and
- the reduction of bearing length will weaken the suppression effects.

For the stationary tensioned web ($V = 0.0$), we compare the solutions of the ADINA fluid-structure interaction analysis (using the Navier-Stokes equations instead of the Reynolds equations). As shown in Fig. 15, both the displacement and

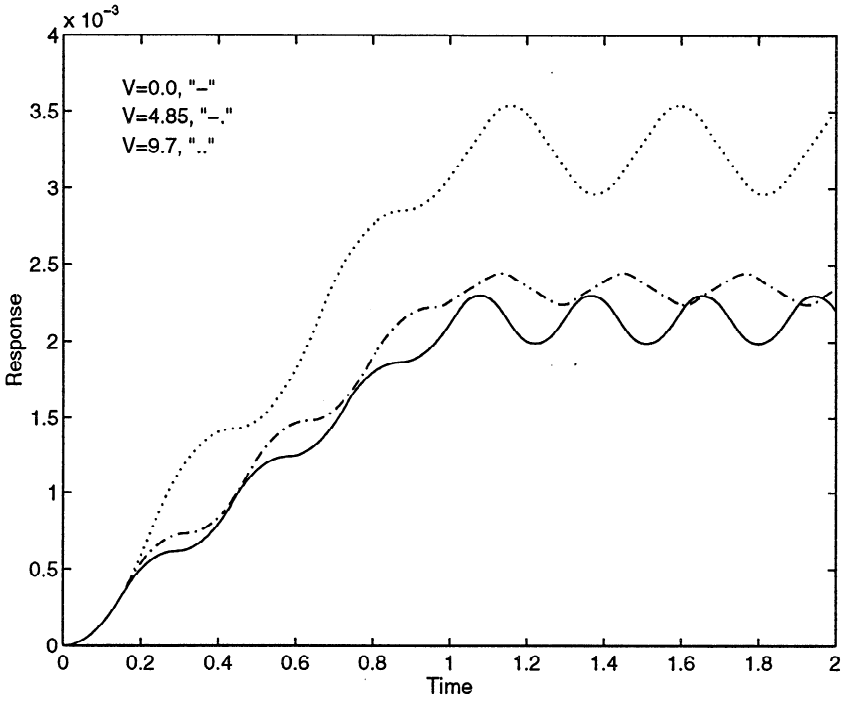

Figure 7: Response due to load (a) without suppression devices.

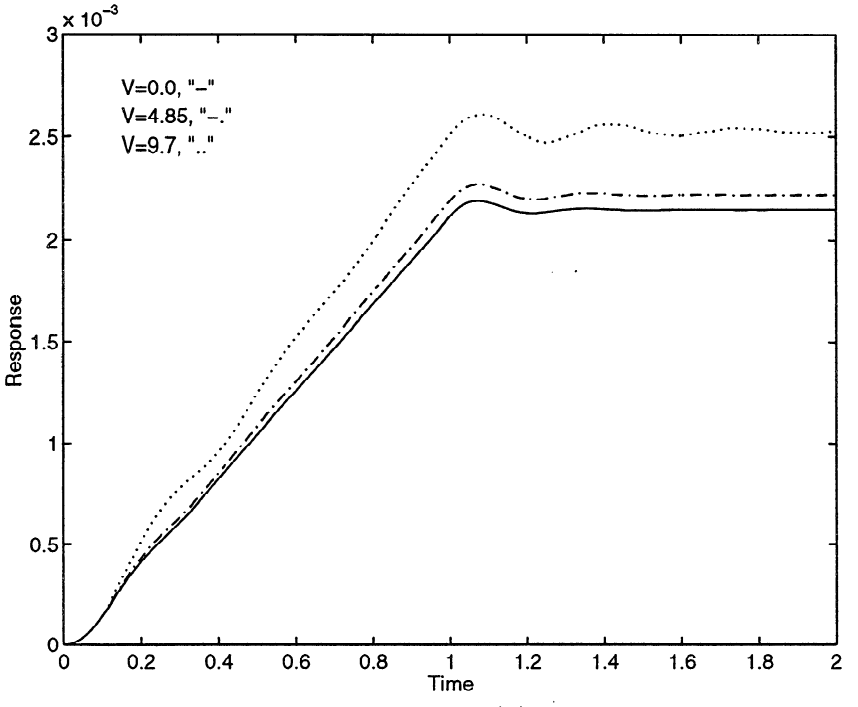

Figure 8: Response due to load (a) with suppression devices.

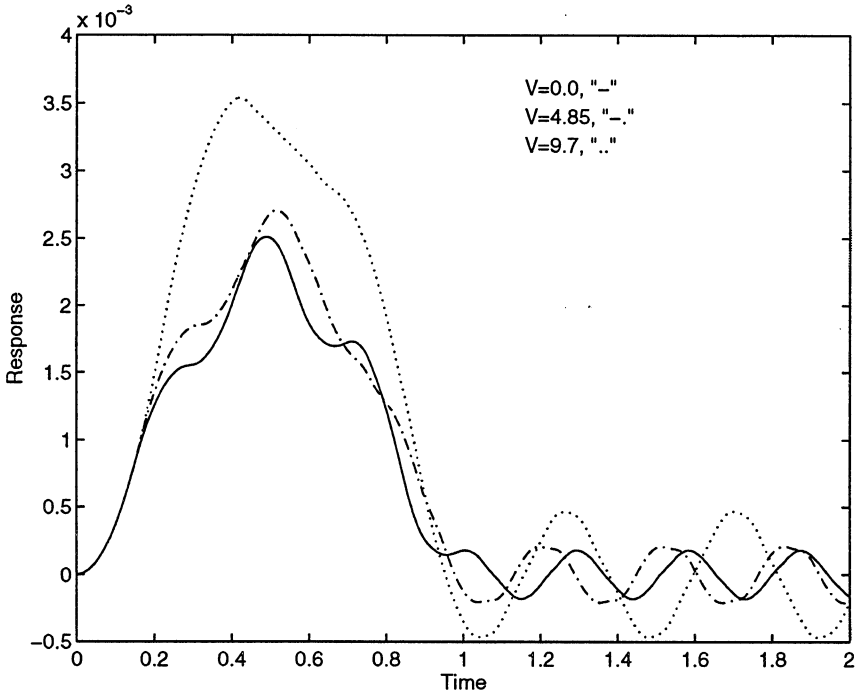

Figure 9: Response due to load (b) without suppression devices.

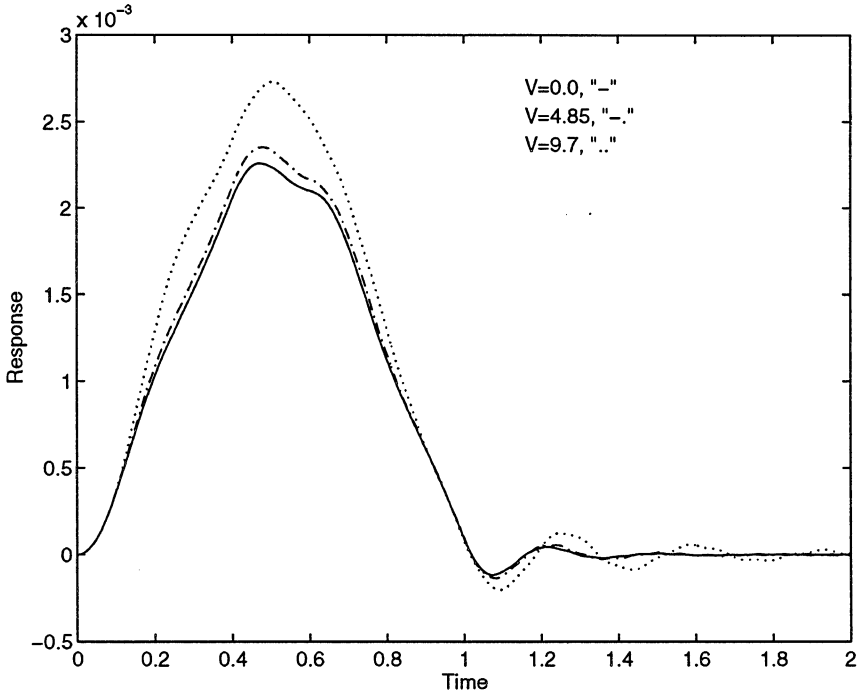

Figure 10: Response due to load (b) with suppression devices.

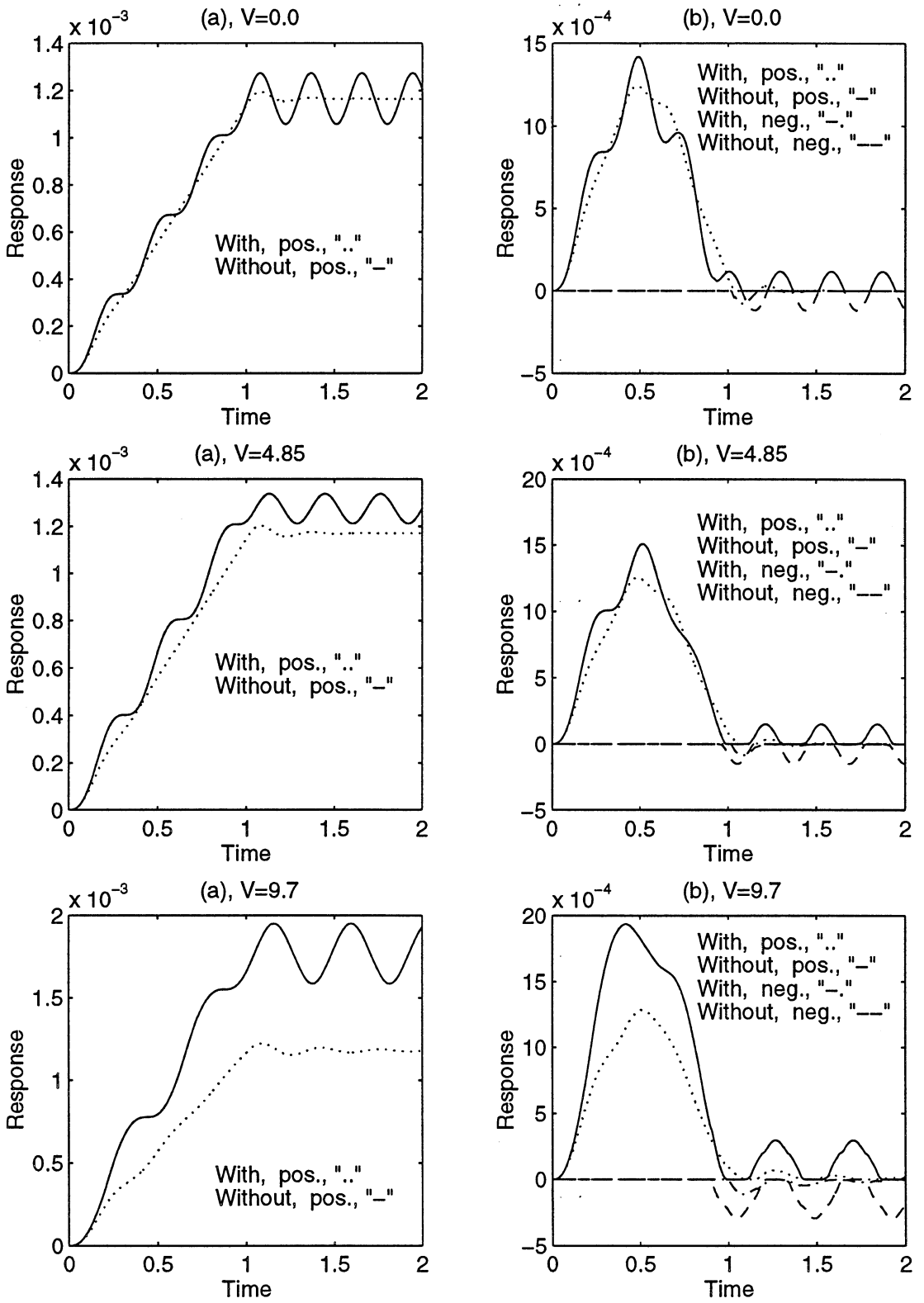

Figure 11: The time history of average positive and negative displacements with and without suppression devices.

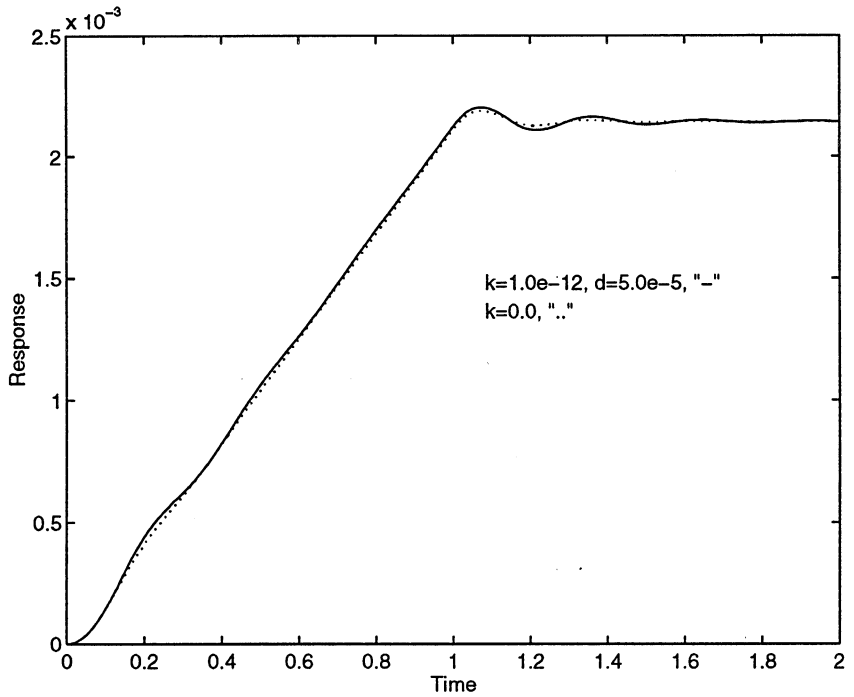

Figure 12: The web porosity effects with load (a).

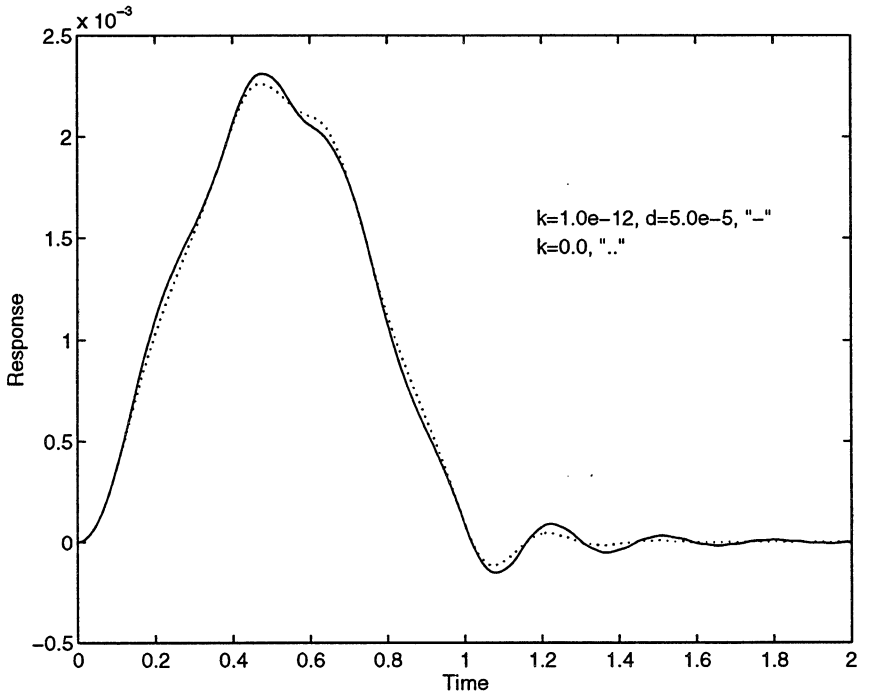

Figure 13: The web porosity effects with load (b).

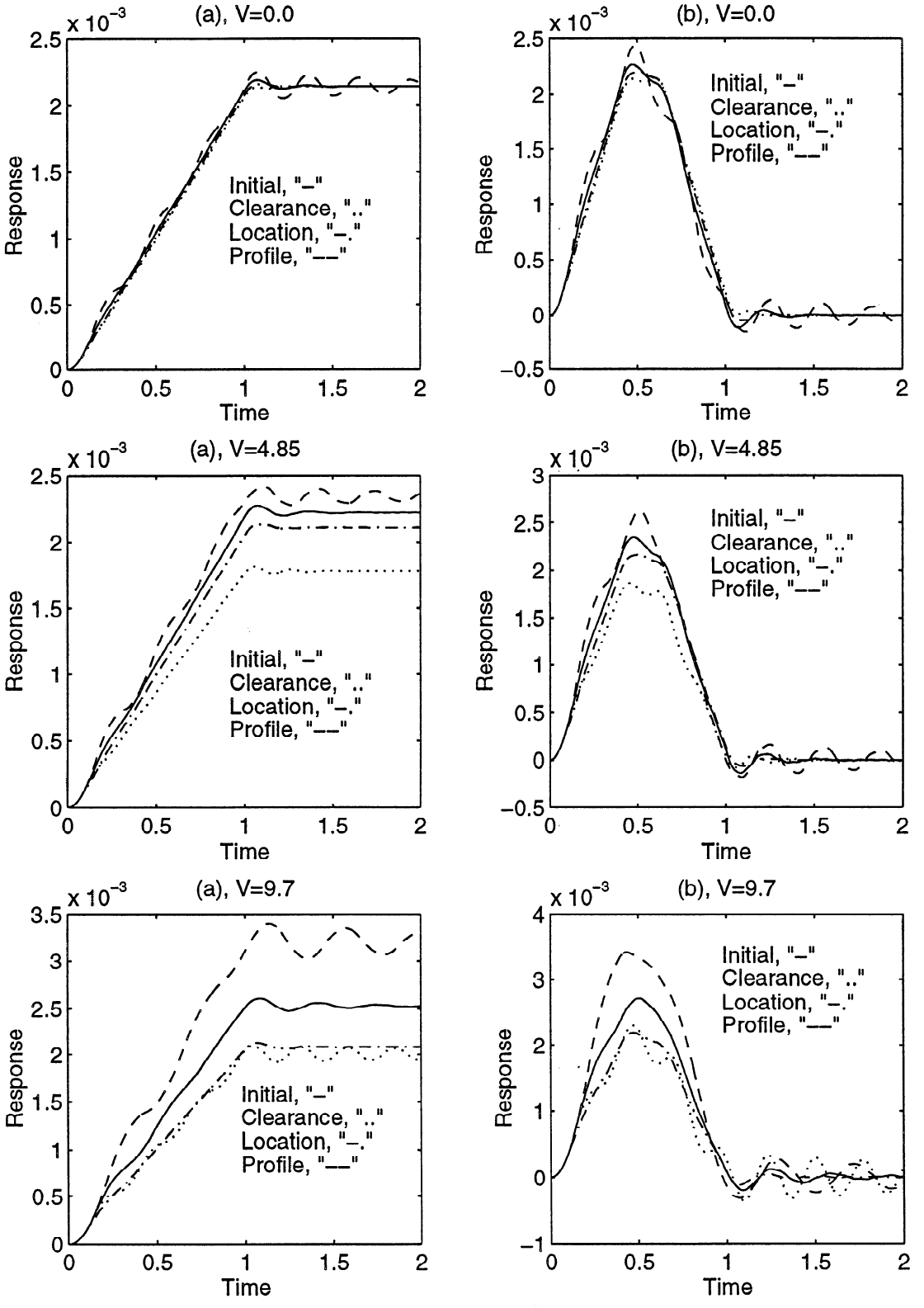

Figure 14: The modifications of bearing locations, clearances, and profiles.

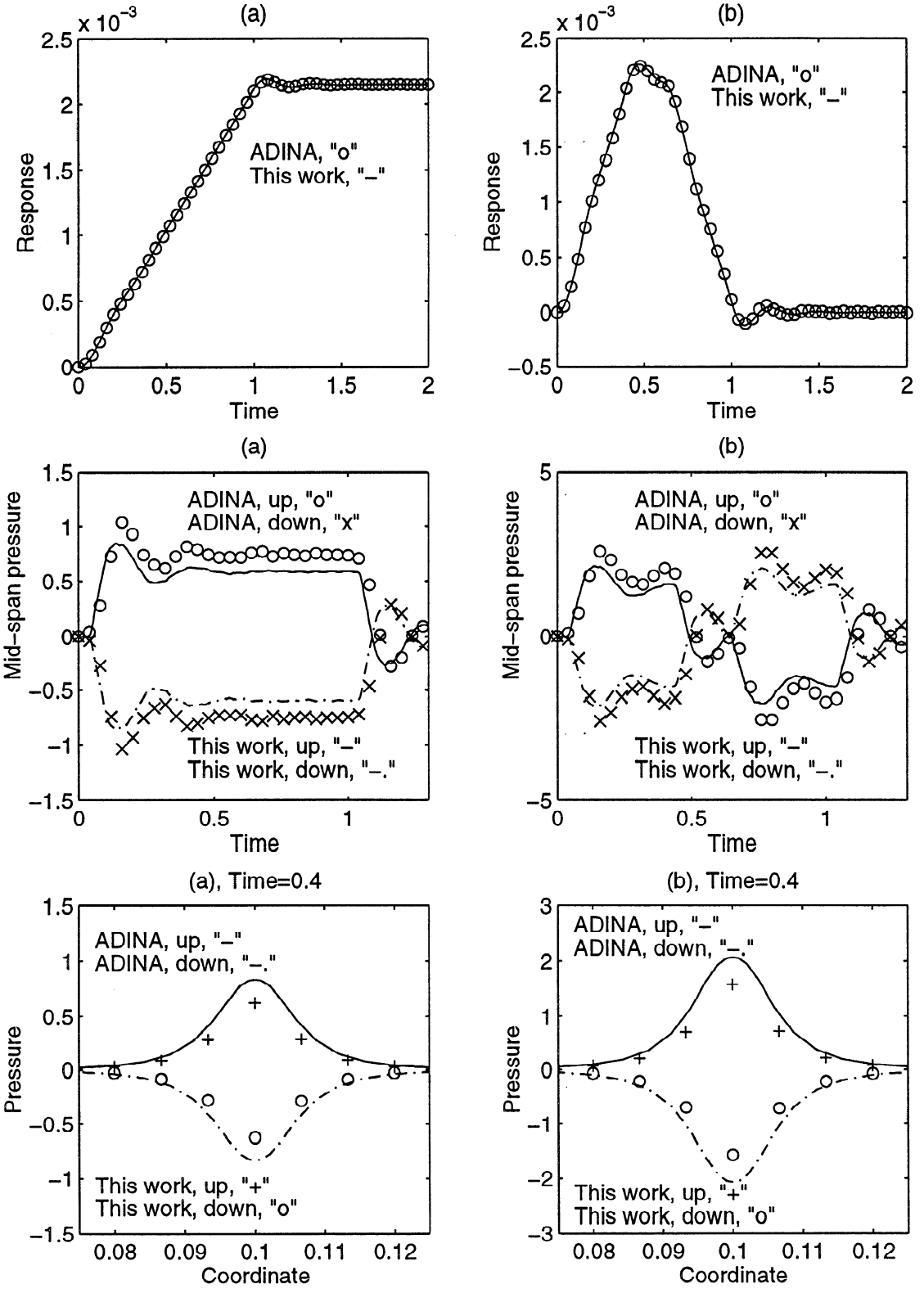

Figure 15: The comparisons with ADINA solutions for the zero traveling velocity cases.

pressure results match each other. Further comparisons and studies will be the subject of future research.

5 Conclusion

In this paper, the coupling dynamic response of a moving web and air bearing suppression devices is analyzed with a proposed finite element procedure and ADINA. The effects on both the steady and dynamic responses due to the changes of bearing designs and locations are investigated.

It is found that the optimized suppression device design is highly dependent on the web moving velocity. Therefore, an adjustable installation of such devices is beneficial when the web traveling velocity needs to be varied.

Based on the studies in this paper, we confirm that for the cases with low Reynolds number, the Reynolds lubrication equation can be effectively used with good accuracy; however, when the lubricant inertia contribution is significant, CFD analysis is needed to couple with the moving web. It is also of interest to note that the web permeability barely affects the dynamic response with the double-sided suppression devices discussed in this paper.

In practice, the nips formed between suppression device surfaces also act as effective supports of the moving web and can significantly reduce the critical traveling speed by reducing the open draw length.

6 Acknowledgment

The author would like to thank the Institute of Paper Science and Technology and its Member Companies for their support, and the researchers in ADINA R&D, Watertown, MA, for helpful suggestions.

References

[1] C.D. Mote. A study of band saw vibrations. *Journal of the Franklin Institute*, 279(6):430–444, 1965.

[2] C.A. Tan and C.D. Mote, Jr. Analysis of a hydrodynamic bearing under transverse vibration of an axially moving band. *Journal of Tribology*, 112:514–523, 1990.

[3] K.U. Ingard and A. Akay. On the vibration damping of a plate by means of a viscous fluid layer. *Journal of Vibration, Acoustics, Stress, and Reliability in Design*, 109:178–184, 1987.

[4] J.C. Heinrich and D. Connolly. Three-dimensional finite element analysis of self-acting foil bearings. *Computer Methods in Applied Mechanics and Engineering*, 100:31–43, 1992.

[5] R.E. Page. Method of suppressing paper web flutter. *United States Patent*, 4321107, March 1982.

[6] S. Müftü and R.C. Benson. Modelling the transport of paper webs including the paper permeability effects. *Proceedings of ISPS at the ASME-International Congress and Exposition in San Fransisco, CA*, November 1995.

[7] C.A. Tan, B. Yang, and C.D. Mote, Jr. On the vibration of a translating string coupled to hydrodynamic bearings. *Journal of Vibration and Acoustics*, 112:337–345, 1990.

[8] Y.D. Murray and C.D. Mote, Jr. Analysis of a plane inclined guide bearing under transverse vibration and translation of a plate. *Journal of Lubrication Technology*, 105:335–341, 1983.

[9] A. Pramila. Sheet flutter and the interaction between sheet and air. *Tappi Journal*, pages 70–74, July 1986.

[10] A. Pramila. Natural frequencies of a submerged axially moving band. *Journal of Sound and Vibration*, 113(1):198–203, 1987.

[11] Y.B. Chang and P.M. Moretti. Interaction of fluttering webs with surrounding air. *Tappi Journal*, pages 231–236, March 1991.

[12] K.J. Bathe. *Finite Element Procedures.* Prentice Hall, Englewood Cliffs, N.J., 1996.

[13] B.J. Hamrock. *Fundamentals of Fluid Film Lubrication.* McGraw-Hill, Inc., 1994.

APPROACH FLOW SYSTEMS

STATUS REPORT

FOR

PROJECT F004

Xiaodong Wang

March 25, 1997

Institute of Paper Science and Technology
500 10th Street, N.W.
Atlanta, Georgia 30318

Project Title:	**Approach Flow Systems**
Project Code:	**PIPES**
Project Number:	**F004**
PAC:	**Papermaking**
Division:	**Engineering and Paper Materials**
Project Leader:	**Xiaodong Wang**
Budget (FY95-FY96):	**N/A**
Budget (FY96-FY97):	**$95,776.00**

This report covers the progress on the approach flow systems project (F004) from Fall 1996 to Spring 1997. The major achievements are a preliminary study on the consistency fluctuations within different stages of the stock preparation process and their correlation to the MD basis weight variation and a preliminary stock mixing experimental setup design. Future research plans from Spring 1997 to Fall 1997 are also outlined.

Summary

Consistency and Basis Weight Variation Analysis

Regardless of the dampening features of individual headbox designs, it is important to minimize the stock consistency variations prior to headbox delivery. As part of the objectives of this approach flow systems project, we need to identify the contributions to the MD basis weight variations from various stages of the stock preparation process.

We analyzed one set of mill data of consistency variations at 14 different locations of the stock preparation process. To properly correlate the signals, we took into consideration the delay of time. To make the analysis even more interesting, the consistency and basis weight (fixed point) variations include the conversion of paper grades, which can be easily identified in the basis weight measurement. Sixteen channel signals are gathered from the mill, i.e., HW HI-D, SW HI-D, Swing HI-D, HW refiner, SW refiner, Coated broke, Uncoated broke, Recovered stock, Blender, Blend chest, Stuff box, Headbox, Silo return, Couch, Basis weight, and Ground. The sensor locations are illustrated in Fig.1.

We divided the signals ($\sim$ 5 hours, with $\Delta t = 0.01$ sec) into three segments, i.e., #1, #2, and the transition #1 $\rightarrow$ #2, corresponding to the grade change. In addition, to accurately analyze the data at three different frequency ranges (≤ 0.125 Hz, ≤ 2.5 Hz, and ≤ 50 Hz), we employed different signal processing techniques.

The corresponding consistency and basis weight variations are shown in the attached figures, along with their spectra, certain correlations, and phase portraits (for the identification of strange attractors). By comparing the stuff box and headbox data, it is clearly visible that different frequency spikes do emerge after the stock

passing through the approach flow systems (from the stuff box to headbox). This suggests that it is possible and necessary to improve the designs within approach flow systems.

Preliminary data analysis software has been developed to handle the multichannel long time duration measurements and generate automatically the needed set of plots.

Experimental Approach Flow System Setup

The planned experimental approach flow system will be constructed at IPST's Industrial Research Facility. In order to properly design the stock mixing experimental setup, we start with a dimensional analysis, and focus on three zones (shown in Fig. 2):

- the mixing zone between the stock pipe outlet and fan pump ($l^* - l_2 = l_0$);
- the stock pipe zone (l_2); and
- the silo zone.

We define the average consistency change f_0 as,

$$f_0 = \frac{\sum_{i=1}^{2} c_i \bar{u}_i A_i}{\sum_{i=1}^{2} \bar{u}_i A_i} \tag{1}$$

and the time rate of change $\dot{f}_0$ is given as,

$$\dot{f}_0 = \{\sum_{i=1}^{2}(\dot{c}_i \bar{u}_i A_i + c_i \dot{\bar{u}}_i A_i) \sum_{i=1}^{2} \bar{u}_i A_i - \sum_{i=1}^{2} c_i \bar{u}_i A_i \sum_{i=1}^{2} \dot{\bar{u}}_i A_i\} / (\sum_{i=1}^{2} \bar{u}_i A_i)^2. \tag{2}$$

Note that we have two separate problems. Firstly, within the mixing zone, the stock mixing behavior is determined by the nozzle shape, l_0, incline angle, etc., and the mixing will influence the performance of the fan pump. From the analysis of the mixing zone, we can obtain the key information on the location of fan pump and fiber distribution uniformity in the cross section. Secondly, within the silo water and stock pipe, the perturbation of consistency and velocity will affect the average consistency of stocks coming out of the fan pump. Both problems have two distinctive scales of interest. Using the Buckingham Π theorem, we obtain the following nondimensional parameters for the three zones:

$$Zone\ 1 : (c_1, c_2) = \mathcal{F}_1 \left(\frac{\bar{u}_i}{(\epsilon_i \nu_i)^{1/4}}, \frac{A_i}{(\nu_i{}^3/\epsilon_i)^{1/2}}, \frac{A_0}{A_1}, \frac{l_0}{\sqrt{A_0}}, \frac{H_2}{l_2}\right),$$

$$\frac{\Delta P_i}{\rho_i(\epsilon_i\nu_i)^{1/2}}\ ,\ \frac{\epsilon_1}{\epsilon_2}\ ,\ \frac{\nu_1}{\nu_2}\ ,\ \frac{\rho_1}{\rho_2}) \tag{3}$$

$$Zone\ 2 : c_2 = \mathcal{F}_2\ (\frac{\bar{u}_2}{(\epsilon_2\nu_2)^{1/4}}\ ,\ \frac{A_2}{({\nu_2}^3/\epsilon_2)^{1/2}}\ ,\ \frac{H_2}{({\nu_2}^3/\epsilon_2)^{1/4}}\ ,\ \frac{g}{({\epsilon_2}^3/\nu_2)^{1/4}},$$

$$\frac{\Delta P_2}{\rho_2(\epsilon_2\nu_2)^{1/2}}\ ,\ \frac{l_2}{({\nu_2}^3/\epsilon_2)^{1/4}}) \tag{4}$$

$$Zone\ 3 : c_1 = \mathcal{F}_3\ (\frac{\bar{u}_1}{(\epsilon_1\nu_1)^{1/4}}\ ,\ \frac{A_1}{({\nu_1}^3/\epsilon_1)^{1/2}}\ ,\ \frac{H_1}{({\nu_1}^3/\epsilon_1)^{1/4}}\ ,\ \frac{g}{({\epsilon_1}^3/\nu_1)^{1/4}}\ ,$$

$$\frac{A}{({\nu_1}^3/\epsilon_1)^{1/2}}\ ,\ \frac{\Delta P_1}{\rho_1(\epsilon_1\nu_1)^{1/2}}\ ,\ \frac{l_1}{({\nu_1}^3/\epsilon_1)^{1/4}}). \tag{5}$$

Note that $\frac{\bar{u}_i}{(\epsilon_i\nu_i)^{1/4}} \cdot \frac{l_i}{({\nu_i}^3/\epsilon_i)^{1/4}} = Re_i.$

Future Research

A miniature flow visualization model for the simulation of fiber mixing in a white water silo was recently designed and constructed. However, this model is only used for the qualitative comparison of the flow mixing behaviors of two different pipe designs. To ensure an optimal silo mixing area design, a three-dimensional CFD analysis of turbulent stock mixing is needed to compare different geometry layouts. As our next research step, we would like to address the following questions using the tools of computational simulations:

- what is the optimum nozzle shape?
- how long and what incline angle should the concentric stock pipe have? and
- what is the proper location of the basis weight valve and fan pump?

Acknowledgment

I would like to thank Dr. Michael Marziale and Mr. Ted Anderson of Westvaco Co. for providing me the mill consistency measurements and many helpful suggestions. I am also grateful to Dr. Barry Hojjatie for assistance in the preliminary design of the experimental approach flow system setup.

It is my pleasure to be able to work with Prof. Fred Bloom from Northern Illinois University, whose help on this project is greatly appreciated.

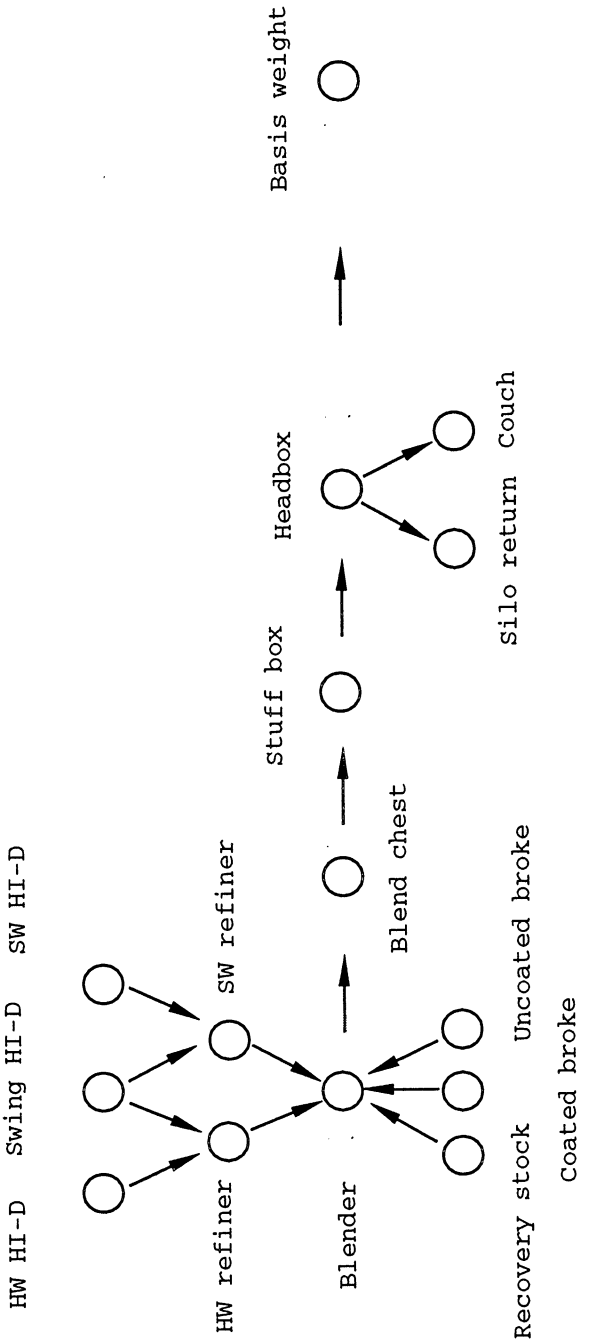

Figure 1: Consistency and basis weight measurements locations.

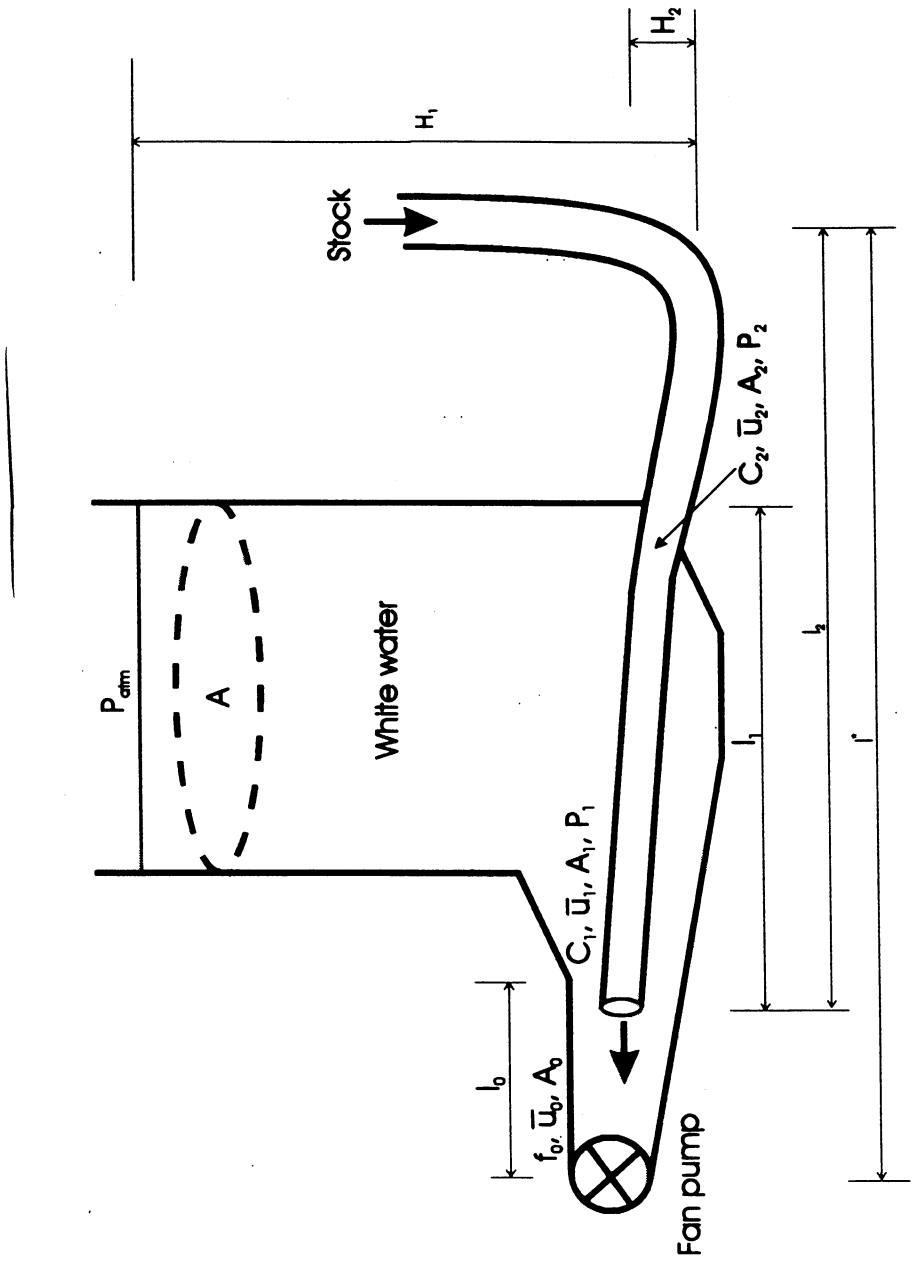

Figure 2: Silo mixing zones.

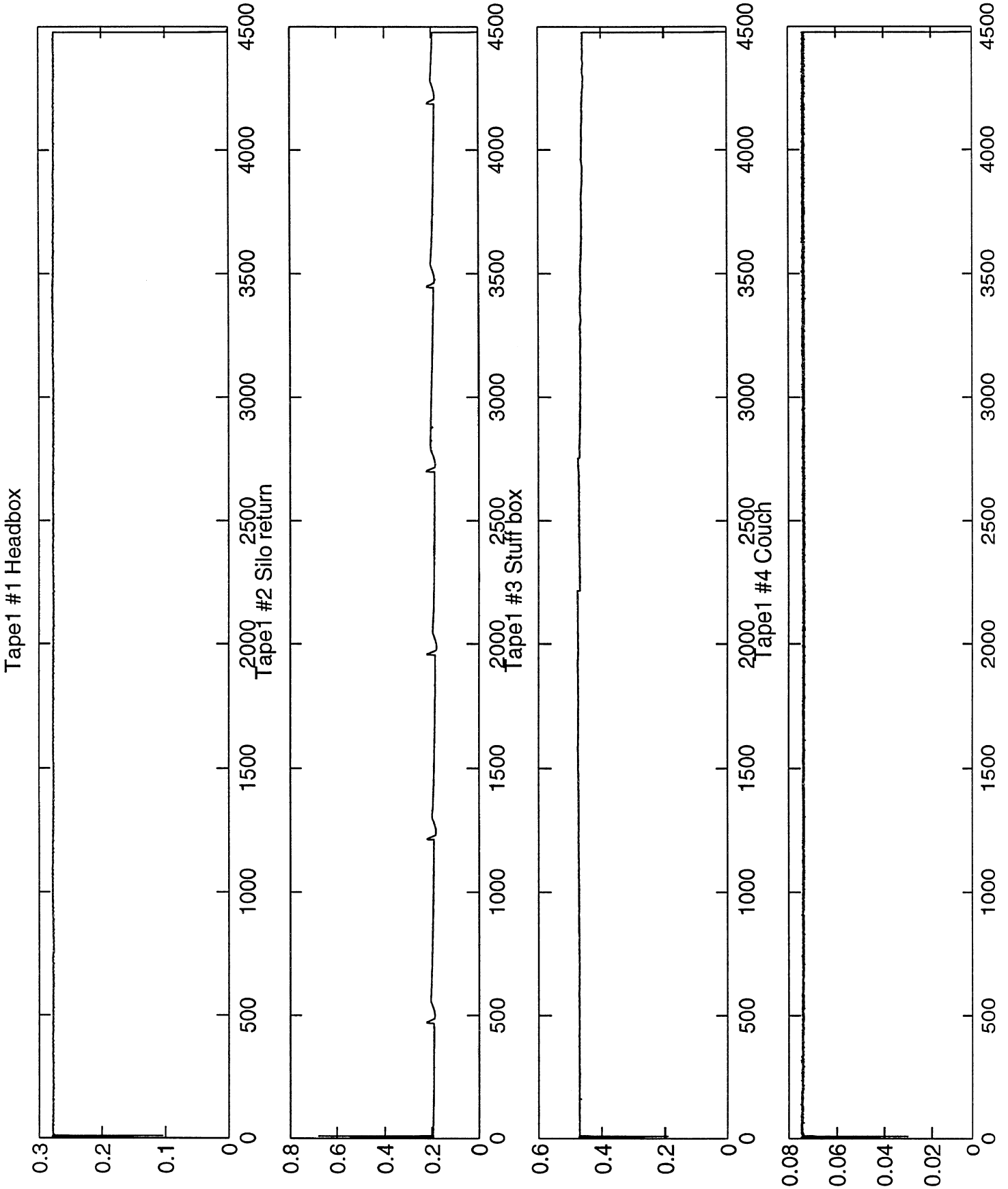
Tape1 #1 Headbox
Tape1 #2 Silo return
Tape1 #3 Stuff box
Tape1 #4 Couch
0.3
0.2
0.1
0
0.8
0.6
0.4
0.2
0
0.6
0.4
0.2
0
0.08
0.06
0.04
0.02
0
0
500
1000
1500
2000
2500
3000
3500
4000
4500

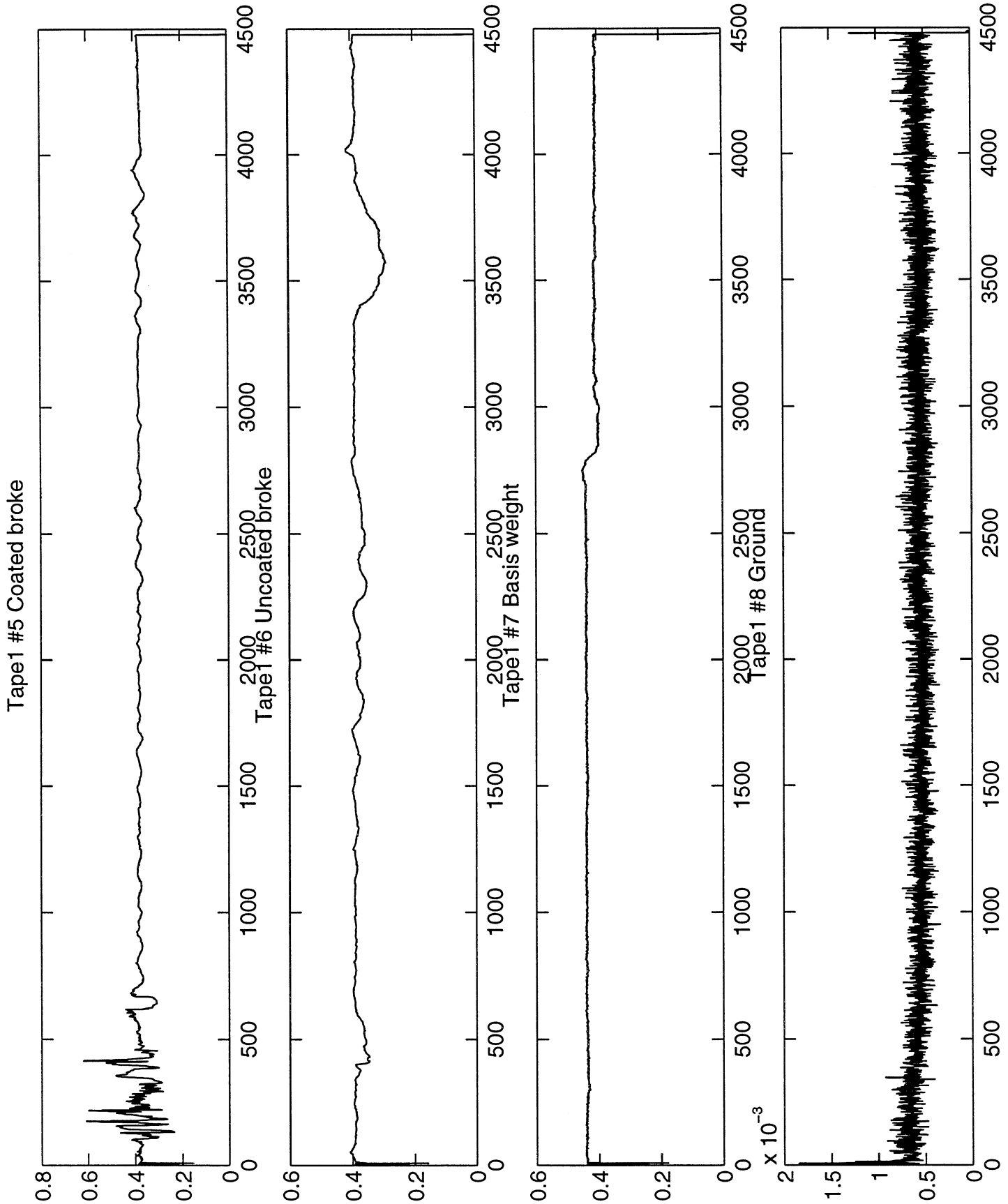
Tape1 #5 Coated broke
Tape1 #6 Uncoated broke
Tape1 #7 Basis weight
Tape1 #8 Ground
x 10^-3

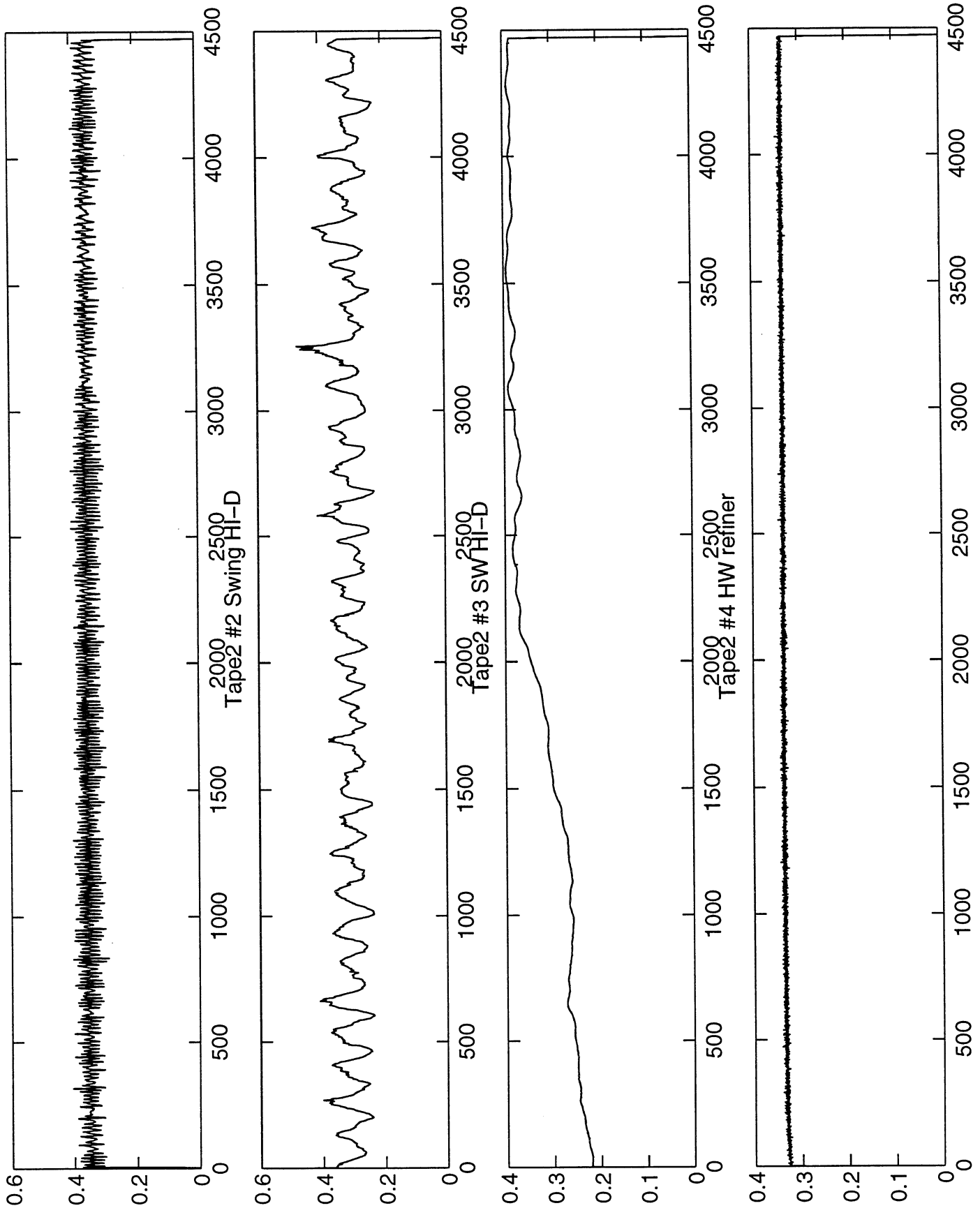
Tape2 #1 HW HI-D
Tape2 #2 Swing HI-D
Tape2 #3 SW HI-D
Tape2 #4 HW refiner
0
500
1000
1500
2000
2500
3000
3500
4000
4500
0.1
0.2
0.3
0.4
0.6

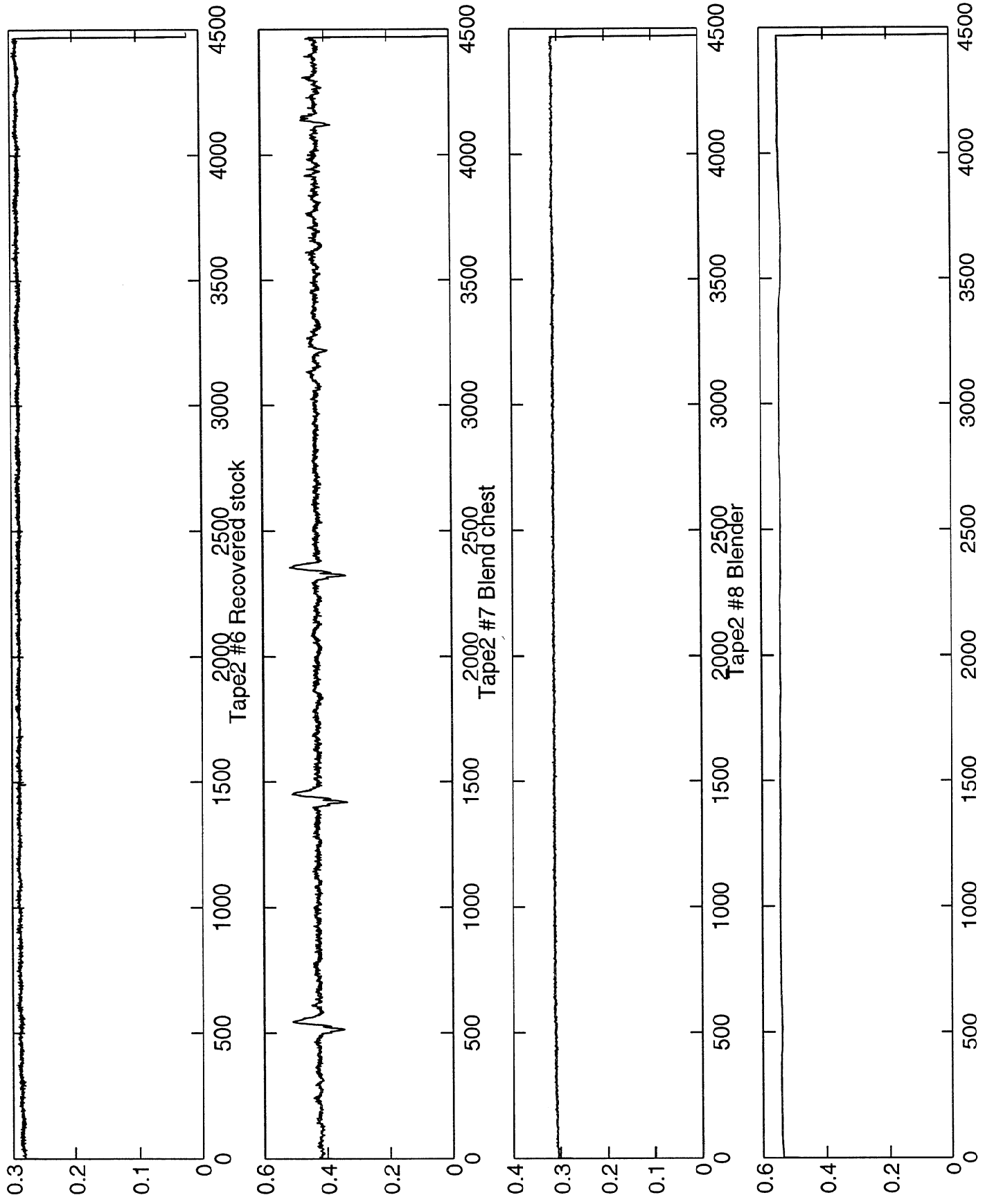
Tape2 #5 SW refiner
Tape2 #6 Recovered stock
Tape2 #7 Blend chest
Tape2 #8 Blender

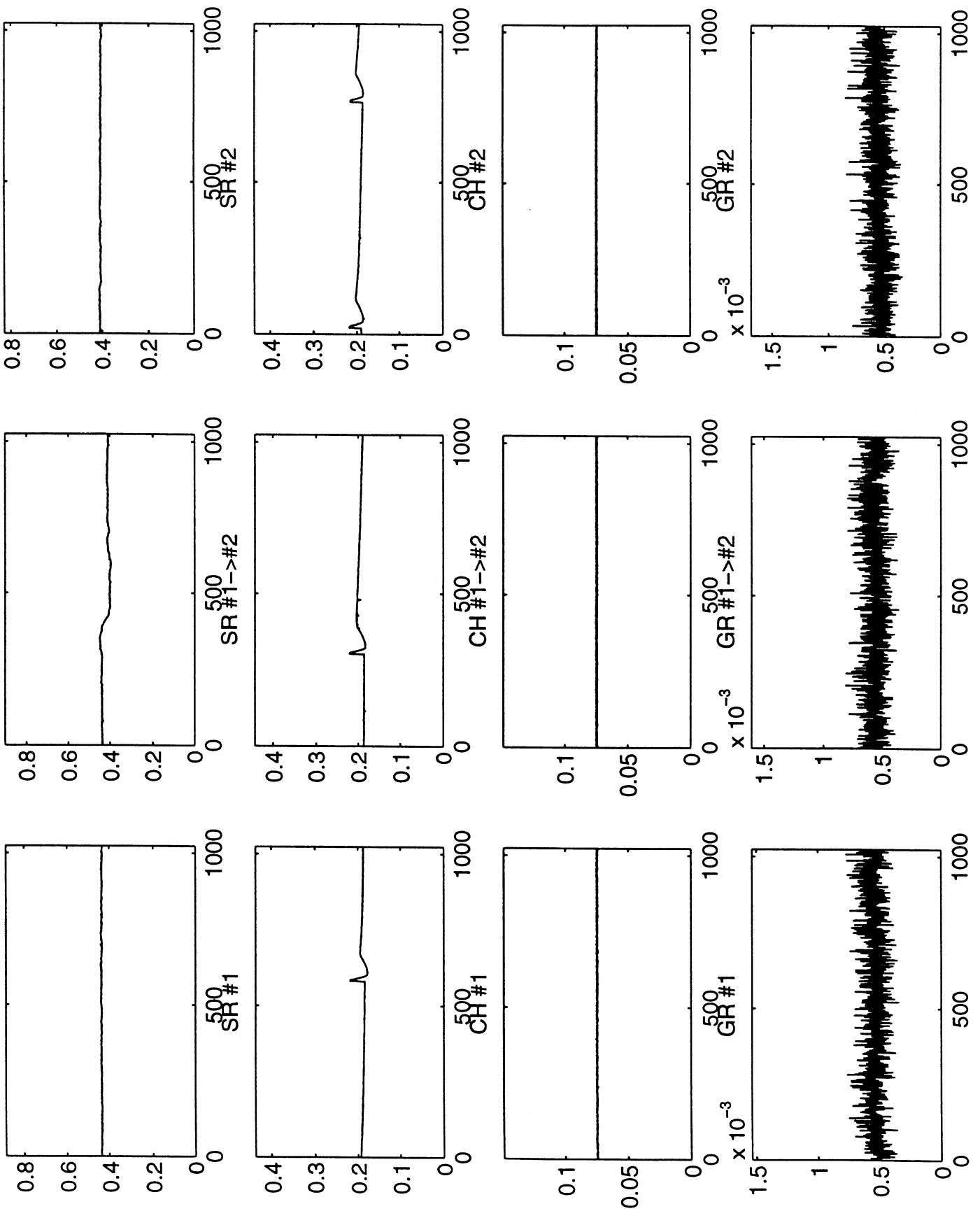
BW #1
SR #1
CH #1
GR #1
BW #1->#2
SR #1->#2
CH #1->#2
GR #1->#2
BW #2
SR #2
CH #2
GR #2
x 10^-3

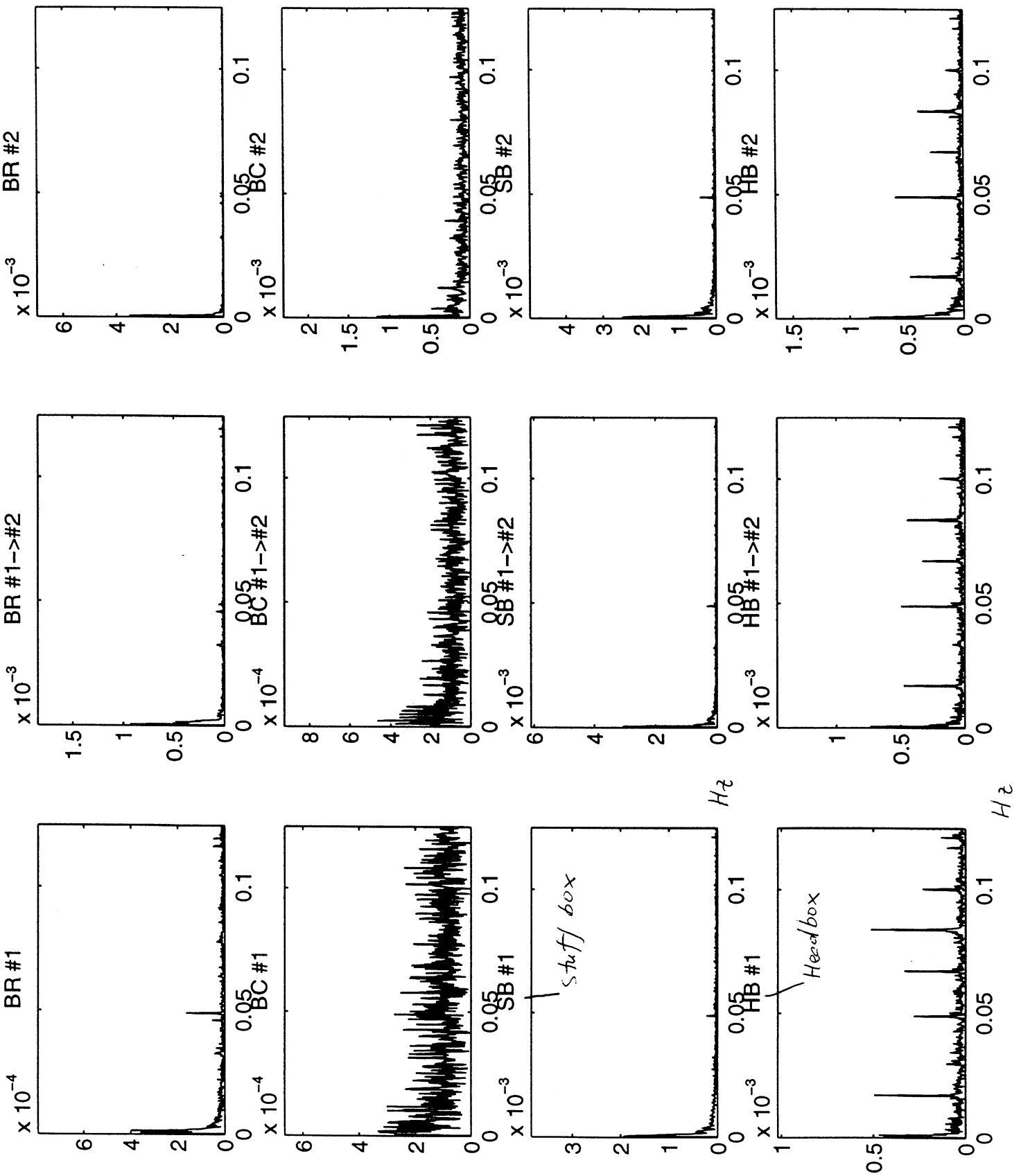
BR #1
BC #1
SB #1
HB #1
BR #1->#2
BC #1->#2
SB #1->#2
HB #2
BR #2
BC #2
SB #2
HB #2
Stuff box
Head box
Hz
Hz

~0.125 Hz

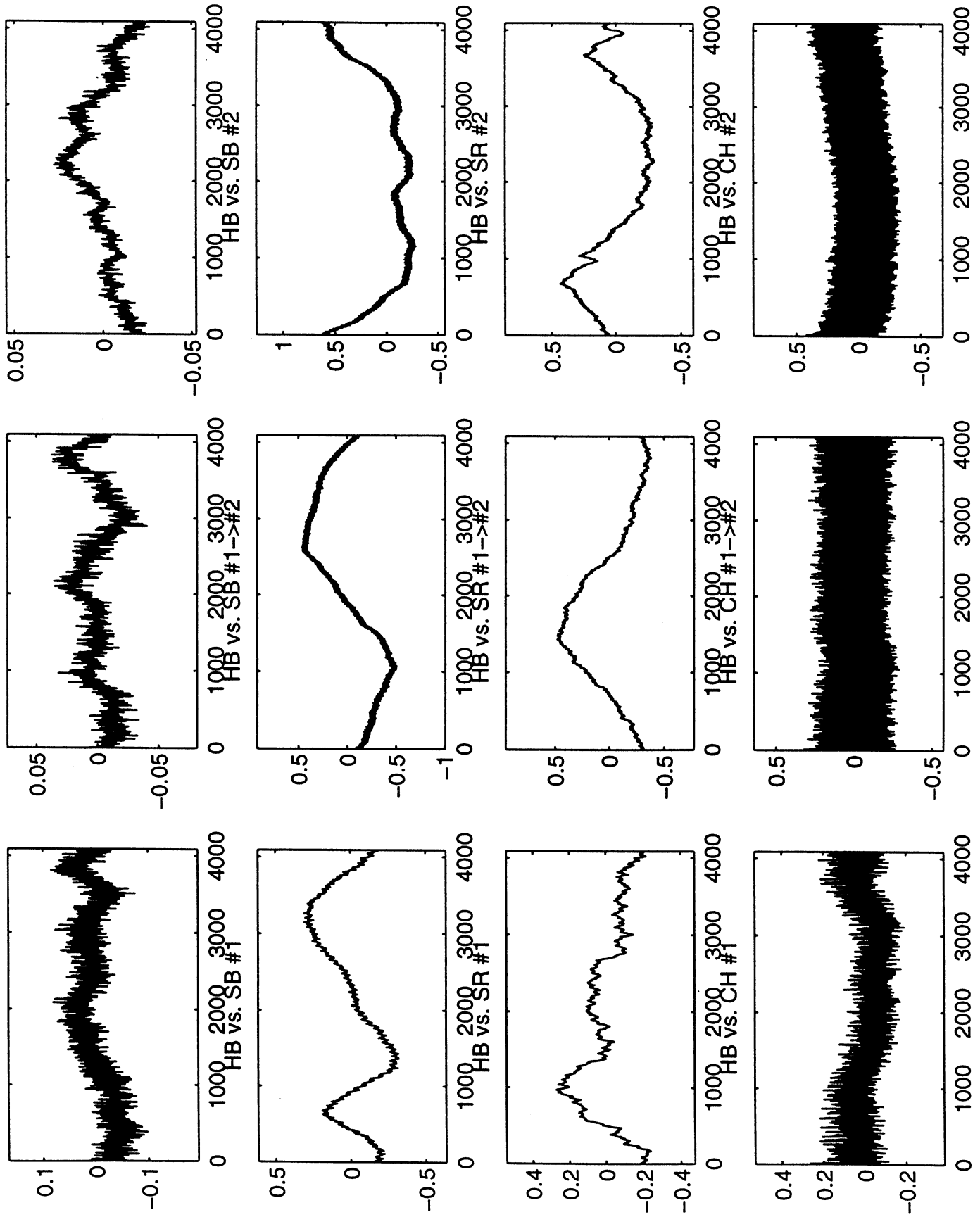
BR vs. HW R #1
BR vs. HW R #1->#2
BR vs. HW R #2
HB vs. SB #1
HB vs. SR #1
HB vs. CH #1
HB vs. SB #1->#2
HB vs. SR #1->#2
HB vs. CH #1->#2
HB vs. SB #2
HB vs. SR #2
HB vs. CH #2

~0.125 Hz

~0.125 Hz

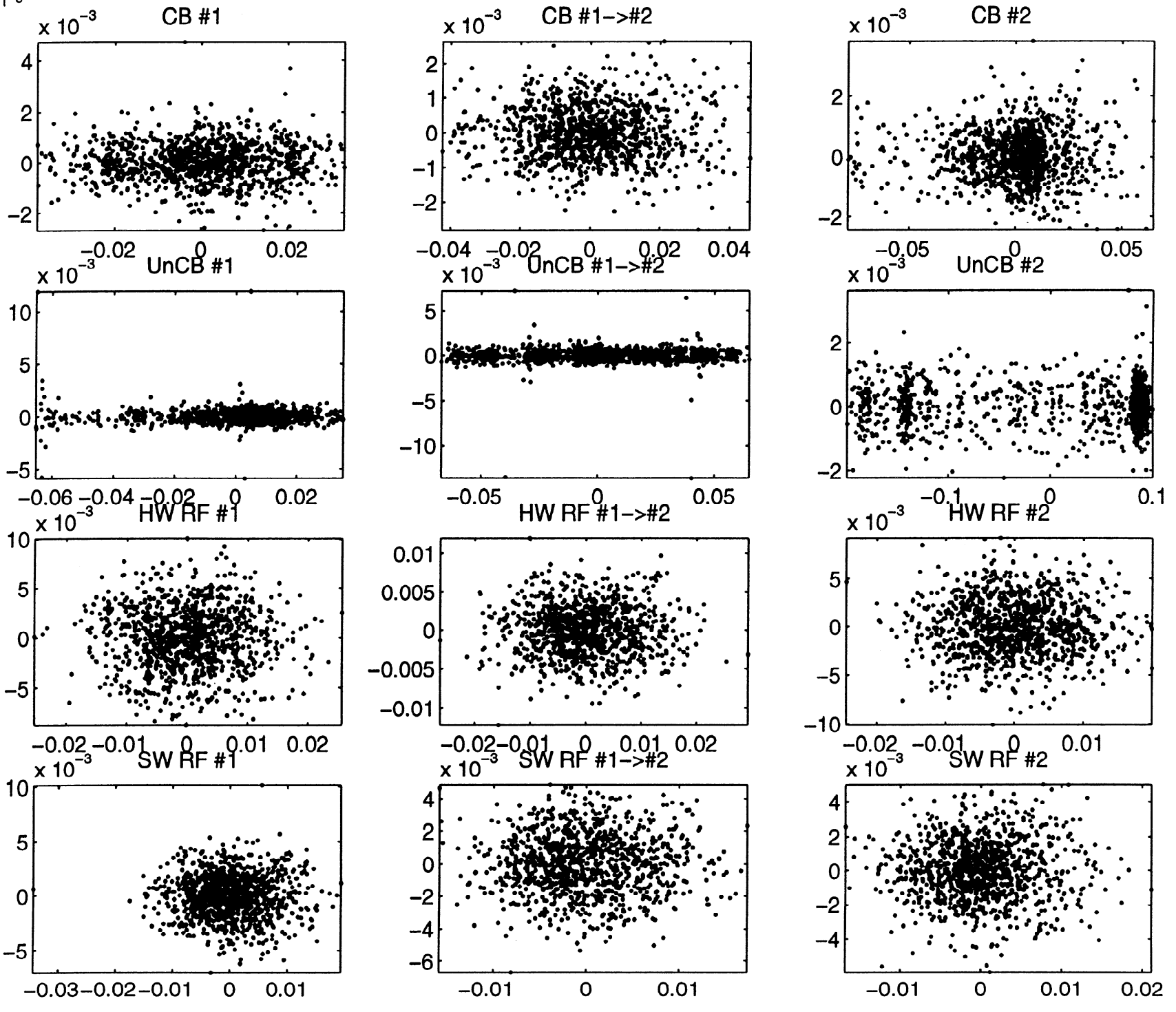
CB #1
CB #1->#2
CB #2
UnCB #1
UnCB #1->#2
UnCB #2
HW RF #1
HW RF #1->#2
HW RF #2
SW RF #1
SW RF #1->#2
SW RF #2

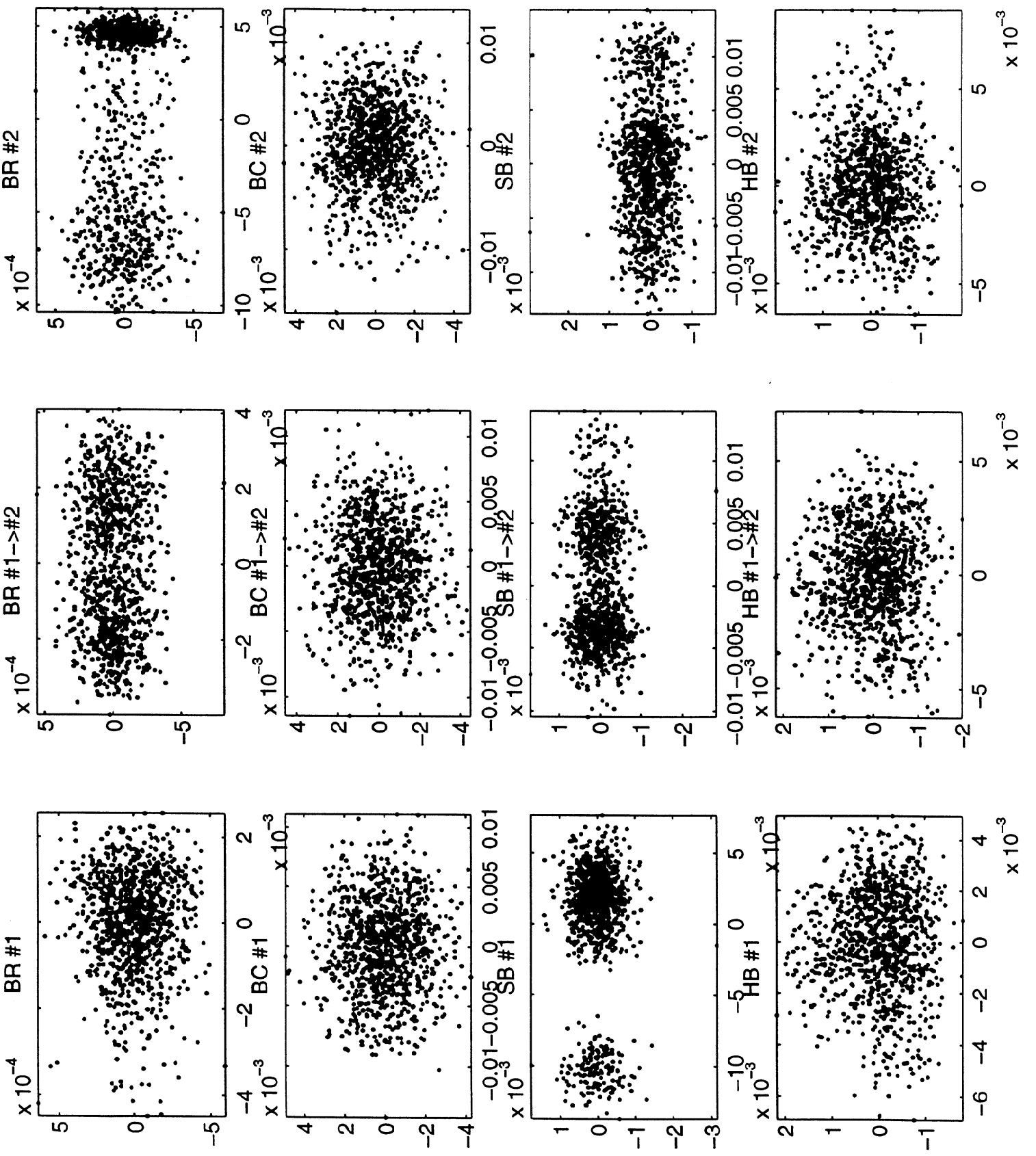

~0.125 Hz

~0.125 Hz

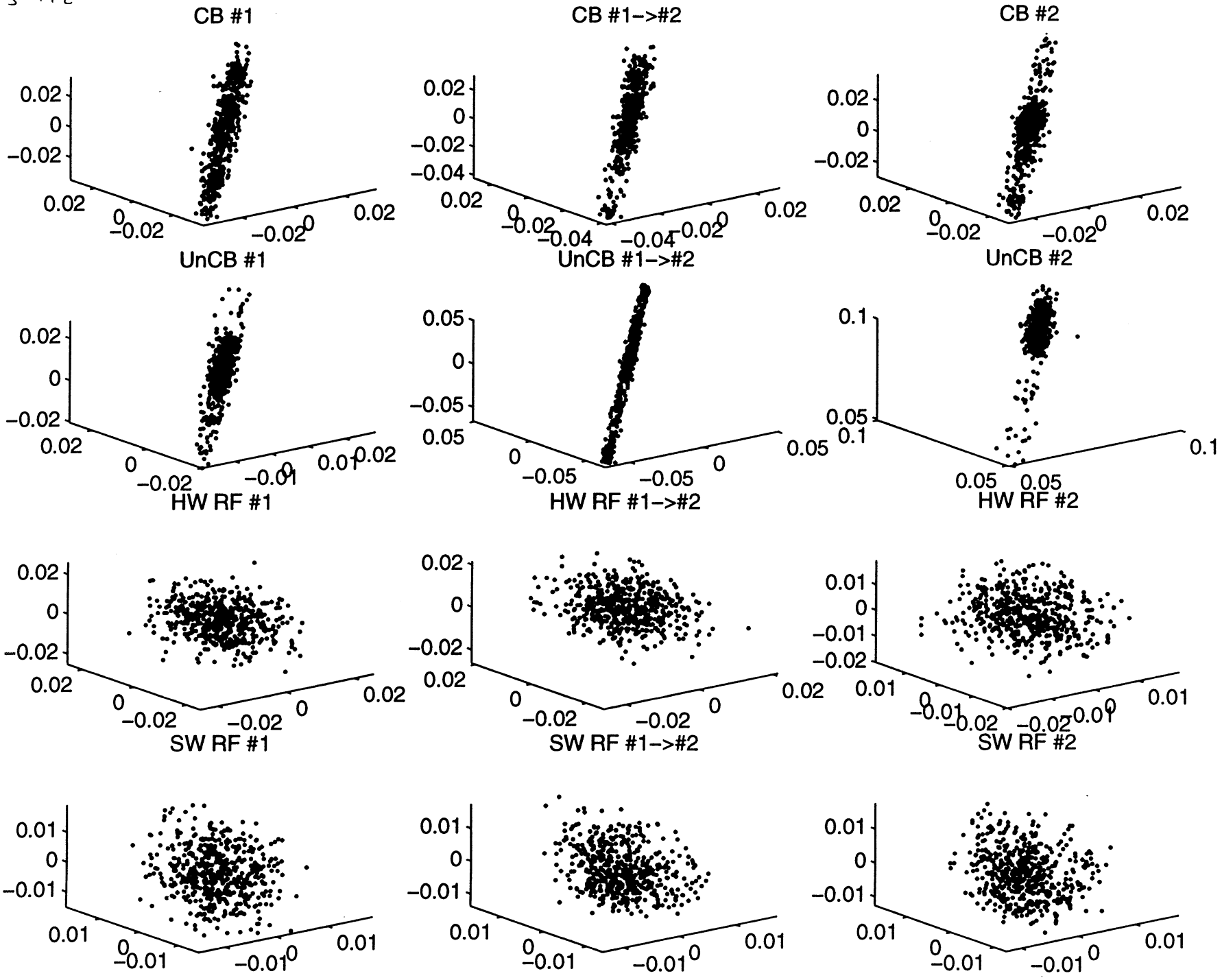
CB #1
CB #1->#2
CB #2
UnCB #1
UnCB #1->#2
UnCB #2
HW RF #1
HW RF #1->#2
HW RF #2
SW RF #1
SW RF #1->#2
SW RF #2

~0.125 Hz

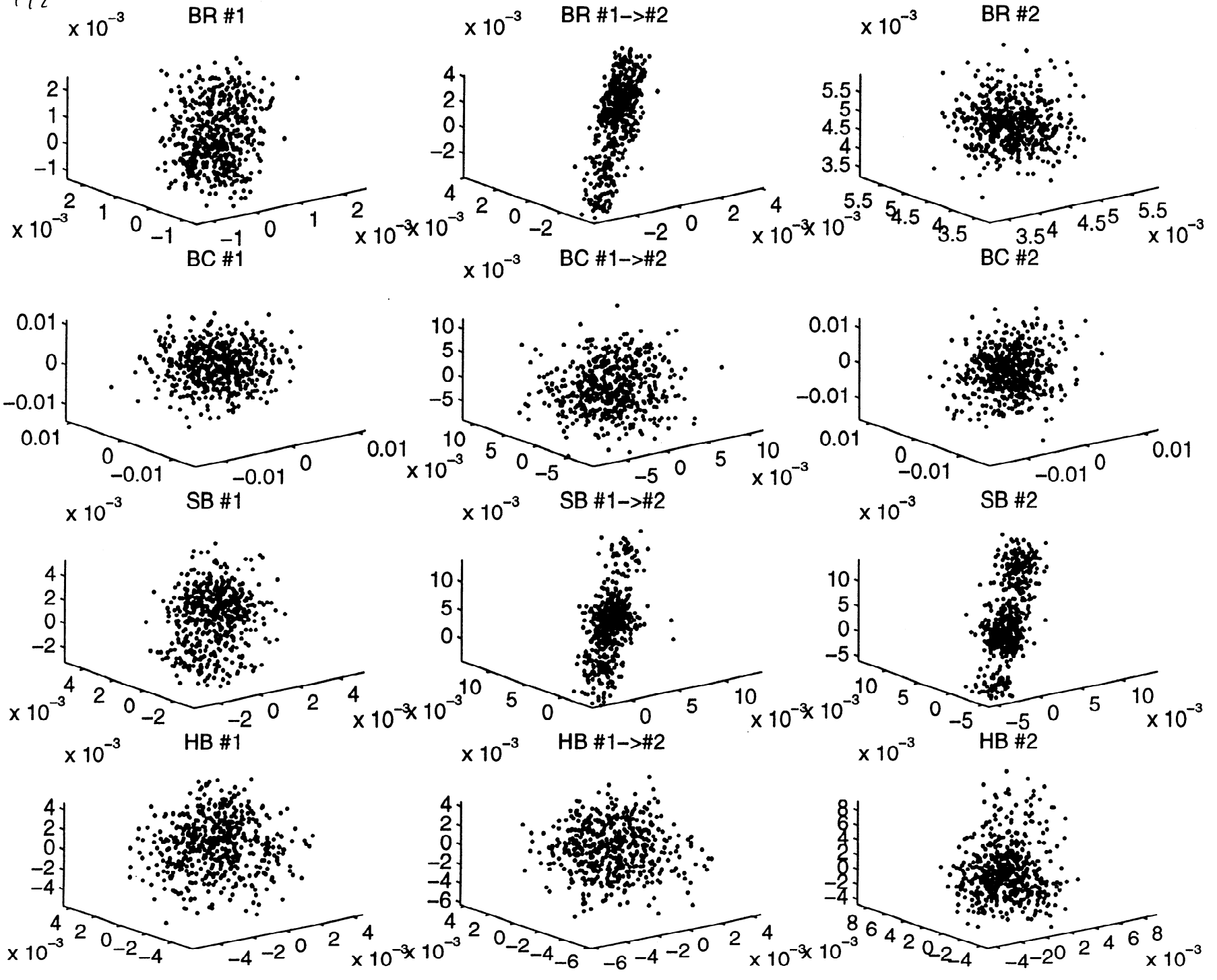

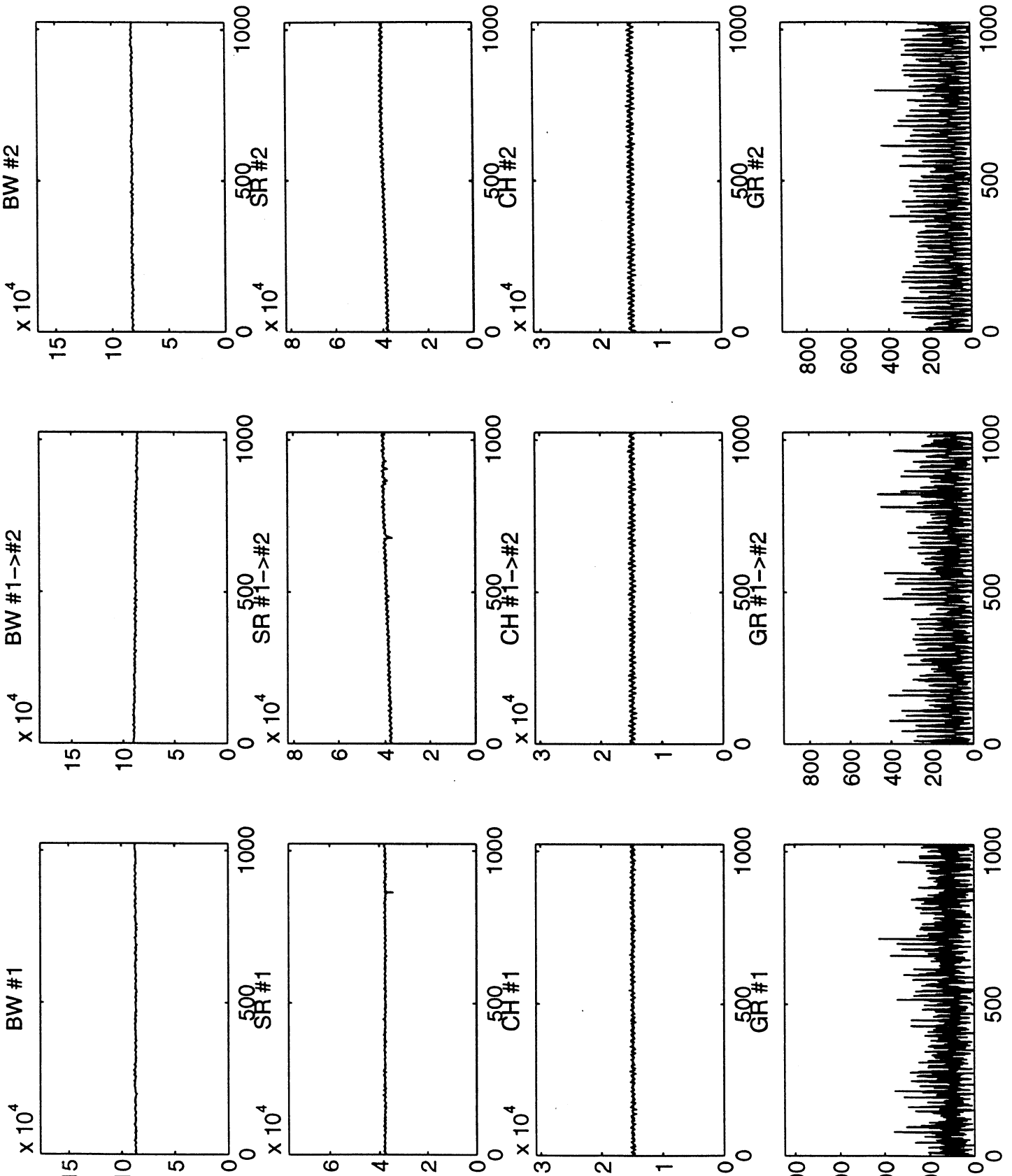

~2.5Hz

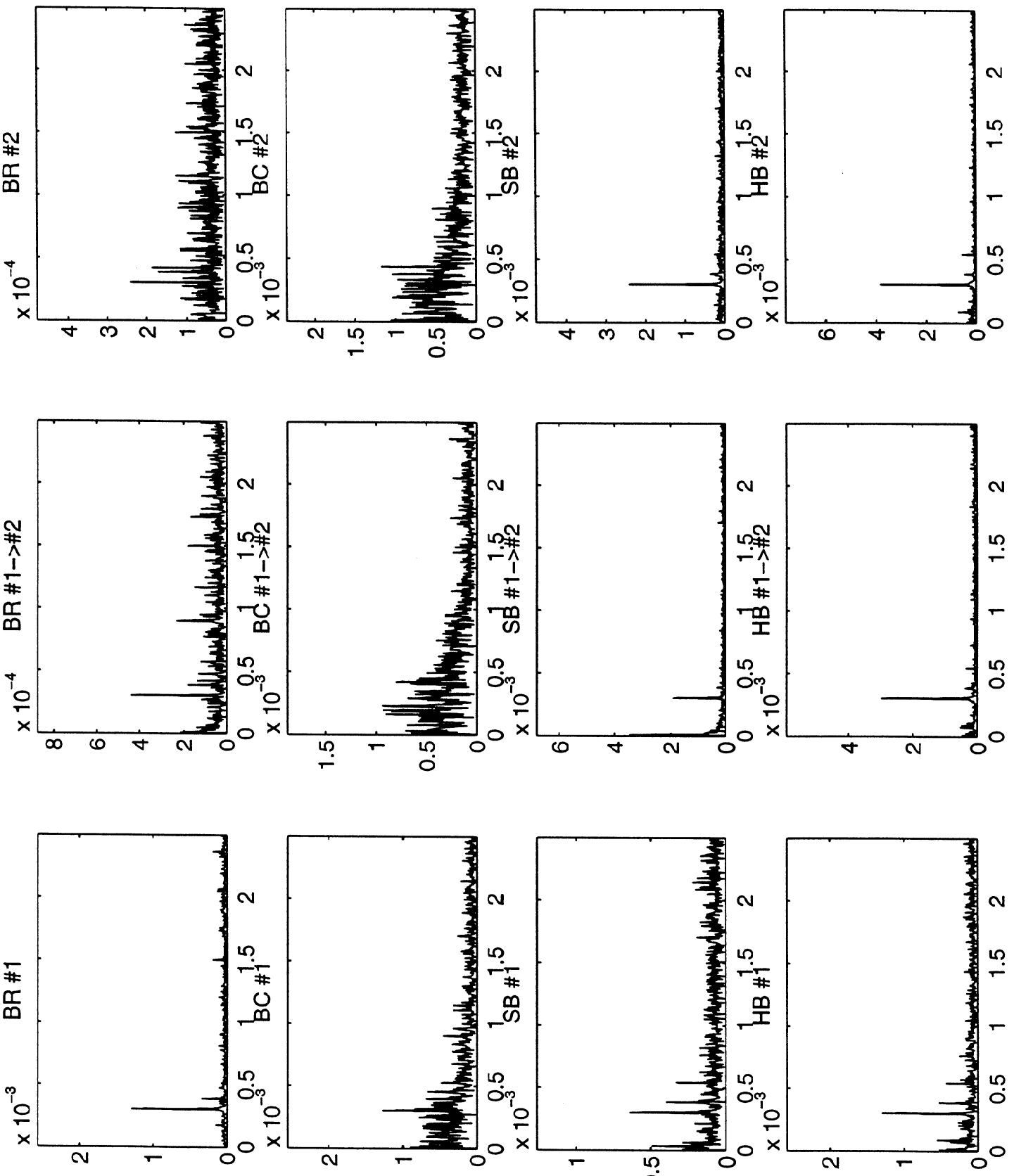

~2.5 Hz

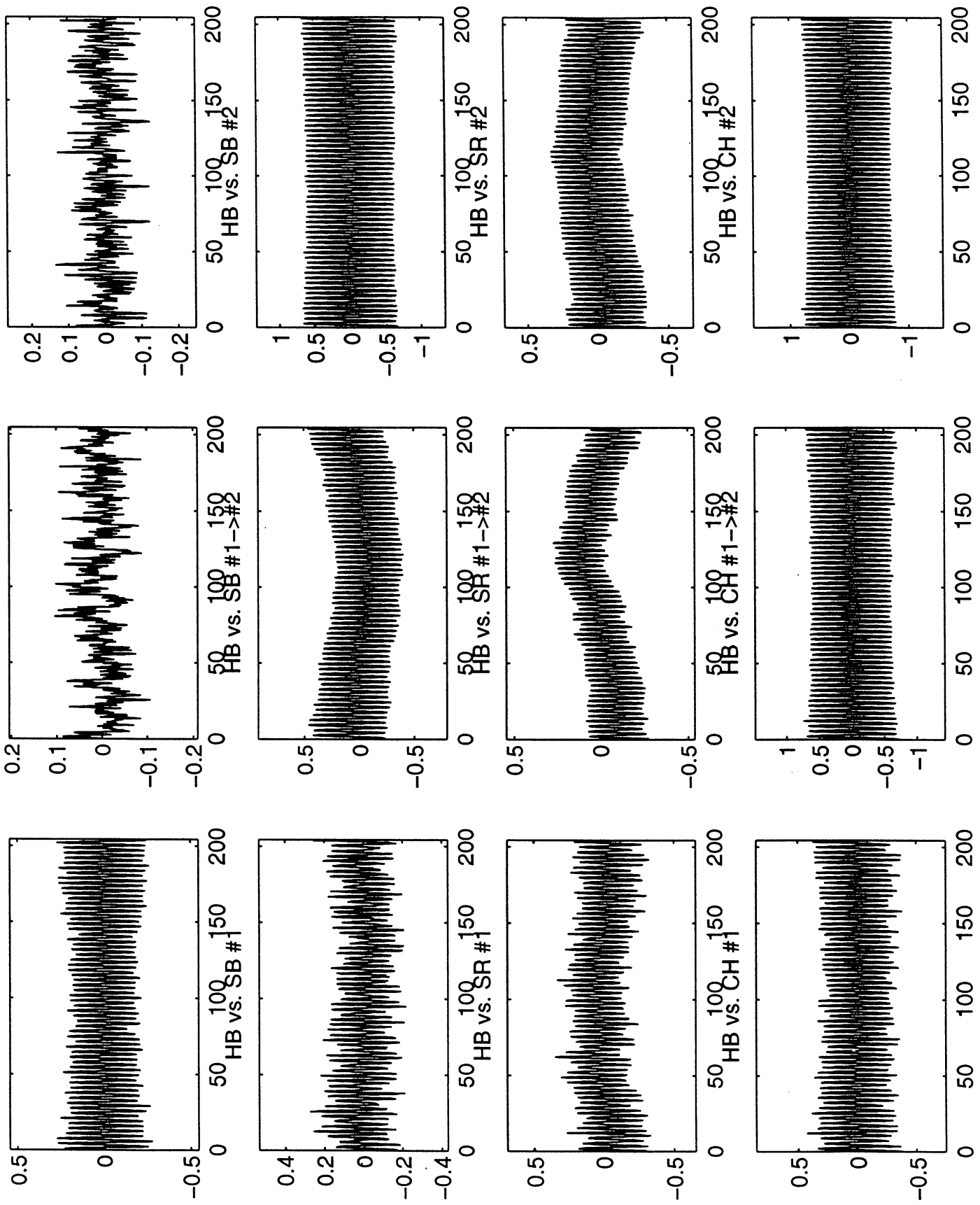
BR vs. HW R #1
HB vs. SB #1
HB vs. SR #1
HB vs. CH #1
BR vs. HW R #1->#2
HB vs. SB #1->#2
HB vs. SR #1->#2
HB vs. CH #1->#2
BR vs. HW R #2
HB vs. SB #2
HB vs. SR #2
HB vs. CH #2

~2.5Hz

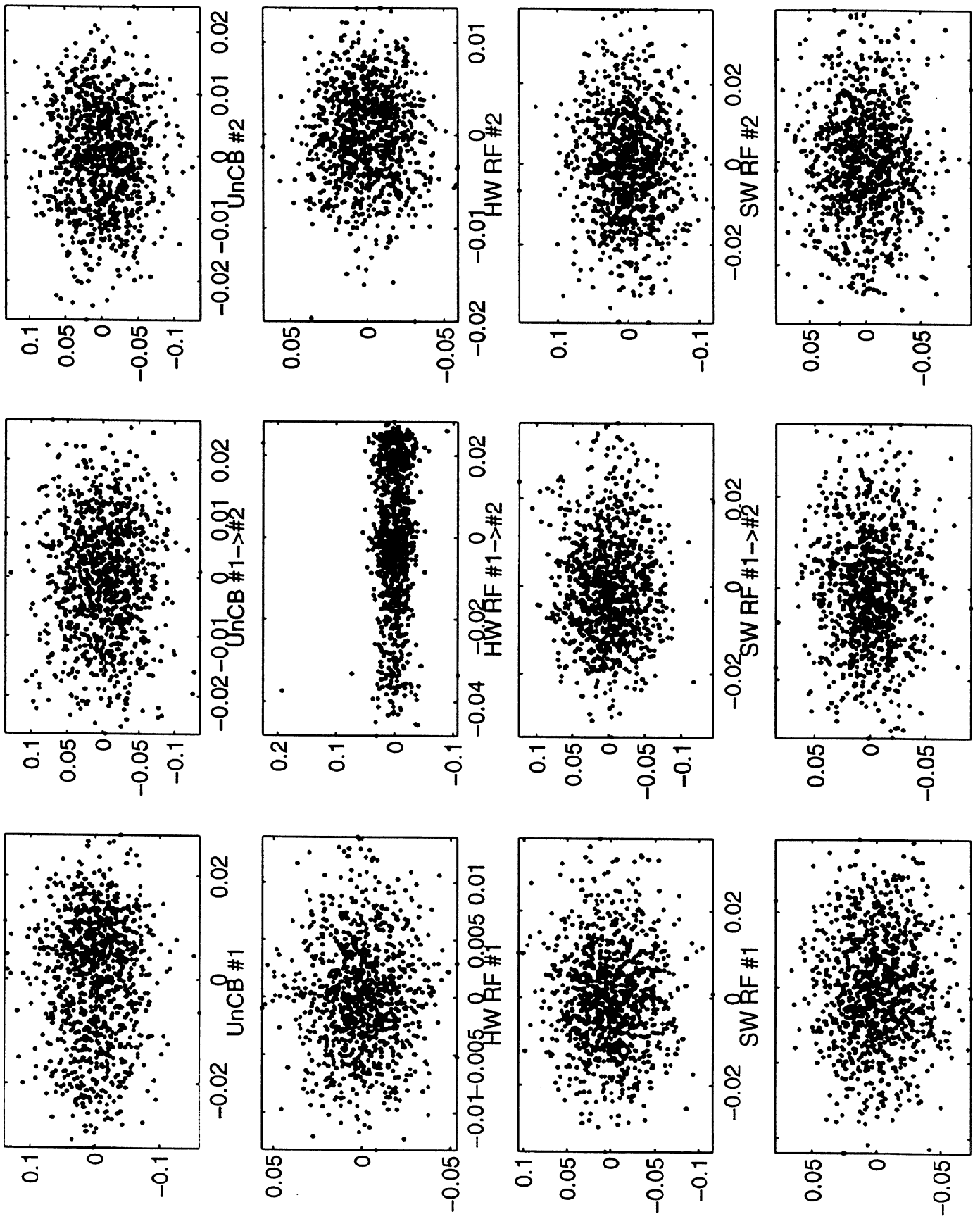
CB #1
CB #1->#2
CB #2
UnCB #1
UnCB #1->#2
UnCB #2
HW RF #1
HW RF #1->#2
HW RF #2
SW RF #1
SW RF #1->#2
SW RF #2

~2.5 Hz

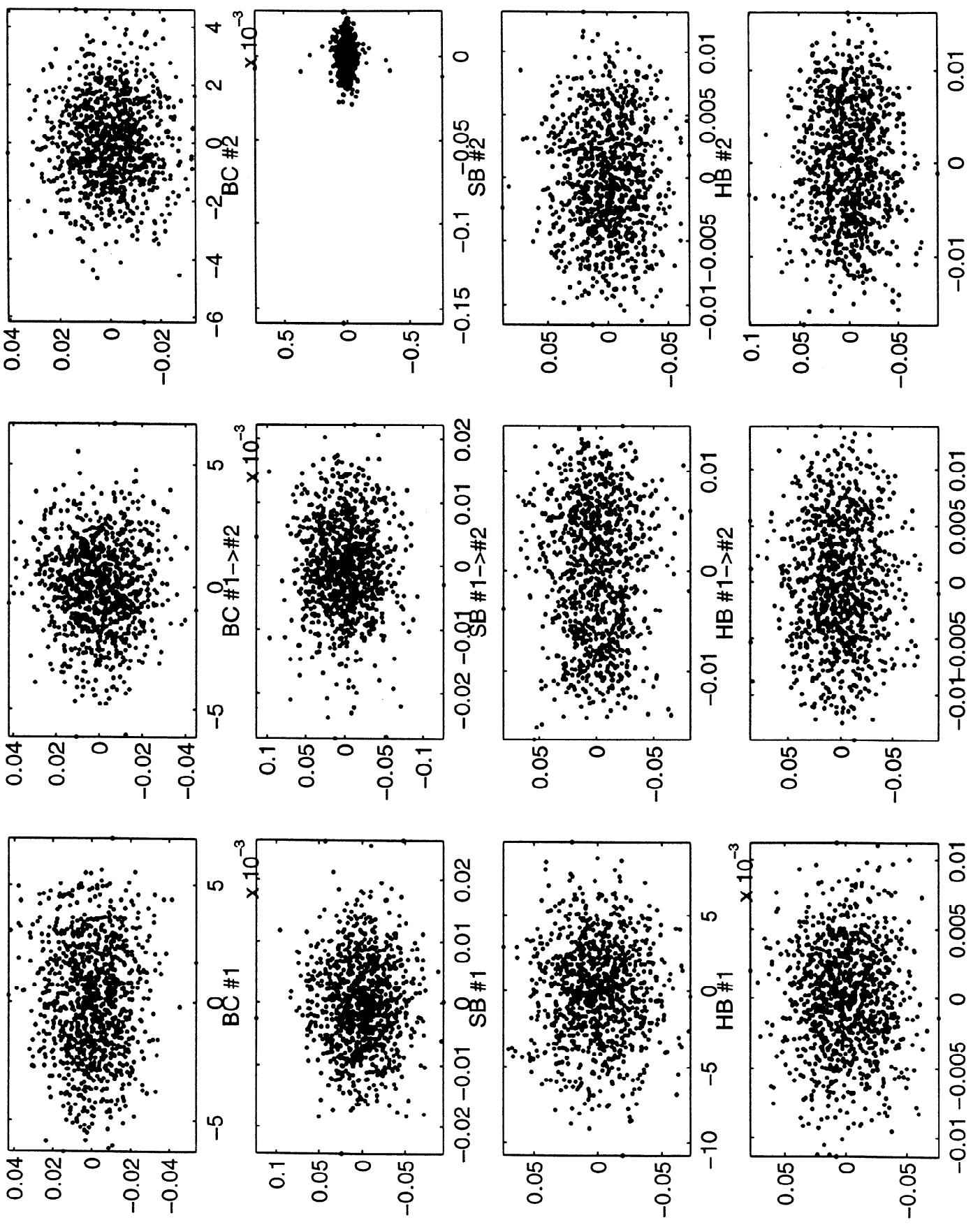
~2.5 Hz
BR #1
BC #1
SB #1
HB #1
BR #1->#2
BC #1->#2
SB #1->#2
HB #1->#2
BR #2
BC #2
SB #2
HB #2
x 10^-3

~2.5Hz

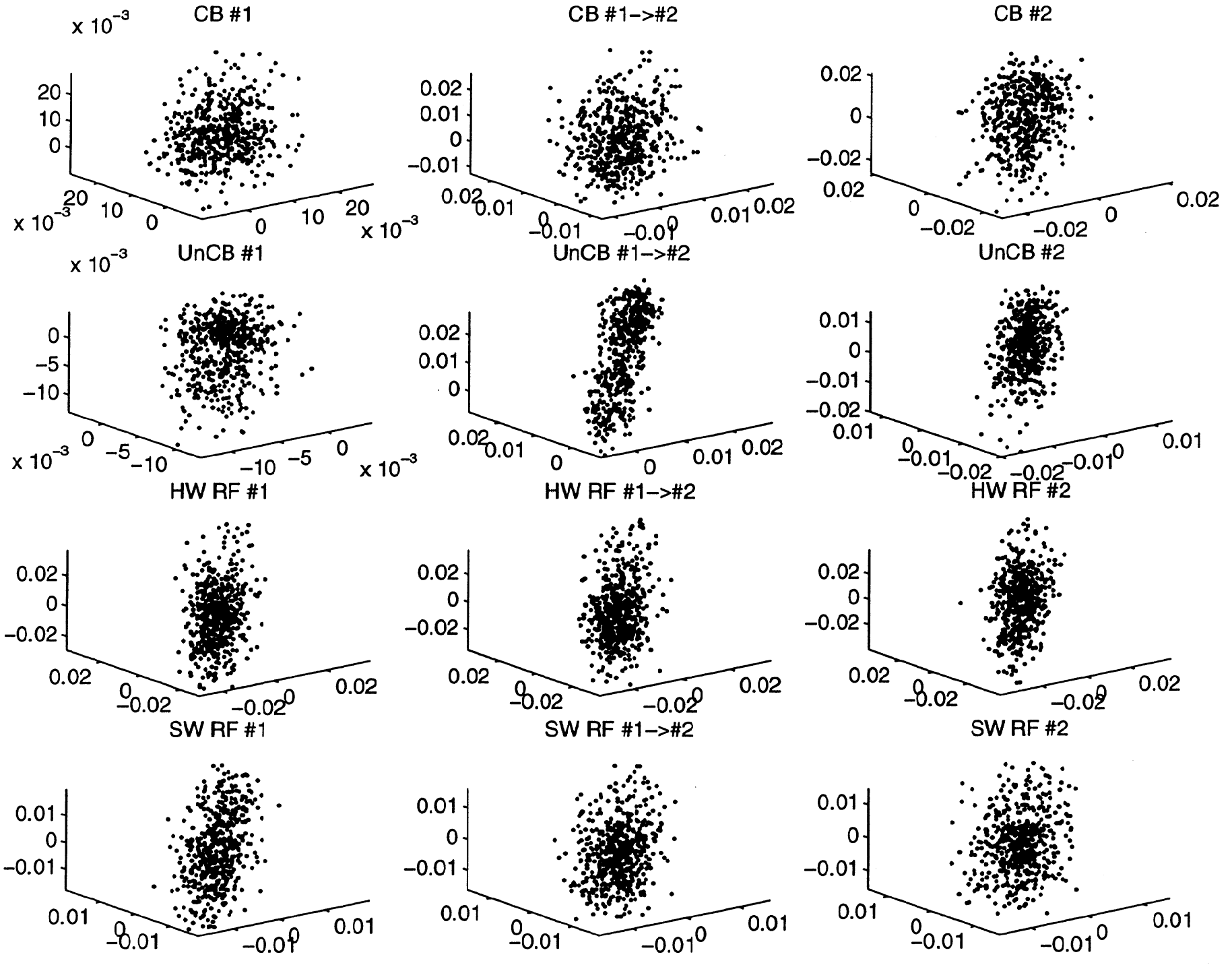
CB #1
CB #1->#2
CB #2
UnCB #1
UnCB #1->#2
UnCB #2
HW RF #1
HW RF #1->#2
HW RF #2
SW RF #1
SW RF #1->#2
SW RF #2

~2-5Hz

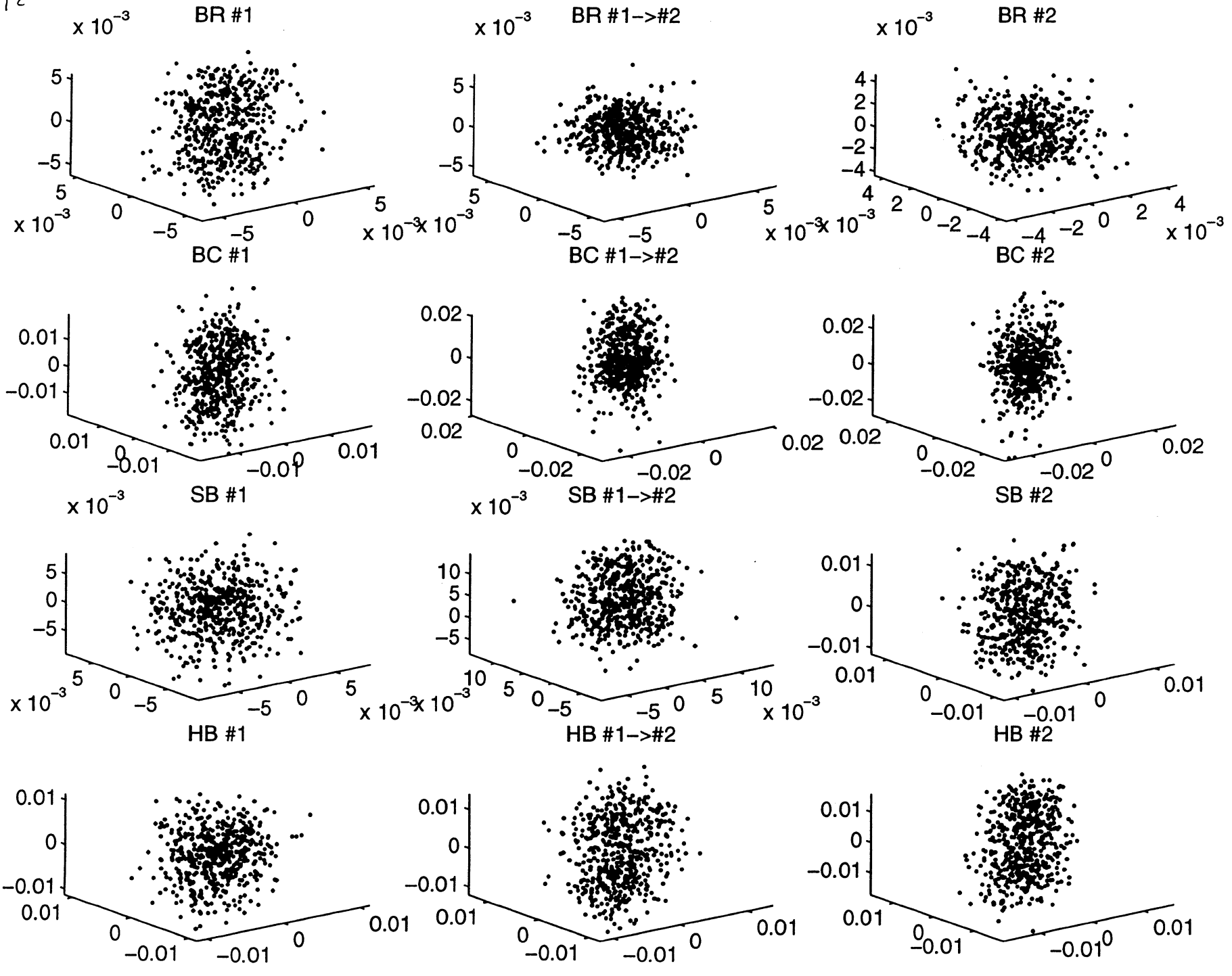

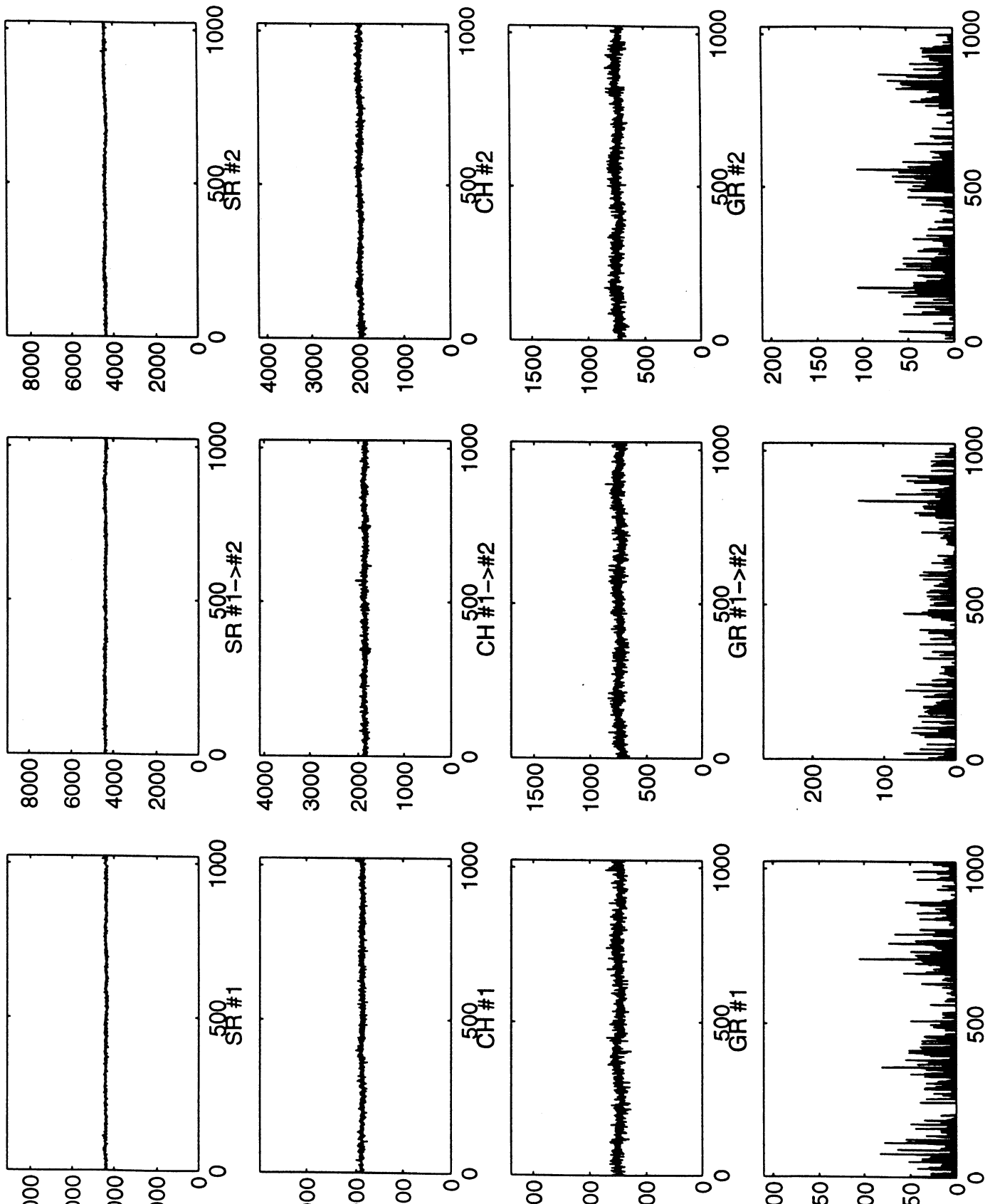

~ 50 Hz

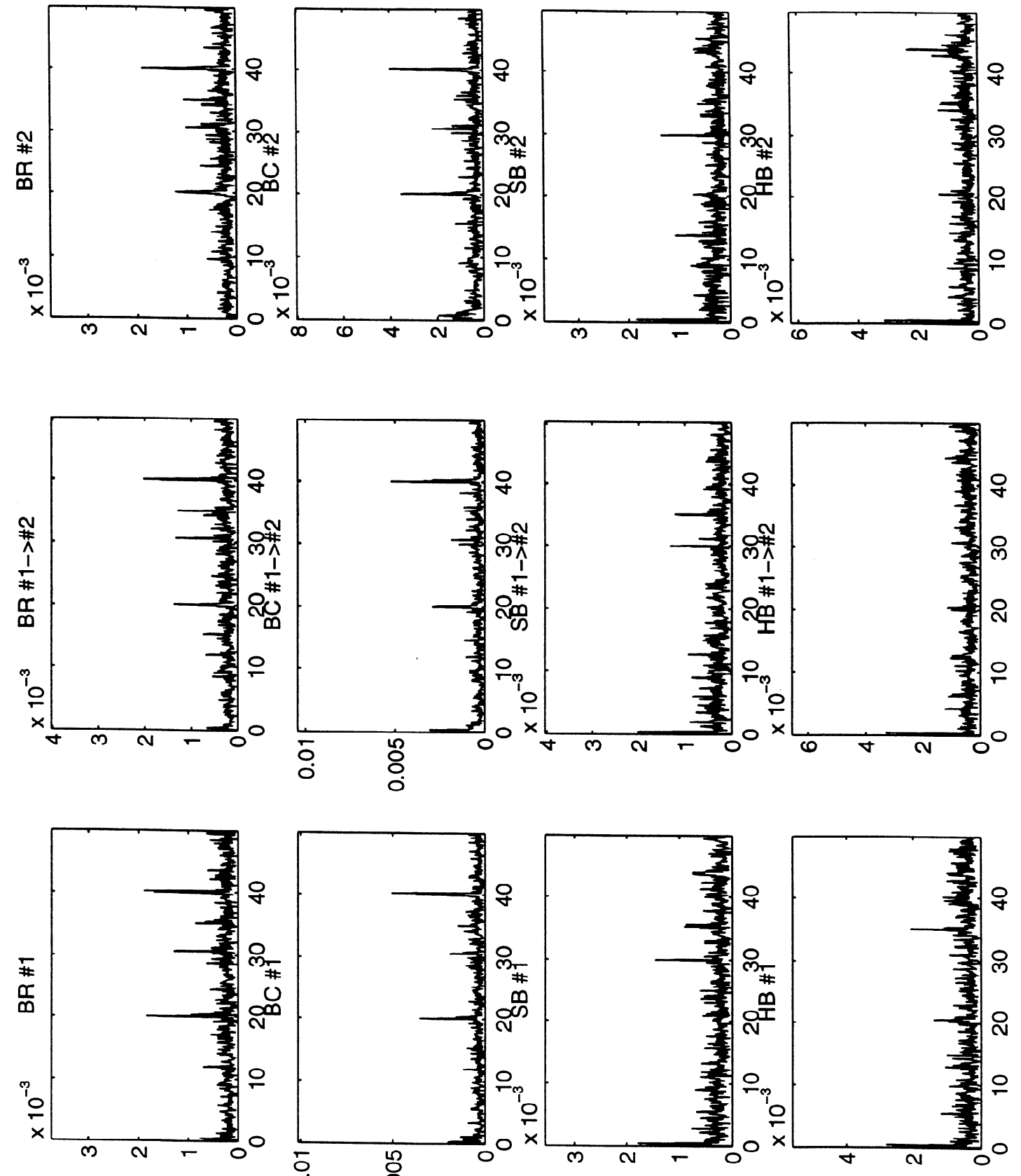

~ 50 Hz

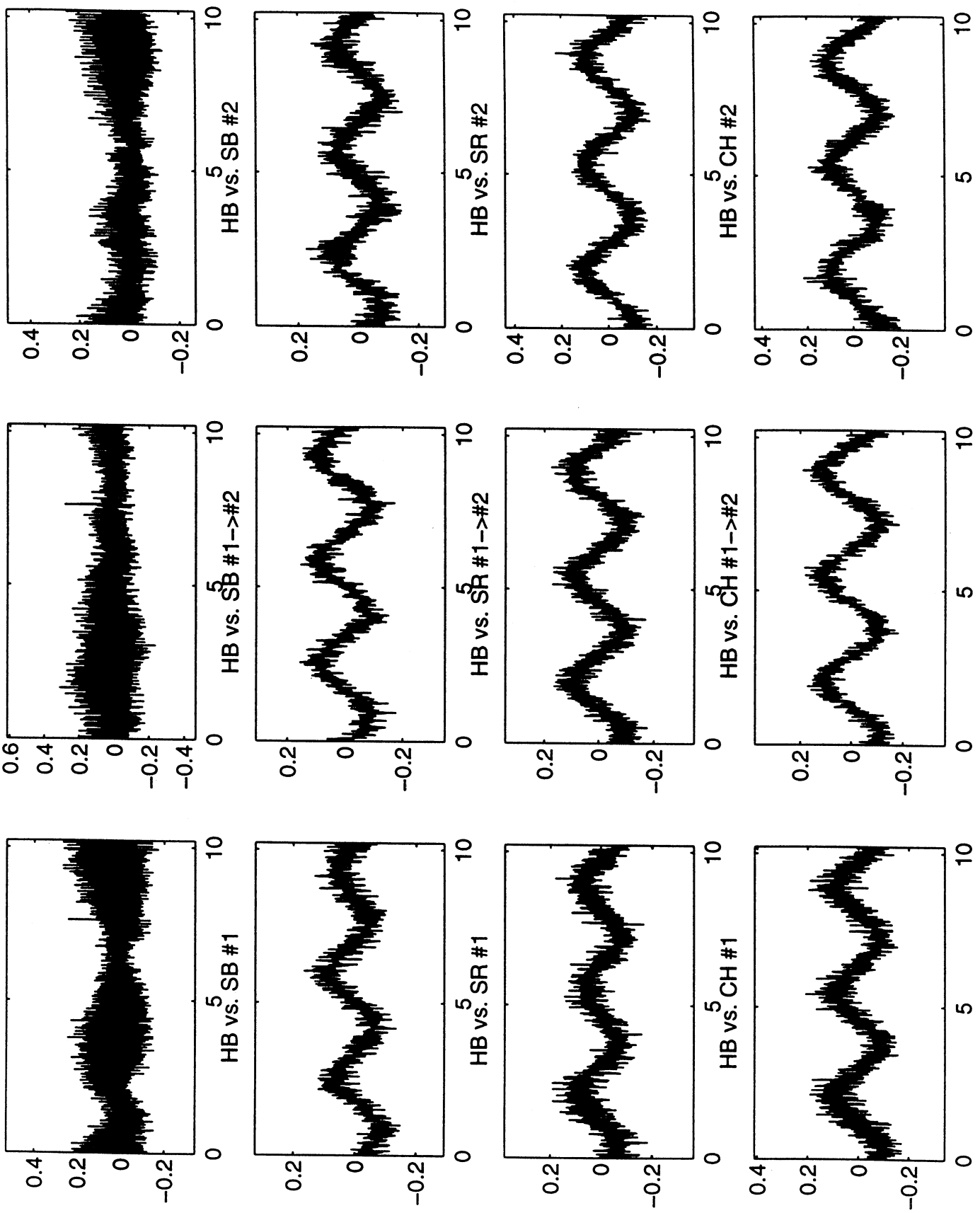
BR vs. HW R #1
BR vs. HW R #1->#2
BR vs. HW R #2
HB vs. SB #1
HB vs. SB #1->#2
HB vs. SB #2
HB vs. SR #1
HB vs. SR #1->#2
HB vs. SR #2
HB vs. CH #1
HB vs. CH #1->#2
HB vs. CH #2

~ 50 Hz

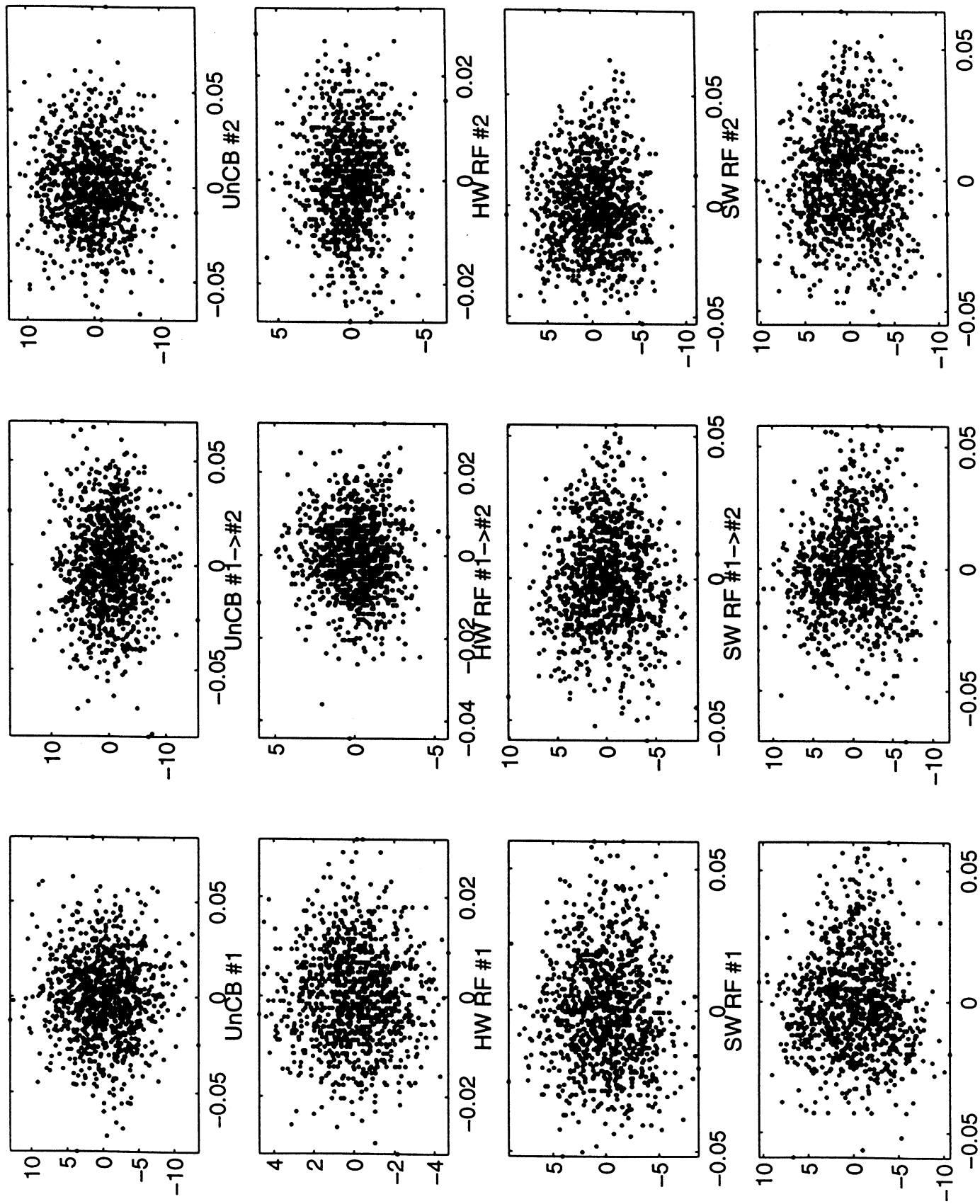
CB #1
UnCB #1
HW RF #1
SW RF #1
CB #1->#2
UnCB #1->#2
HW RF #1->#2
SW RF #1->#2
CB #2
UnCB #2
HW RF #2
SW RF #2

~150 Hz

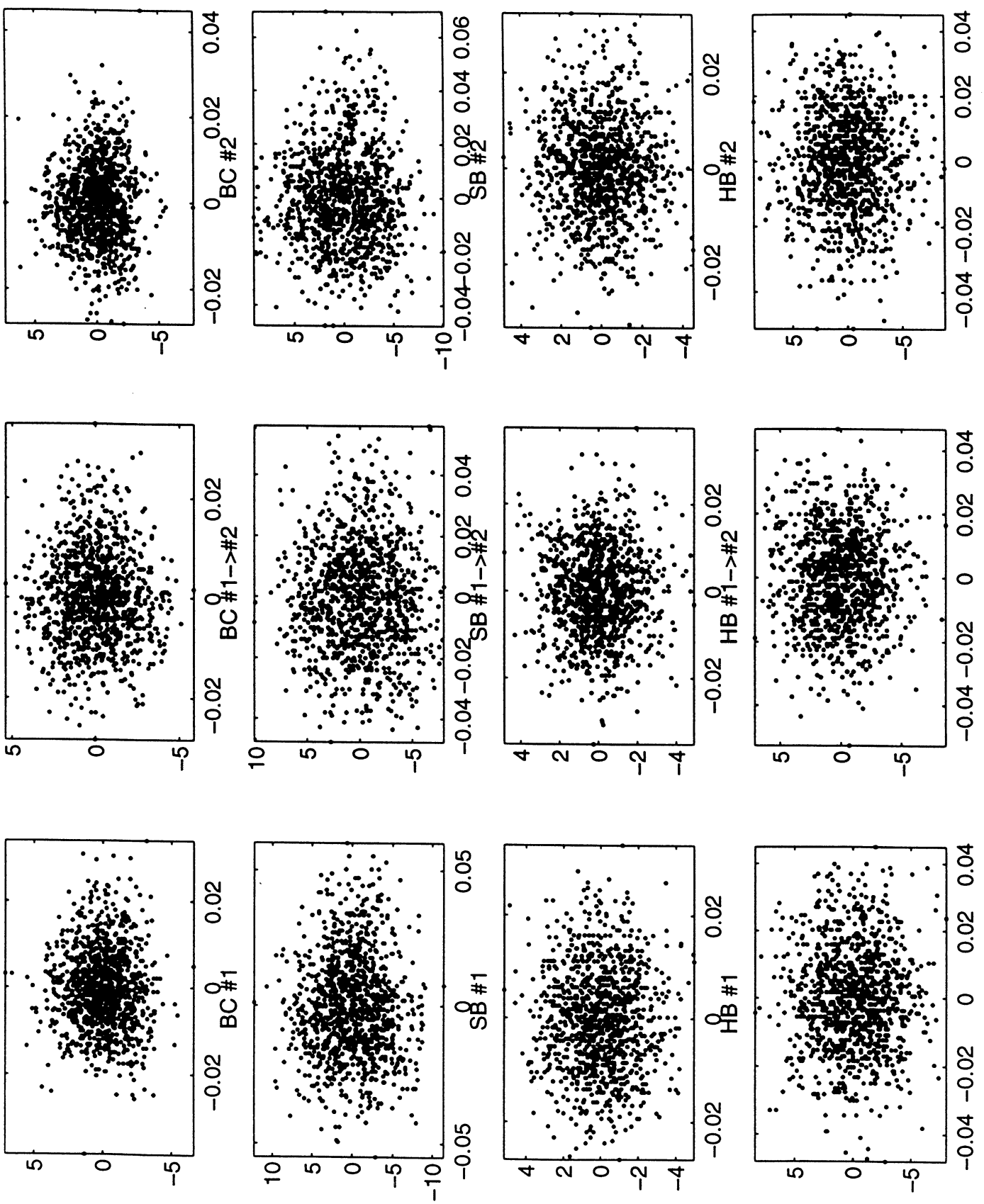

~ 50 Hz

~50 Hz

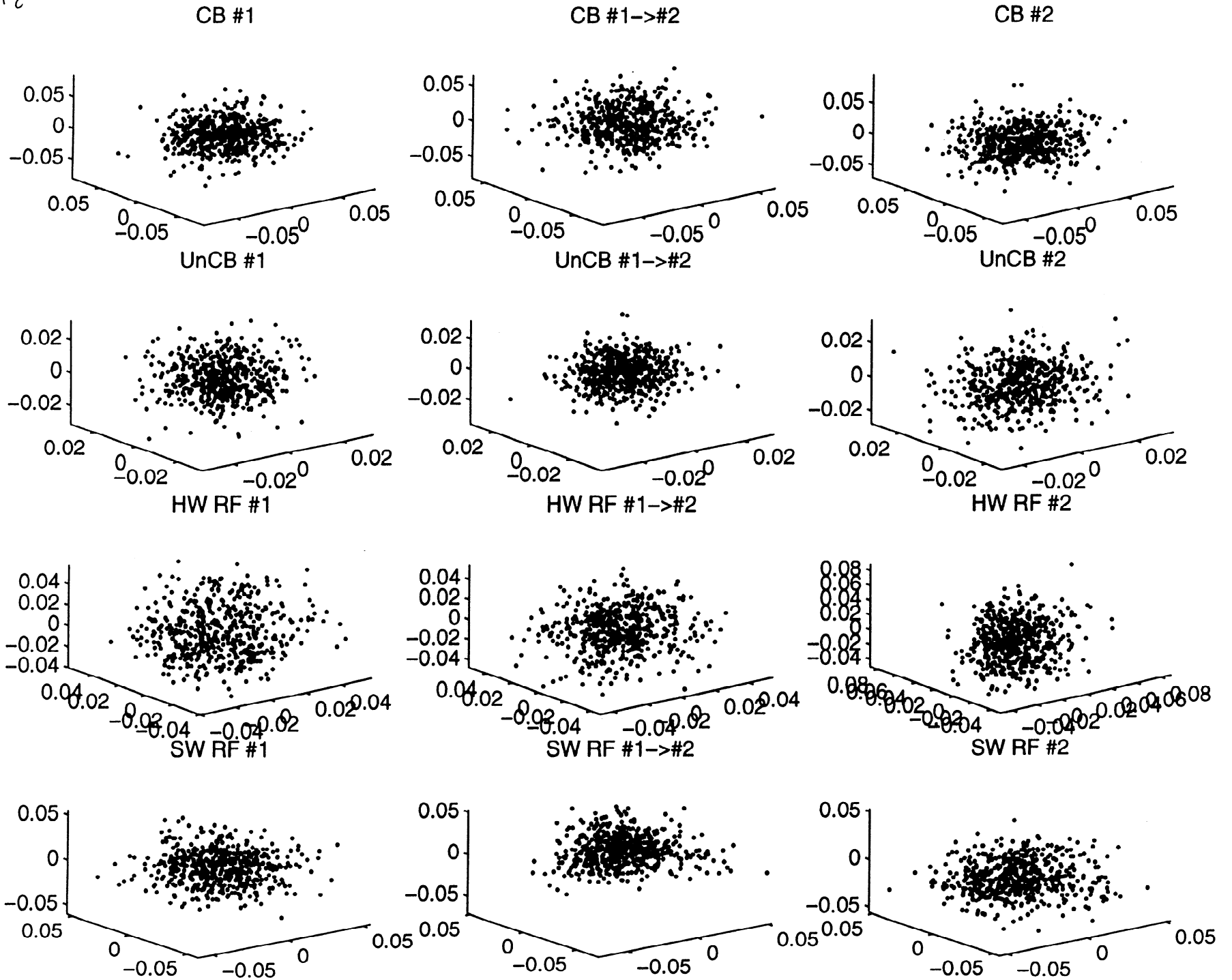
CB #1
CB #1->#2
CB #2
UnCB #1
UnCB #1->#2
UnCB #2
HW RF #1
HW RF #1->#2
HW RF #2
SW RF #1
SW RF #1->#2
SW RF #2

~150 Hz

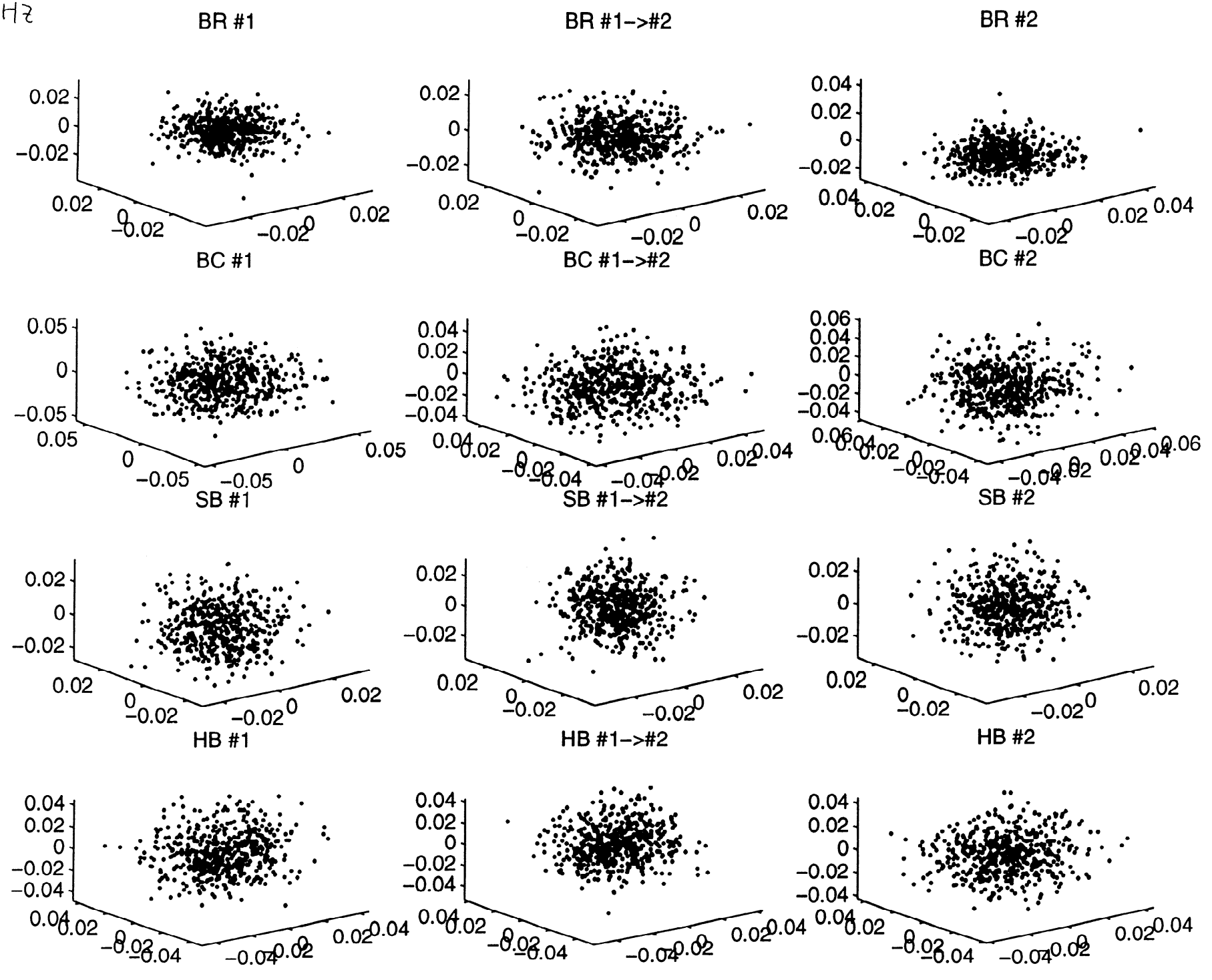

FUNDAMENTALS OF DRYING

STATUS REPORT

FOR

PROJECT F001

David I. Orloff
F. Bloom, C. Korach, H. Nanko, T. Patterson, P. Phelan,
M. Rislakki, I. Rudman, D. Woods

March 25, 1997

Institute of Paper Science and Technology
500 10th Street, N.W.
Atlanta, Georgia 30318

TABLE OF CONTENTS

Section	Subsection	Authors
I. Objective		
II. Goals		
III. Summary		
IV. Discussion		
A.	Methods of Controlling Sheet Delamination During Impulse Drying(F001).	D. Orloff
B.	Pilot HRP Impulse Drying Roll Press Verification of Post-Nip Pressurization Concepts(F001).	P. Phelan
C.	Microscopic Investigation of Sheet Delamination and Sheet Structure(F001).	H. Nanko
D.	Mathematical Model of Sheet Expansion and Steam Venting During Nip Opening(F001).	D. Woods, F. Bloom
E.	Sheet Expansion During Nip Opening Experiments(F001).	I. Rudman, M. Rislakki
F.	High-Speed Infrared Detection of Coated Roll Surface Defects(3595).	C. Korach, T. Patterson
G.	Status of Roll Coating Durability Testing(3595).	C. Korach, T. Patterson
H.	X4 Wet Pressing Results from January 1997 Start-up(3595).	P. Phelan
I.	Preliminary Analysis of the January 1997 Roll Cover Failure(3595).	D. Orloff, P. Phelan
J.	Thermal Barrier Coating Failure Mechanisms and Plans for Recoating the Press Roll(3595).	D. Orloff
V. References		
VI. Appendices		
AA.	The Mathematical Formulation of the Model for Pore Expansion During the Impulse Drying of Paper.	F. Bloom, D. Woods

TECHNICAL PROGRAM REVIEW

Project Title:	FUNDAMENTALS OF DRYING
Project Code:	DRYING
Project No.	F001
Division:	Engineering and Paper Materials
Project Staff:	D. Orloff, F. Bloom, A. Dowdell, C. Korach, H. Nanko, T. Patterson, P. Phelan, I. Rudman
Budget (FY'96-97):	$ 150,900
Government Funding:	Project 3595: FY'96-97, $ 700,000
Ph.D. Students:	1 (D. Woods)
Post-M.S. Students:	1 (M. Rislakki)

I. OBJECTIVE

To develop an understanding and a database for commercialization of advanced water removal systems based on high intensity drying principles. This new technology will reduce capital costs, increase machine productivity, reduce virgin fiber use, reduce the amount of energy used, and improve paper physical properties.

II. GOALS

F001: To expand the operating window of impulse drying technology to include a wider range of furnishes, basis weights, and grades.

3595: To commercialize the impulse drying process for board grades by 1998.

III. SUMMARY

Work on the dues funded (No. F001) project and on the separate DOE funded (No. 3595) project are on schedule. The dues funded work has focused on evaluating post-nip pressurization techniques in sheet-fed pilot impulse drying roll press experiments and in continuing to develop fundamental understanding that opens the operating window of the technology. The DOE funded work (in collaboration and with financial support from Beloit) has concentrated on roll surface durability and on initial startup of the pilot impulse dryer that is now installed on Beloits' No. 4 pilot paper machine. The key accomplishments of this period are summarized in this section.

Project No. F001:

- Patents: A US. patent, on high ambient pressure impulse drying, was issued on February 4, 1997 as US. Patent number 5,598,642. Beloit has funded the foreign filing of this patent. A US. patent on the use of a post-nip wrap and/or post-nip shoe to suppress sheet delamination has been filed as US. Patent application serial number 08/618,294, filed March 18, 1996. Beloit has agreed to fund foreign filing of this patent.

- Publications: Members of the Impulse drying team have published the following papers;
  1. "Lubrication and Heat Transfer in a Crown-Compensated Press Roll," Tribology Transactions 39(4):745-756 (1996).
  2. "The Effect of Thermal Mass and Peak Pressure on Impulse Drying Energy Transfer," TAPPI Journal 79(11):131-137 (1996).

3. "Analysis of Lubrication for Controlled-Crown Press Rolls: A Parametric Study," TAPPI Journal 79(9):164-171 (1996).

- A literature review was written to document the evolution of research on the impulse drying sheet delamination problem. See Section IV.A. for details.

- Statistically designed sheet-fed pilot impulse drying roll press experiments, conducted at Beloit, verified that a post-nip pressurization provided by a roll wrap or shoe will suppress sheet delamination. The experiment also examined variables that influence rewet. See Section IV.B. for details.

- Samples of delaminated specimens from the sheet-fed pilot impulse drying roll press experiments were microscopically investigated by Dr. Hiroki Nanko. The results are consistent with previous IPST-proposed delamination mechanisms and show some interesting fines distributions that may be the result of migration during impulse drying. Aee Section IV.C. for details.

- As part of Ph.D. thesis work, a theoretical model to predict sheet expansion and steam venting during the nip opening process was developed. The model, when coded, will allow the permeability of the ingoing web to be accounted for in post-nip pressurization optimization. The model may also prove useful in exploring potential sheet bulking techniques. See Section IV.D. for details.

- As part of a Post-M.S. project an apparatus and method for measuring sheet expansion during impulse drying was designed and is now being constructed. This apparatus will be used to provide data to verify the theoretical model. See Section IV.E. for details.

Project No. 3595:

- The use of a high speed infrared imaging system to detect roll coating defects on the roll durability test facility was documented. See Section IV.F. for details.

- The roll durability test facility was used to evaluate four different plasma sprayed roll coatings. After almost 5 million roll revolutions, no coating failures were observed. Future felt durability and roll doctoring experiments are being planned. See Section IV.G. for details.

- The induction heating system was installed on the Beloit No. 4 (X4) pilot paper machine, converting their Extended Nip^{R} press into an impulse dryer. The paper machine, with the Extended Nip^{R} press operating as a single-felted wet press, was used in January of 1997 to produce 42-pound linerboard at a speed of 1250 fpm from repulped commercial linerboard. Press dryness and sheet physical properties were determined. See Section IV.H. for details.

- The induction heater on the X4 paper machine was started up and impulse drying runnability experiments were begun during in January of 1997. Impulse

drying experiments were delayed due to an unanticipated roll coating failure. A preliminary analysis of the coating failure suggests that the most likely causes may be easily rectified. See Section IV.I. for details.

- To assure that all possible causes of the coating failure are considered, a literature review was conducted on recent advances in the design and the mechanisms of failure of thermal spray coatings. Plans for recoating the X4 roll are also discussed. See Section IV.J. for details.

IV. DISCUSSION

A. Methods Of Controlling Sheet Delamination During Impulse Drying

Our understanding of the mechanisms responsible for sheet delamination during impulse drying has grown over the past eight years. With what is known today one can look back and see a fairly clear picture of the evolution of the ideas of the researchers who have contributed to this understanding.

In the watershed paper by Crouse, Woo and Sprague [A1], impulse drying of linerboard was shown to have the potential of disrupting and delaminating (breaking of fiber bonds) the linerboard sheet. They found that delamination could only be avoided when the sheet-fed pilot press was operated at temperatures below 150°C. Conditions that only resulted in sheet strength and press dryness that could as easily be achieved by conventional pressing at elevated ingoing sheet temperatures. Hence, it was concluded that delamination must be fully understood and be alleviated for impulse drying to become a commercial technology that is applicable to the manufacture of board grades.

In response to the work of Crouse, Woo and Sprague, research was undertaken at a number of corporate and academic research centers to overcome the sheet delamination problem. Early work focused on identifying significant variables and developing causal hypotheses. In work reported by Burkhead, Burns, Lindsay, and Orloff [A2], delamination was found to be affected by felt initial moisture content. The use of bone-dry felt resulted in poorer dewatering and was more likely to cause delamination than were slightly moist felts. It was speculated that the effect of initial felt moisture might be due to observed differences in the dynamic compression behavior of the felt or to changes

in its water absorption properties. Although felt moisture played a role in delamination, press surface temperature, peak mechanical pressure, and nip residence time were also identified as important process variables.

Back [A3] reported that the risk of delaminating the wet sheet when it exits the nip had been underestimated by previous investigators. He reasoned that this had occurred, on the one hand, through the use of residence periods in the press nip which cannot yet be realized at modern machine speeds, and, on the other hand, as a result of the relatively long periods required to relieve pressure in pilot tests. In a paper on hot pressing, Back [A4] examined the limitations of impulse drying. He recommended further research focused on improving z-direction strength and suggested that the economics of impulse drying could be improved by the use of equipment permitting an extended residence time in the nip and a slow reduction in pressure. In a later review article, Back [A5] set forth what he considered as requirements for impulse drying equipment. These included using the longest possible dwell time to achieve maximum outgoing solids and z-directional wet strength; a low pressure deloading rate to reduce drag forces, which cause delamination; and a low outgoing maximum temperature in the wet web, especially where most moist. Hence, Back saw the solution to delamination as being associated with the temporal change in pressure experienced by the sheet within the nip and minimization of heat transfer to the sheet during nip opening.

From this starting point, research on preventing delamination took two separate paths. The first path consisted of modifications to the press nip such as reducing the thermal properties of the press roll, drilling the press roll and changing the conditions of the nip, for example impulse, pressure profile, and sheet construction. The second path, which has been much more sparsely reported in the literature, approaches the problem through

modifications to the conditions the sheet experiences after it leaves the nip. Examples that will be discussed include the use of steam chambers, gas chambers, roll wraps, and secondary nips.

1.) Modifications Within The Nip:

To prevent delamination, Stenstrom [A6, A7] proposed the use of a press surface that would make it possible to evacuate vapor from the hot surface of the sheet through a number of radial drilled holes. He reasoned that, while in the nip, the hydraulic pressure prevents vaporization during most of the contact time. However, the sudden pressure decrease, when leaving the nip, causes vaporization and rapid flow of water vapor out of the sheet. If the z-direction wet strength of the web in this moment is not high enough to withstand the internal vapor pressure the web will break and delaminate in two or more layers. He concluded that in order to prevent high vapor pressures, vapor flow and vaporization should also be made possible during contact in the nip. As resistance to vapor flow is lower in the dried, as compared to the wet part of the sheet, vapor flow can be achieved by venting the hot surface in contact with the sheet. Using similar reasoning, Pulkowski [A8] patented a porous press roll surface for use in impulse drying.

Approaching the problem from the heat transfer standpoint, Kloth, Orloff, and Rudemiller [A9], patented a low thermal diffusivity press roll surface. Subsequent patents issued to Lenling and Orloff [A10] and Orloff [A11] further developed the use of insulating press roll surfaces for the purpose of reducing the likelihood of sheet delamination.

In a paper by Orloff [A12], the development, design concept, and performance properties of a prototype insulating roll-coating material that could extend the operating temperature of impulse drying were described. Impulse drying simulations, at short dwell times and ingoing sheet temperatures that were consistent with current practice, were reported. It was found that reducing the effective "thermal mass" of the heated press surface and increasing peak operating pressure allowed operating temperatures to be increased. Under these conditions, impulse drying was used to achieve higher outgoing solids, higher final sheet densities, and higher specific elastic modulus without sheet delamination.

Using the insulated press roll surface technology, Orloff and Sobczynski [A13] report additional process modifications that facilitate the drying of heavyweight grades while avoiding sheet delamination. The research examined the influence of specific surface, assessed the relationship between specific surface and energy transfer, and presented an estimate of anticipated energy savings. Two virgin-fiber Kraft furnishes of southern pine *(pinus)* were impulse dried on a pilot roll press featuring a plasma-sprayed ceramic-coated roll. The out-of-plane permeability of the sheets were measured as a function of sheet porosity to determine their hydrodynamic specific surface. The results showed that specific surface limited the maximum impulse-drying temperature. Data from laboratory simulations suggested that the use of the ceramic coatings avoided sheet delamination by decoupling heat transfer from overload pressure and the physical state of the sheet.

Lindsay and Orloff [A14] investigated the influence of yield, refining, and ingoing solids on the impulse drying performance of the ceramic-coated press roll. Furnishes of southern pine *(Pinus)* were used in pilot-scale impulse drying experiments that covered a range of refining levels, ingoing solids, and kappa numbers. These experiments produced sheets with a range of hydrodynamic specific surfaces. The results confirmed earlier laboratory

findings that indicated that the roll temperature at which sheet delamination initially occurs was a function of the specific surface of the ingoing web, which was, in turn, a function of cooking, refining, and pressing variables.

To extend the work to more typical linerboard sheet structures, simulations of the impulse drying of recycled multi-ply linerboard were carried out by Orloff [A15]. The experiments were conducted to determine the influence of several factors on impulse-drying performance. These factors included virgin pulpwood species, OCC content, and composition and freeness of the individual plies in two-ply linerboard. Virgin pulp species was found to be important because southern pine *(Pinus)* was found to be superior to Douglas-fir *(Pseudotsuga menziesii)*. Single-ply blends composed of 50% or less OCC had better strength, and those with 75% or less OCC content had better dryness. For two-ply linerboards constructed of blended bottom sheets and virgin-fiber top sheets, the composition of the sheet contacting the heated press surface controlled the critical temperature of impulse drying (i.e., the highest temperature that could be used to impulse-dry the sheet without causing delamination).

In another simulation, Boerner and Orloff [A16] explored the effect of basis weight and refining on sheet permeability and critical impulse-drying temperature. Linerboard grades with basis weights of up to 400 g/m^2 and freeness of 600 ml CSF could be impulse-dried without delamination when a heated press surface with a low "thermal-mass" coating was used. Permeability measurements showed that the critical impulse-drying temperature could be predicted from the hydrodynamic specific surface of the sheet. The reason that Darcian permeability was greater in lightweight sheets may be due to the presence of nonuniformities (macropores) that extend through the sheet thickness and allow fluids to pass through. In contrast, in sheets with a higher basis weight, the macropores did not

extend through the sheet, so that porosity was controlled by the hydrodynamic specific surface of the fines and fibers in the sheet. Comparisons of outgoing sheet dryness and compression strength with sheets pressed in a double-felted Extended Nip^{R} press showed that impulse drying was better.

Orloff and Phelan [A17] studied the influence of pressure profile on impulse drying. In these simulations, pressure pulse shape was varied while heat flux, critical temperature, and the development of paper physical properties were measured. It was found that the pressure peak should be maximized and should be shifted to the dry end of the process to optimize water removal and sheet strength. Hence, besides providing the long residence time beneficial to impulse drying, a shoe press also provides the optimum pressure pulse shape.

To demonstrate the usefulness of these process modifications, Crouse, Orloff, and Phelan [A18], conducted experiments in which linerboard was impulse dried on a sheet-fed pilot shoe press which was fitted with a press roll having a low "thermal mass" coating. For a wide range of one- and two-ply linerboard sheet structures, impulse-drying and double-felted pressing were compared. Performance indicators included STFI compression strength, press dryness, and flexographic printability. The results confirmed simulations [A15] that showed impulse drying to be superior to double-felted pressing.

To provide insight into the reasons why low "thermal mass" press surfaces are useful, Kerschner, Orloff, and Phelan [A19] performed experiments to test the hypothesis that excessive energy transfer to the sheet, by itself, accounts for sheet delamination. Steel- and ceramic-coated platens were used in simulations that investigated the effect of thermal mass and peak pressure on energy transfer during impulse drying. Shoe-press pressure

profiles at three levels of peak pressure, viz., 6.5, 8.5, and 9.5 MPa; two levels of ingoing solids, viz., 36 and 47%; and two furnishes with hydrodynamic specific surfaces of 1.4 and 10.5 m^2/g were simulated. The press surfaces were equipped with vacuum-deposited surface thermocouples. Temperature profiles measured during the impulse-drying event were used to calculate heat flux to the sheets. The results show that, for a given sheet structure, there was no unique critical energy that was required to initiate sheet delamination. For the ceramic surface, the energy transferred to the sheet was dependent on temperature but not on pressure. In contrast, the energy transfer from the steel surface was dependent on both temperature and pressure. Compared to the ceramic case, there was a substantial amount of scatter in the steel energy data, indicating that local variations in paper properties (e.g., moisture content) and nip pressure may influence total energy transfer for the steel surface. These results partly explain why low "thermal mass" press surfaces are useful and also pointed out that further improvements to impulse drying technology would need to come from post-nip modifications.

2.) Modifications After the Nip:

In an early paper by Miller [A20], "multipulse" drying units were compared with impulse dryers. He described the "multipulse" machine as consisting of a heated, free-floating drum between two movable nip rolls that tension a belt around the drum and the rolls. He reports that multiple nips are more effective than a single nip, and that they lessen web shrinkage, enhance heat transfer, and inhibit sheet delamination. He explains the delamination inhibition of the "multipulse" units by noting the differences between the impulse cycle and the "multipulse" cycle. The "multipulse" nips are shorter, putting less energy into the sheet at each nip. As a result, less energy, internal to the sheet, vents as vapor. In the case of the first "multipulse" nip and the interior nips, the sheet is

constrained on the exit of the nip so the internal vapor expands only to the intermediate pressure level and is constrained while doing so, typically at 170 to 240 kPa (10 to 20 psig). The last nip is therefore the critical one, and it has two benefits over the impulse nip. It inputs less energy to the sheet and it is operated at a higher ingoing solids. Hence, Miller viewed the solution to the delamination problem as requiring multiple short residence time roll nips with the sheet being constrained between these nips. A few years later, Crouse [A21] patented the concept of using two successive Extended Nip^{R} presses with two separate heated press rolls configured such that the web is held in contact with the press rolls both before and after entering into the press nips by felt.

Babinsky and Mumford [A22] assumed that delamination occurred during or immediately after the sheet exits the nip. They hypothesized that they could eliminate delamination by reducing the rate of vaporization from the sheet as it leaves the press nip. To reduce the rate of vaporization, they proposed exposing the exiting sheet to a steam environment. In their patent they use a steaming chamber positioned just downstream from the nip. The steam chamber was sealed against the press rolls and required a downstream exit seal through which the web can pass. Steam was injected into the chamber to keep the chamber pressure at about 200 kPa (2 atmospheres). Means were also provided to preheat the web upstream from the nip. These arrangements permitted the reduction of the temperature of the heated roll and reduced the magnitude of the pressure changes to which the web was subjected, thus reducing the chance of delamination.

Recognizing that further improvement to impulse drying technology would need to come from modifications after the nip, Orloff [A23] proposed modifications to the impulse drying simulator to allow process modifications during and immediately following nip

opening. Orloff hypothesized that delamination occurs when subcooled water, at high pressure and temperature in the sheet, flashes to vapor when the nip opens to ambient pressure. To test the significance of the pressure that the sheet is exposed to upon nip opening, Orloff designed the simulator so that at nip opening the sheet would be exposed to pressures well above one atmosphere. If the hypothesis was correct, then sheet delamination would be eliminated.

Using the modified simulator, Orloff [A24] patented a method of impulse drying at elevated ambient nip-opening pressures. The method exposes the web to ambient pressures above atmospheric and provides for increasing cooling rates when the press load is released. The patent teaches that sheet delamination can be prevented by opening the nip to a sufficiently high "critical" ambient gas pressure. The gas used can be any gas as long as it is at a temperature below 100°C. Based on simulations, "critical" pressures were found to increase with increased temperature of the heated press surface, increased basis weight, increased ingoing sheet moisture content, and increased specific surface of the sheet.

In recent research we have used thermocouples imbedded in sheets to record internal temperature profiles during nip opening. Using thermodynamic reasoning we showed under what conditions those temperatures could be used to infer local pressures. In such a manner we were able to show that by opening the nip to higher ambient gas pressures we are actually reducing the pressure difference between the inside and outside of the sheet during that critical time. One can then say that we are holding the sheet together while the internal pressure decays. While one can hold the sheet together with an external gas pressure, a simpler way would be to provide an external mechanical force. Based on this reasoning, we filed a US patent [A25] to cover the application of elevated pressures by

such techniques as post-nip roll wraps and post-nip shoes. To demonstrate that this concept is not just a laboratory curiosity, we have conducted sheet-fed impulse drying experiments at Beloit's pilot HRP impulse drying roll press. The preliminary results of these experiments is given in Section IV.B. of this report.

B. Pilot HRP Impulse Drying Roll Press Verification of Post-Nip Pressurization Concepts

1.) Introduction:

Experiments were continued on the Beloit Hot Roll Press (HRP) in October 1996. Previous results were reported at the Fall 1996 Papermaking PAC meeting. This experiment had the following specific objectives:

- Test the concept of a duplex felt to suppress delamination and minimize rewet.
- Test the use of an air-knife to help suppress delamination.
- Test the use of a Teflon block to simulate a second low-pressure shoe.

The main objective was to test a duplex felt (transfer belt) for rewet suppression while being able to go to a higher temperature with different post-nip treatments. The cold felt was a standard felt (N240) and was separated from the transfer belt immediately after the nip. The transfer belt was made with six MD sections, only two of which were tested, and was used to apply a post-nip wrap.

An air-knife, applied between the sheet and the transfer belt, was tested for additional delamination suppression. For some selected cases, the air knife was applied between the sheet and the hot roll. Also, a fitted Teflon block was used to apply additional pressure to the transfer belt coming out of the nip, simulating a second low-pressure shoe for applying a ramp to the tail of the pressure profile.

2.) Procedures:

A quarter factorial experiment was designed with the following parameters:

a.) Constants

- Beloit "E" roll cover,
- Steam preheating of the sheet to ~93°C (200°F), and
- 40 ms haversine pressure pulse.

b.) Variables

Furnish (3)	OCC at 500 ml CSF OCC at 400 ml CSF Virgin Pine at 350 ml CSF
Pressure (2)	3.65 and 5.17 MPa (530 and 750 psi)
Ingoing Solids (2)	35 and 45%
Post-nip Treatments (4)	None, no wrap with air knife, 3.3-inch wrap, and wrap with Teflon block
Transfer Belt Types(2)	2 out of 6 possible
Temperatures (4)	24, 163, 204, and 246°C (76, 325, 400, and 475°F)

The test sheets were cut from Formette Dynamique sheets that were pressed to the required solids level using a combination of platen pressings and roll pressings. After cutting the 8-inch by 11-inch sheets, the samples were randomized and bagged for shipment to Beloit.

Before starting the factorial experiment, the six transfer belt sections were evaluated with the roll temperature at 177°C (350°F). Samples of each furnish were pressed using each belt section. Based on the water removal and visual appearance of the samples, the two best sections (coded 1 and 4) were chosen for the remainder of the experiment. After removing the post-nip wrap, the temperature was varied to determine the critical temperature. Unfortunately, sheet sticking at low temperatures made the determination difficult. Impulse drying temperatures of 163, 204, and 246°C were used to cover the possible range of critical temperatures.

The factorial experiment was designed to maximize randomness within certain constraints of roll temperature and post-nip treatments. Enough replicates of different run conditions were performed to check day-to-day variations. For each run condition, five repeats were used.

In the middle of the experiment, an interlock failure caused the roll to develop an extreme hot spot. This hot spot overheated the transfer belt, destroying the belt. A new belt was made and mounted on the HRP and the experiment continued. Additional replicates were added to the experiment to test the difference between the transfer belts.

After finish drying, the samples were tested at IPST for delamination using the bench-scale ZD ultrasound tester. Additional tests performed were: in-plane ultrasound, ZD ultrasound using the on-line tester with contact wheels, Sheffield Smoothness, Caliper (density), Gurley porosity, MD and CD STFI, and MD and CD Ring Crush.

For the statistical analysis, the compiled data was sent to a consultant (N. Esposito). The analysis is ongoing at the time of this writing. Final results will be published in a member report later this spring.

3.) Preliminary Results:

Using the averages of the five repeats for each run condition, delamination was determined using up to four test criteria: visual codes, specific elastic modulus (SEM), coefficient of variation of the specific elastic modulus (CVSEM), and microscopic examination of wet sheets (see Section IV.C. of this report). A consensus of the four criteria was reached using the following rules:

- If all criteria indicate no delamination, then the run was marked "undelaminated".
- If the visual code and any one other criteria indicated delamination, then the run was marked "delaminated".
- If either the visual code or the microscopic examination indicated delamination, then the run was marked "provisionally delaminated".

Once it was determined whether a run was delaminated or not, the run temperature was then an upper or lower limit of the "critical temperature". The results are tabulated below as number counts for each condition. The numbers in parenthesis are the provisionally delaminated cases.

Table B1. Pine Furnish, Delamination Limit Counts.

Temperature	None	Air Knife	Wrap	Block
Lower				
>163				2
>204				
>246				
Upper				
<163	0 (2)	2 (2)		
<204	2	2	0 (1)	1
<246	2	2	1 (1)	2
Brackets	Tc<163	Tc<163	Tc<204	163<Tc<204

Table B2. OCC400 Furnish, Delamination Limit Counts.

Temperature	None	Air Knife	Wrap	Block
Lower				
>163	1	2	2	2
>204			2	
>246			1	
Upper				
<163	(1)			
<204	1 (1)	2		1
<246	2	2	1	2
Brackets	Tc<204	163<Tc<204	204<Tc	163<Tc<204

Table B3. OCC500 Furnish, Delamination Limit Counts.

Temperature	None	Air Knife	Wrap	Block
Lower				
>163				1
>204			2	1
>246				
Upper				
<163	1 (1)	1 (2)	(1)*	(1)*
<204	2 (1)	2 (1)		
<246	2 (1)	3	1	
Brackets	Tc<163	Tc<163	204<Tc<246**	400<Tc**

Notes: * These are anomalous runs.

** Excluding the anomalous runs.

For the above tables, the process variables of ingoing solids, peak pressure, and transfer belt were lumped together. The anomalous runs noted above are not used in the following analysis. At the time of writing, we do not know why these runs delaminated, but we are continuing to examine the data. The above results indicate ranges for the critical temperatures, but cannot be refine further without additional data. To gain further insight, we utilize a statistical analysis.

Initial analysis of the data showed two things. First, the furnish overwhelmed all other process variables, accounting for from 65 to 70% of the total variation for the analyzed response variables. This was expected because the furnishes were selected to cover a moderately large range. The second result was that there was no significant difference between the post-nip conditions "none" and "air knife", and between the conditions "wrap" and "block". Therefore, for further analysis, the post-nip conditions were grouped into "no wrap" and "wrap", and each furnish was evaluated separately. In

addition, ingoing solids was added as a covariate (the analysis was statistically adjusted to remove the influence of ingoing solids).

Summaries of the results, utilizing the above changes, are presented in Tables B4 through B8. The numbers indicate the approximate percentage of total variability of each response variable associated with each process variable as determined from the sum of squares of the ANOVAS for the run averages. The arrows indicate the direction of change. If a cell is blank, then the process variable was not statistically significant. The tables only summarize the main effects, higher order interactions are not shown.

Table B4. Preliminary Results For OCC400 Furnish. Significant Main Effects Only.

RESPONSE VARS.	Postnip2*	Roll Temp	Furnish	Ingoing Solids	Peak Press	Trans Belt
Delam	↓42	↑27	EXCLUDED			
MRC		↑47	FROM	22	↑8	↑4
Cdstfi	↑8	↓26	ANALYSIS			
Cdring		↓48			↑4	↑4

*POSTNIP AT 1 = NO WRAP CONDITION, POSTNIP AT 2 = WRAP CONDITION

Table B5. Preliminary Results For OCC500 Furnish. Significant Main Effects Only.

RESPONSE VARS.	Postnip2*	Roll Temp	Furnish	Ingoing Solids	Peak Press	Trans Belt
Delam	↓42	**11	EXCLUDED	6	↓2	↓8
MRC	↓3	↑37	FROM	24	↑3	↑3
Cdstfi		↓34	ANALYSIS			
Cdring	↑2	↓44		1	↑1	↑3

*POSTNIP AT 1 = NO WRAP CONDITION, POSTNIP AT 2 = WRAP CONDITION

**Quadradic dependence.

Table B6. Preliminary Results For Pine350 Furnish. Significant Main Effects Only.

RESPONSE VARS.	Postnip2*	Roll Temp	Furnish	Ingoing Solids	Peak Press	Trans Belt
Delam	↓59	↑23	EXCLUDED			
MRC		↑26	FROM	40	↑10	↑10
Cdstfi		↓52	ANALYSIS			
Cdring		↓47				

*POSTNIP AT 1 = NO WRAP CONDITION, POSTNIP AT 2 = WRAP CONDITION

Regression analyses were done for the Delamination Code (Delam) response variable. For these analyses, the data at 24°C (76°F) and the two anomalous runs were not used. The preliminary coefficients are summarized below in Table B7 and were used to infer the critical temperatures as shown in Table B8.

Table B7. Preliminary Regression Results On Delam For Each Furnish.

Independent Variable	Coefficients		
	Pine350	OCC400	OCC500
Constant	0.323573	0.014059	8.19366
Post-Nip2	-0.700085	-0.535737	-0.678694
Roll Temp	0.003493	0.003446	-0.033554
(Roll Temp)^2			0.000042
Trans Belt			-0.060634

Table B8. Preliminary Estimates Of Critical Temperature From Regressions.

	Pine350	OCC400	OCC500
No Wrap			
Tc (°C)	107	132	Still
Min	73	52	Being
Max	140	212	Analyzed
Wrap			
Tc (°C)	218	218	Still
Min	151	138	Being
Max	285	298	Analyzed

We are still evaluating the above statistical analyses and consider the results to be preliminary. For each of the other response variables (water removal and strength properties) we will do a regression analysis and using the critical temperatures noted above, we can compare relative differences between the post-nip treatments.

4.) Conclusions:

From the results reported, the following conclusions can be stated:

- Adding a post-nip roll wrap increases the critical temperature for the furnishes tested. With proper rewet control, water removal should also increase based on the ANOVA result that increased temperature increases water removal while wrap has little or no effect (further analysis to come).
- The air knife has no statistically significant effect.

- The block has no statistically significant difference from the plain wrap. This may be due to the shape of the pressure profile that was obtained by using the block.
- The effect of using a duplex felt system cannot be determined until we compare the results from this experiment to previously reported data. However, these data do show that proper rewet control is possible with a post-nip wrap.

5.) Acknowledgments:

An unmeasurable amount of thanks must be given to Jere Crouse of Beloit Corporation and all of the people who helped run the experiment. Without them, this work would not have been possible.

The personnel of the IPST paper testing laboratory contributed a large amount of their time and effort in completing the testing to meet the provided deadline. The authors gratefully thank them.

Last but far from least, Dr. Nicholas Esposito provided invaluable help in designing the experiment, performing the statistical analyses, and interpreting the results. Thank you.

C. Microscopic Investigation of Sheet Delamination and Sheet Structure

1.) Purpose:

The purpose of this work was to add to the understanding of the mechanisms responsible for impulse drying induced sheet delamination through microscopic observation of delaminated sheet structure. For this purpose, samples were obtained during the October 1996 Beloit Hot Roll Press (HRP) experiment that was presented in Section IV. B. of this report.

2.) Methods:

a. Observation of delamination in the moist sheet exiting the impulse dryer.

In order to maintain the structure of the moist web exiting the impulse dryer, the following embedding method was developed and utilized:

- Each impulse dried sheet was sandwiched between two blotters, and the edges of the blotters were stapled together to protect the moist sheet from accidental deformation.

- These samples were soaked in 100% ethanol and were kept in the plastic bags to prevent ethanol evaporation. Replacement of the water in the moist web by the ethanol gradually progressed within the plastic bag.

- After the dehydration of the sample with 100% ethanol, the ethanol is replaced with propylene oxide, and finally the propylene oxide is replaced with Epoxy resin.

- After substitution with the Epoxy resin, the samples were removed from between the blotters and were sandwiched between polyethylene films.

- These were cured in the oven at 65°C for one week.

- Three-micron-thick cross sections were cut from the embedded samples and permanent slides were prepared.

- The sections were observed under the phase contrast microscope.

b. Observation of the internal surface of delamination by Scanning Electron Microscopy

Considerably delaminated dry samples were selected and 5-mm by 7-mm samples were cut out with a laser blade. The delaminated surface was exposed as if opening a book and was mounted on a stub. This made it possible to compare the hot-side and cold-side of the delaminated surface. After coating, the samples were observed in the Scanning Electron Microscope.

3.) Results

a. Cross-sectional view of delamination.

In the moist web that entered the impulse dryer, relatively large pores, which extend more or less parallel to the web surface, existed in various Z-direction positions (Figure C1). Some of these pores remained in the web even after impulse drying. The moist web was relatively loose on the heated-side of the sheet as compared to the cold- or wire-side of the sheet.

Delamination occurred close to the hot surface. The space caused by delamination extended more or less parallel to the web surface (Figures C2, C3, and C4). In the extremely delaminated webs, delamination often occurred in two Z-direction locations and overlapped or merged into one delamination (Figure C2).

The fibers that had contacted the hot roll surface were collapsed (Figures C2, C3, and C4). The hot surface of the web was flat and the layer attached to it was more dense than other parts of the web (Figure C2 and C3).

The density of the moist web increased when the pressure at the nip was increased (compare Figure C2 and Figure C3).

Secondary fines were visible in sections; however, their distribution was rather difficult to determine by light microscope.

b. Internal surface of delamination.

On the internal surface of the delamination, the fiber network was mostly covered by the secondary fines (Figure C5). The areas of exposed fibers were sparsely distributed and were relatively small.

4.) Possible mechanisms of delamination

The microscopic observations suggest the following mechanism of web delamination, which is shown schematically in Figure C6.

- Rapid elevation of temperature occurs in the moist web close to the hot roll surface.

- The fiber network (of these Formette Dynamique produced handsheets), impregnated by fines, forms panel-like layers in the web. Such a network, enforced by fines, considerably reduces steam permeability. It is also highly resistant to forces required to break the structure. When steam expands due to the decrease of nip pressure, the panel-like layers resist the Z-directional expansion of the steam.

- The moist web is relatively susceptible to Z directional tensile forces because the fibers are oriented more or less in the XY plane. The steam expands forcing the space between panel-like planes to open. These planes guide the steam outward from the roll nip toward the nip exit and atmospheric pressure.

- The steam escapes mostly from the hot surface of the web when the web has passed through the roll nip.

5.) Further study

- Determination of fines distribution in the moist web.
- Possibility of fine migration during impulse drying.
- Observation of the sheet structure after drying.

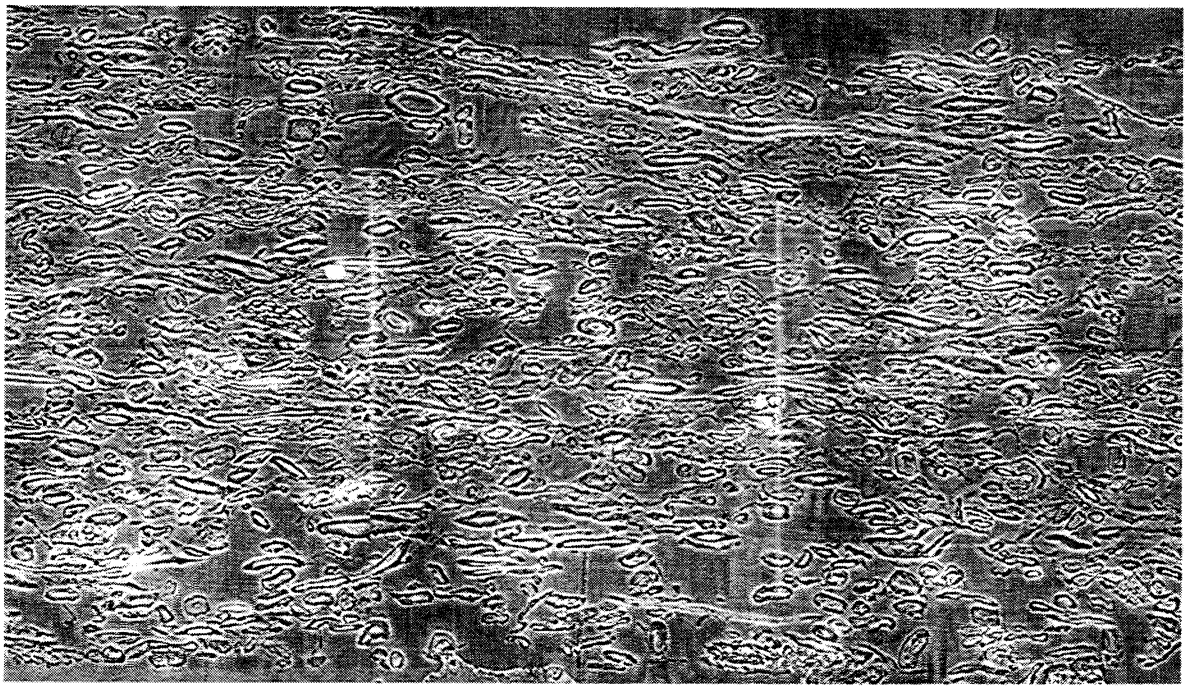

Figure C1. Cross Section of the Moist Web of OCC 500 Before Impulse Drying.

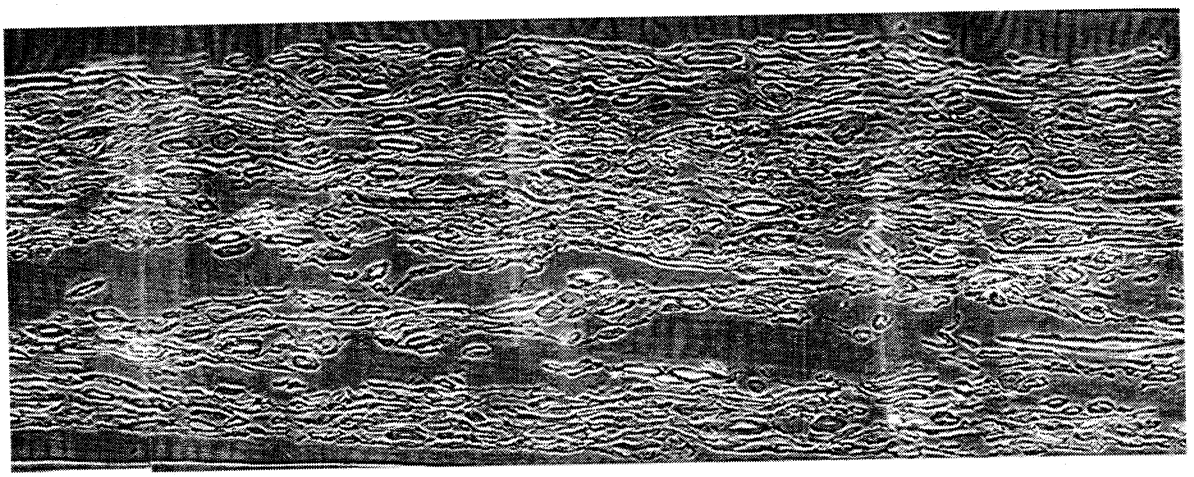

Figure C2. Cross Section of an Impulse-Dried Sheet Showing Delamination.

Post-Nip Treatment: Wrap, Roll Temp.: 246°C, Press.: 5.17 MPa, Furnish: OCC500

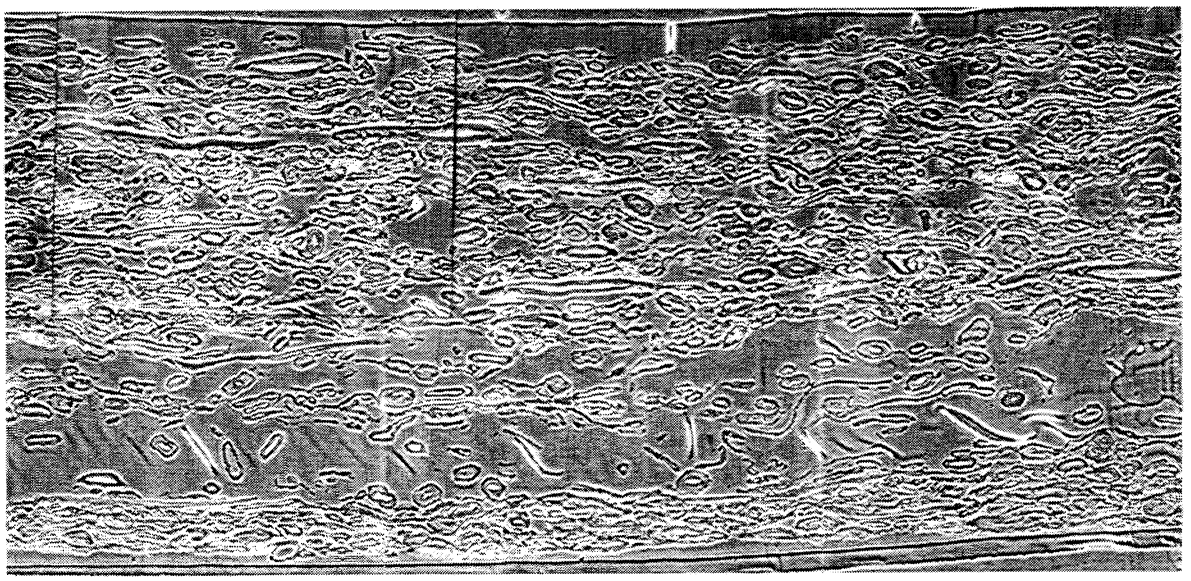

Figure C3. Cross Section of an Impulse-Dried Sheet Showing Delamination.

Post-Nip Treatment: None, Roll Temp.: 246°C, Press.: 3.65 MPa, Furnish: OCC500

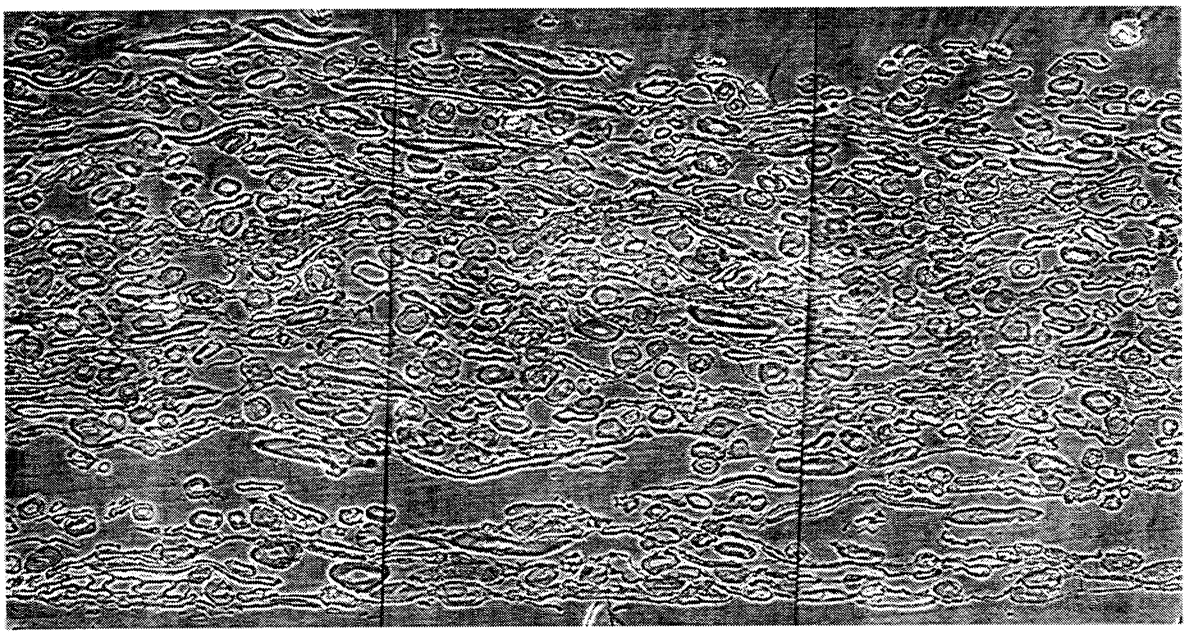

Figure C4. Cross Section of an Impulse Dried Sheet Showing Delamination.

Post-Nip Treatment: None, Roll Temp.: 246°C, Press.: 3.65 MPa, Furnish: Pine350

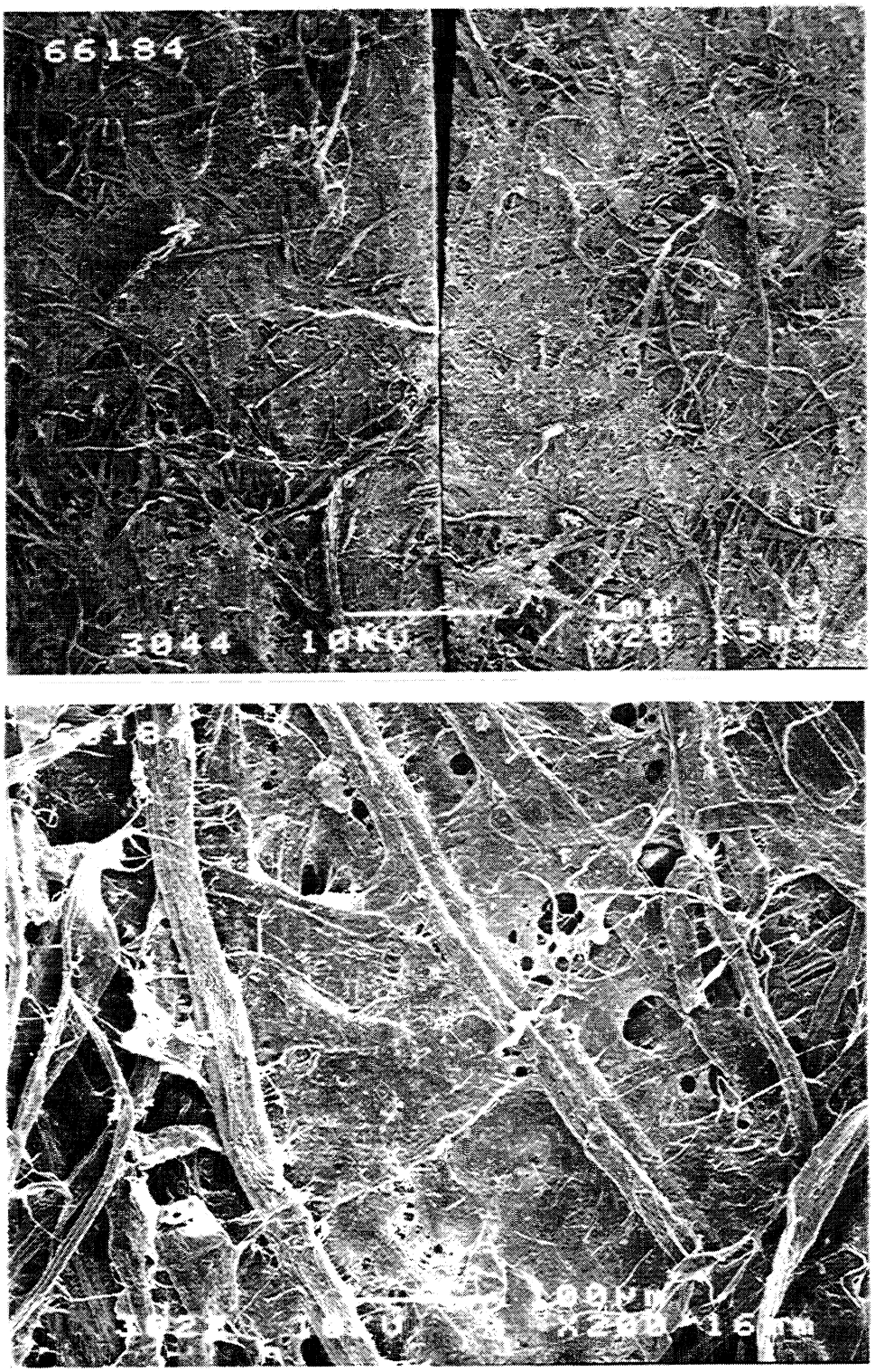

Figure C5. Internal Surface of Delamination of an Impulse-Dried Sheet.

Post-Nip Treatment: None, Roll Temp.: 246°C, Press: 3.65 MPa, Furnish: OCC500

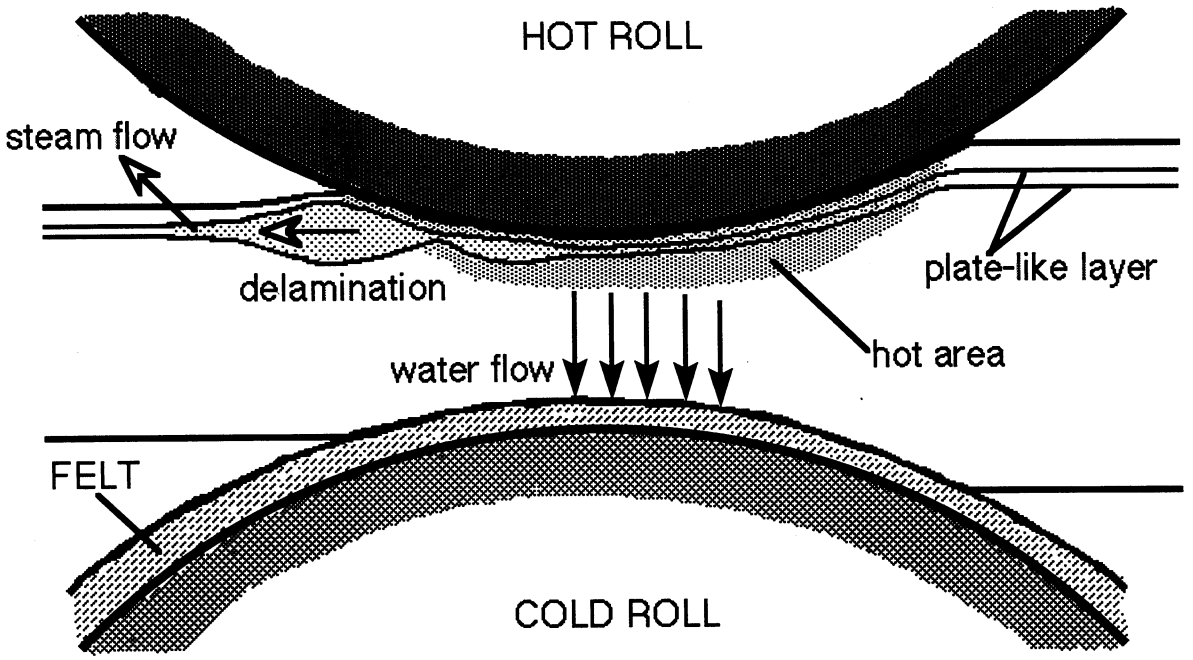

Figure C6. Schematic illustration of the Mechanism of Delamination by Impulse Drying.

D. Mathematical Model Of Sheet Expansion and Steam Venting During Nip Opening

1.) Introduction:

To date, much of the work done to control delamination during the impulse drying of paper has been in modifying the physical characteristics of the sheet to make it less liable to delaminate [D1], [D2], or in modifying the surface properties of the press roll to control how heat energy is transferred to the sheet [D3], [D4], [D5]. Work to control the cause of delamination, the flash vaporization of water within the paper, has recently been undertaken [D6]. To control this flash vaporization, it is necessary to understand what is happening inside the sheet as it exits the nip. To this end, a mathematical model of what occurs in individual paper pores during the critical time period was developed. This model takes advantage of well-known physical laws and thermodynamic properties to make predictions about the shape and size of the paper pores through time. It is hoped that this model will give some insight into the conditions that lead to a pressure buildup within the sheet that eventually ruptures the fiber bonds of the paper.

2.) Summary of the Model:

In Figure D1, we depict a cross section of a sheet of paper as it exits the nip. For the idealized situation shown, it is assumed that the pores may be represented by cylinders of constant radii R_i and variable heights $H_i(t)$, $i = 1,\ldots,n$, $t \geq 0$, where n is the number of pores. The pores are connected, one to the other, by capillaries which allow for the venting of water vapor. These capillaries are assumed to have constant lengths l_i and radii r_i, $i = 1,\ldots,n$, with the radii r_i chosen so that $A_i = \pi r_i^2$ is the net area through

which vapor may vent at the top of the i^{th} pore. As shown in Figure D1, the first capillary vents out through the top of the sheet, which is maintained at pressure $p_0(t)$ for $t \geq 0$, and there is no venting of vapor into the n^{th} pore, which may be taken to lie either at the bottom of the sheet or at the bottom of that layer of the sheet in which

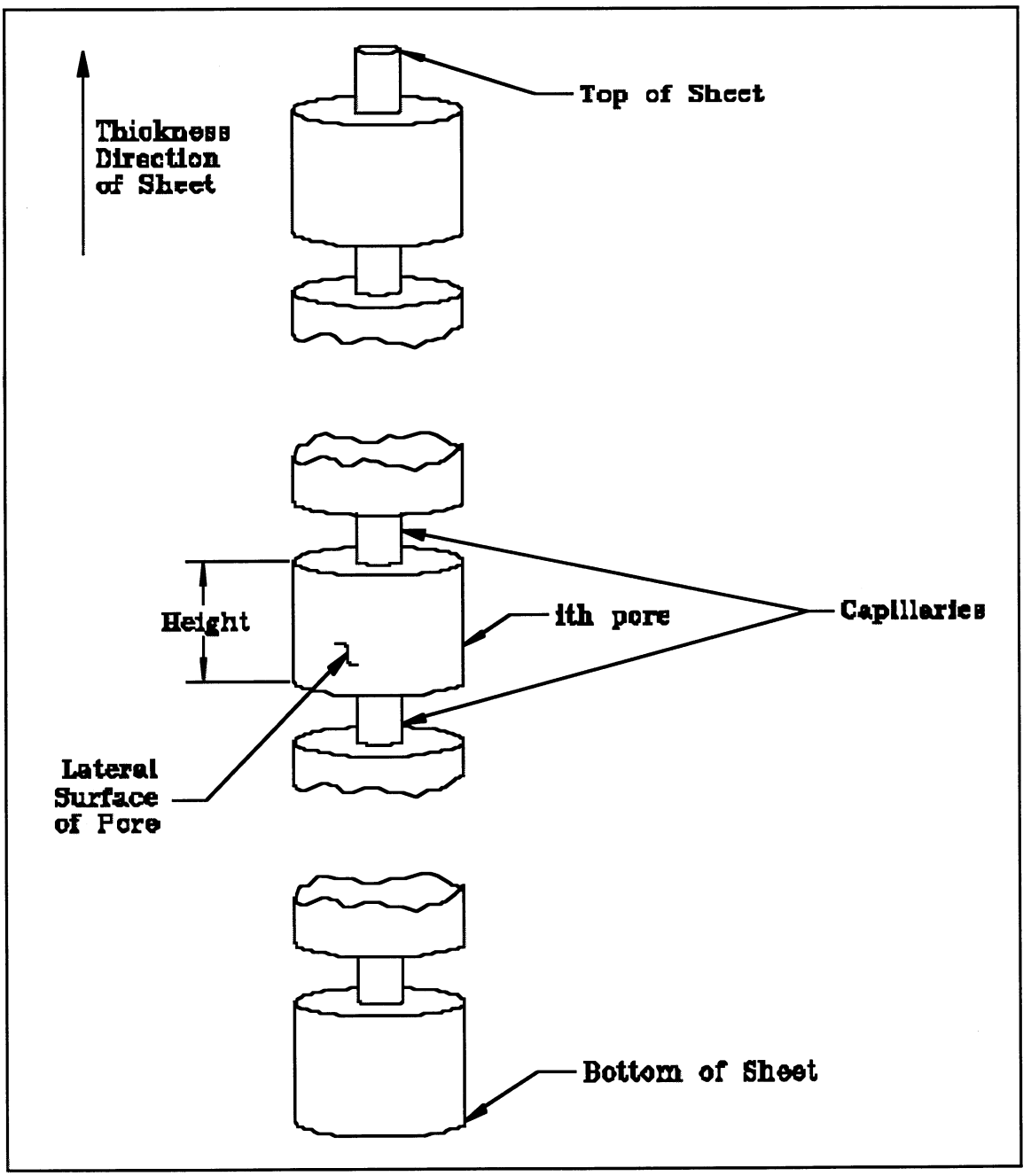

Figure D1. A Conceptualization of the Pore Structure of Paper

flash vaporization occurs as the sheet exits the nip. The pressure in the idealized i^{th} pore is taken to be spatially homogeneous and is denoted by $p_i(t)$, $t \geq 0$. As a consequence of the evaporation of water from the paper fibers which are idealized, in this model, as forming the lateral surfaces of the respective cylindrical pores, a very rapid buildup of pressure occurs in each pore. This increase in p_i, for any $i = 1,\ldots,n$, is exacerbated by the venting of water vapor into the i^{th} pore from the $(i+1)^{st}$ pore and is mollified by the venting out of water vapor from the i^{th} pore into the $(i-1)^{st}$ pore. For $i = n$ there is no venting into the pore, while for $i = 1$ the vapor is vented out through the top of the sheet.

At any given time $t > 0$, the pressure in the i^{th} pore, $p_i(t)$, exerts a force on the idealized "solid" upper boundary of the i^{th} cylinder whose area is just $\mathcal{A}_i = \pi\,(R_i^2 - r_i^2)$. This force serves to stretch the fibers which are idealized as comprising the lateral surface of the i^{th} pore, thus leading to an increase in the value of $H_i(t)$. The net increases in $H_i(t)$, $i = 1,\ldots,n$, as one goes from time $t = 0$ to any fixed time $t = T > 0$ are then thought of as accounting for the expansion of the sheet in the thickness direction over this time interval. The stretching of the fibers forming the lateral surface of each pore is influenced by the water content of the fibers at time t; this affects both the effective mass and the effective stiffness ratio of the fibers and is itself changing as a consequence of the flash evaporation process. The fibers comprising the lateral surface of the i^{th} pore are collectively thought of as behaving like a linearly elastic spring in this model, although viscoelastic effects could very easily be incorporated as well.

In principle, this model is quite simple. It is governed by two equations for each pore: one based on a spring equation with a time dependent external forcing function and one based on that specialization of the first law of thermodynamics in which it is assumed

that all the work done by the pressure field in any given pore goes into changing the internal energy of the pore with little or no change in the net heat content of that pore. For the i^{th} pore, our equations couple the temporal variations of $p_i(t)$ and $H_i(t)$, which are themselves coupled to the time evolution process in both the $(i-1)^{st}$ and $(i+1)^{st}$ pores as a consequence of the venting phenomena; exceptions occur at the geometrical extremes for $i=1$, where the process in the first pore is coupled to that in the second pore and the pressure $p_0(t)$ at the top of the sheet, and for $i=n$, where the process in the n^{th} pore is coupled only to the process in the $(n-1)^{st}$ pore. Here, we will present the model equations and give a brief discussion of their parameters.

The model is given by the following system of ordinary differential equations, for $i=1,\ldots,n$:

$$\alpha_i(t)\frac{dp_i}{dt}+\beta_i(t)\frac{dH_i}{dt}=\gamma_i(t),$$

$$m_i^f\frac{d^2H_i}{dt^2}+\frac{d}{dt}\left(m_i^w(t)\frac{dH_i}{dt}\right)=-k_i(t)\left[H_i(t)-H_i(0)\right]+\mathcal{A}_i p_i(t),$$

with the initial conditions

$$p_i(0)=p_i^0,\quad H_i(0)=H_i^0,\quad \text{and } \dot{H}_i(0)=0.$$

It is important to note that

$$\alpha_i(t)=\alpha_i(p_{i-1}(t),p_i(t),p_{i+1}(t),H_i(t),t),$$

$$\beta_i(t)=\beta_i(p_i(t)),$$

$$\gamma_i(t)=\gamma_i(p_{i-1}(t),p_i(t),p_{i+1}(t),t),$$

$$m_i^w(t)=m_i^w(p_{i-1}(t),p_i(t),p_{i+1}(t),H_i(t),t),$$

and

$$k_i(t)=k_i(p_{i-1}(t),p_i(t),p_{i+1}(t),H_i(t),t).$$

For this reason, our initial value problem involves a system of $2n$ second order, coupled, nonlinear, ordinary differential equations, with $3n$ associated initial conditions.

With this model in hand, the physical problem has been reduced to a mathematical one. The solution of this problem may be approximated using the existing techniques of computational mathematics. In fact, it is proposed that we use the perturbed nonlinear Gauss-Seidel iterative algorithm developed by Dey [D7], [D8], [D9], [D10]. To apply this algorithm, we first approximate the differentials with finite differences, discretizing the temporal variable and reducing our problem to a system of $2n$ coupled, nonlinear, *algebraic* equations of the form

$$F_1(p_0(t),\, p_1(t),\, p_2(t),\, H_1(t),\, t) = 0, \quad F_2(p_0(t),\, p_1(t),\, p_2(t),\, H_1(t),\, t) = 0,$$

$$F_3(p_1(t),\, p_2(t),\, p_3(t),\, H_2(t),\, t) = 0, \quad F_4(p_1(t),\, p_2(t),\, p_3(t),\, H_2(t),\, t) = 0,$$

$$\vdots \qquad\qquad \vdots$$

$$F_{2n-1}(p_{n-1}(t),\, p_n(t),\, H_n(t),\, t) = 0, \quad F_{2n}(p_{n-1}(t),\, p_n(t),\, H_n(t),\, t) = 0,$$

where F_j, $j = 1,\ldots,2n$, are appropriately chosen nonlinear functions and $t = t_m$, for $m = 0,1,\ldots,M$. To generalize the notation, we will write this system as

$$F_j = F_j(p_0(t),\, p_1(t),\ldots,\, p_n(t),\, H_1(t),\ldots,\, H_n(t),\, t) = F_j(\mathbf{x}(t)) = 0$$

for each $j = 1,\ldots,2n$ or, in vector notation, as $\mathbf{F}(\mathbf{x}(t)) = \mathbf{0}$. To begin the numerical analysis, we will assume that at each time step t_m, $m = 0,1,\ldots,M$, there exists an $\mathbf{x}_m^* = \mathbf{x}^*(t_m)$ such that $\mathbf{F}(\mathbf{x}_m^*) = \mathbf{0}$. Next, to apply Dey's perturbed iterative scheme (PIS), we rewrite the equations for $F_j(\mathbf{x}(t)) = 0$ as $x_j(t) = G_j(\mathbf{x}(t))$ for $j = 1,\ldots,2n$ or, in vector notation, as $\mathbf{x}(t) = \mathbf{G}(\mathbf{x}(t))$. Thus, we have that $\mathbf{x}_m^* = \mathbf{G}(\mathbf{x}_m^*)$ for each $m = 0,1,\ldots,M$; that is, $\mathbf{x}_m^*$ is a fixed point of $\mathbf{G}$ for each $m = 0,1,\ldots,M$.

To begin the PIS iterations, we make an initial guess of the value of $\mathbf{x}_m^*$, call it $\mathbf{x}_m^{(0)}$. At the k^{th} PIS iteration, our approximation to the solution has the form $\mathbf{x}_m^{(k)} = \mathbf{w}_m^{(k)} + \mathbf{G}(\mathbf{x}_m^{(k-1)})$, where $\mathbf{w}_m^{(k)}$ is called the k^{th} perturbation parameter for the m^{th} time step. This parameter is computed using data from the $(k-1)^{st}$ iteration and, as it becomes available, data from the k^{th} iteration. The addition of this parameter to nonlinear Gauss-Seidel iterations has two very desirable effects [D7]. First, the convergence rate of PIS is quadratic while that of Gauss-Seidel is linear. Second, it has been shown [D10] that in exact arithmetic, provided certain conditions on $\mathbf{G}$ are satisfied, the iterates $\mathbf{x}_m^{(k)}$ converge to the solution $\mathbf{x}_m^*$ if and only if $\lim_{k\to\infty} \left[\left\| \mathbf{w}_m^{(k)} \right\|_\infty \right] = 0$. Thus, at each iteration, we can check for convergence without any additional computational cost. It is hoped that a judicious choice of the finite difference approximations for our differentials will force $\mathbf{G}$ to satisfy the necessary conditions [D8].

As this point, no numerical experiments have been performed because some of the parameters needed for the model have not yet been determined. These parameters include the effective mass of the dry fibers comprising the lateral surface of the i^{th} pore, the initial mass of water contained in these fibers, the effective stiffness of these fibers (a quantity that will vary with the amount of water present), the initial heights of the pores, the lengths and radii of the capillaries as well as the radii of the pores, the effective permeability of the top surface of each pore, etc. However, it is believed that these parameters can be derived from existing experimental data. The matter is being explored.

Once the parameters have been determined, the last step of the numerical analysis will be to write a Fortran program to compute our approximate solution. This approximate

solution will include estimations of the heights of the pores through time. This information can then be used to predict when delamination will occur under different initial conditions; including the pressure applied to the top of the sheet.

3.) Future Work:

The next step in this project will be to attempt an expansion of the model. In the current model, henceforth referred to as the Phase I model, there are several assumptions which can easily be eliminated. First, it is assumed that any water lost from the fibers comprising the lateral surfaces of the pores has been changed to water vapor. This is not an entirely reasonable solution as the water may also flow downward through the sheet in liquid form. The first step in developing the Phase II model will be to allow for this possibility. Next, for the Phase I model, it is also assumed that any pressure buildup in the i^{th} pore will change only the height, $H_i(t)$, of the pore. Again, this is not a reasonable assumption as the pressure should also cause a "bulging" of the lateral surface of the pore. This possibility will also be incorporated in the Phase II model. Finally, and perhaps most importantly, it is assumed in the Phase I model that the pressure in the i^{th} pore, $p_i(t)$, is spatially homogeneous throughout the pore. This, again, is not an entirely reasonable assumption. In the Phase II model, we will allow for the possibility that the pressure in the i^{th} pore will vary throughout the pore. With this assumption, our Phase II model will become a system of second order, coupled, nonlinear, *partial* differential equations. At this point, we will again begin our numerical analysis. As for the Phase I model, the first step in the analysis for the Phase II model will to be approximate the differentials with finite differences, discretizing the temporal and spatial variables. This will again lead to a system of coupled, nonlinear, algebraic equations. It is believed that

the PIS algorithm may also be applied to this system. However, further mathematical analysis is necessary before this can be said for certain.

E. Sheet Expansion During Nip Opening Experiments

1.) Measurement systems development:

Information on dynamic compression of impulse-dried sheet is important for modeling vapor venting during the depressurization period of the impulse drying nip, as discussed in Section IV.D. of this report. Coupled with measurements of temperature profiles and moisture profiles, it will allow us to describe the impulse drying process in greater detail.

Measurement systems, have previously been developed to investigate web compression in a nip. They are based on several different physical principles.

A method using image analysis was developed for measuring the Z-direction density distribution of paper [E1]. For image enhancement, the pulp was tinted with methylene blue during refining. A gray image of the paper cross section was formed in such a way that the fiber wall area was darker than a certain gray value, and the void area lighter than the same gray value. The cross-sectional image was divided with the aid of image analyzer into many layers and the fiber wall area in each was determined. The density of each zone was assumed to be proportional to the fiber wall area. Appropriate calibrations were made which allowed the conversion of fiber wall area to density.

By tinting different layers different colors and making measurements over various nip periods, this system may be used to trace change in thickness of different sheet layers. Additionally, instead of tinting, thin colored films may be placed as targets in the layered sheet. It seems, however, that this procedure would be very time-consuming.

Reconstructing the pressing dynamics requires repeated pressings, the repeatability of which may be difficult to achieve.

Flash X-ray radiography (FXR) allows visualization of displacement processes inside a sheet and felt combination during impulse drying. It can capture rapid, transient events that occur in a 30-ns time frame [E2]. An X-ray-absorbent tracer may be placed on the surface of the sheet. Tracers (metal elements with high atomic number and density such as tungsten, lead, silver, etc.) provide the contrast needed to reveal compression characteristics. Aqueous solutions of the above metal salts have helped in the examination of flow characteristics. In Zavaglia's work [E2], a falling upper platen acted to trigger the FXR system. A triggering device using a photoelectric sensor was connected to a digital delay generator on the FXR system console. Various delay times could be set manually to observe the dynamics of compression (or fluid motion) at different nip times.

Strips from thick linerboard handsheets (440-490 gsm, unbleached Kraft, 650 ml CSF) were required in order to obtain the desired resolution [E2]. This may be the primary disadvantage of the FXR method because observation of the compression in 205-gsm liner would require examining the displacement in layers having basis weights of, at most, 50-100 gsm.

The measurement systems used by Burns, Burton, Chang, and Devlin [E3-E7] were based on an impedance variation caused by eddy currents induced by a sensor (transducer) in the metal target. The inductive measurement system developed by Chang [E6] made it possible to examine the dynamics of felt-and sheet compression and expansion in the nip. The transducers mounted in the pedestal tracked the displacement of the targets placed on either side of the sheet. These targets included a flat steel disk on the open felt surface and a flat steel screen between the felt and paper.

Chang's technique was extended to determine a density profile by using multiple targets placed at various levels in the sheet by Burton [E5] and Burns [E5, E6]. Schematic diagrams of the press configuration used are shown below.

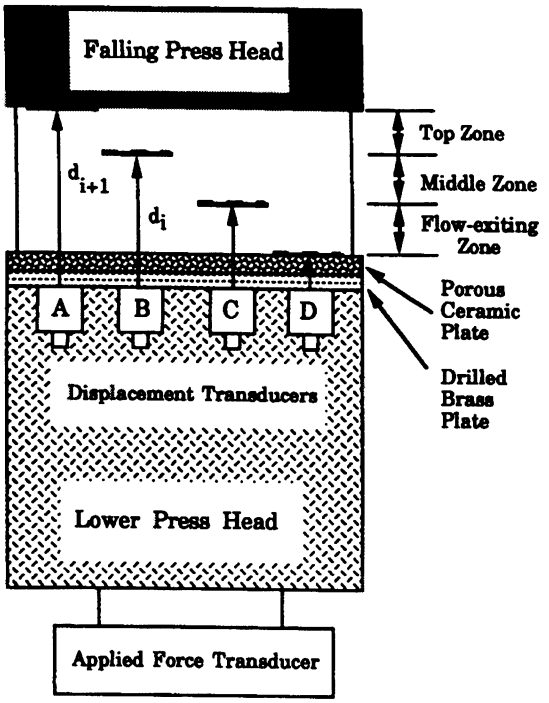

Figure E1.

Schematic diagram of Burton's Press Platens Used in Impulse-Drying Simulations.

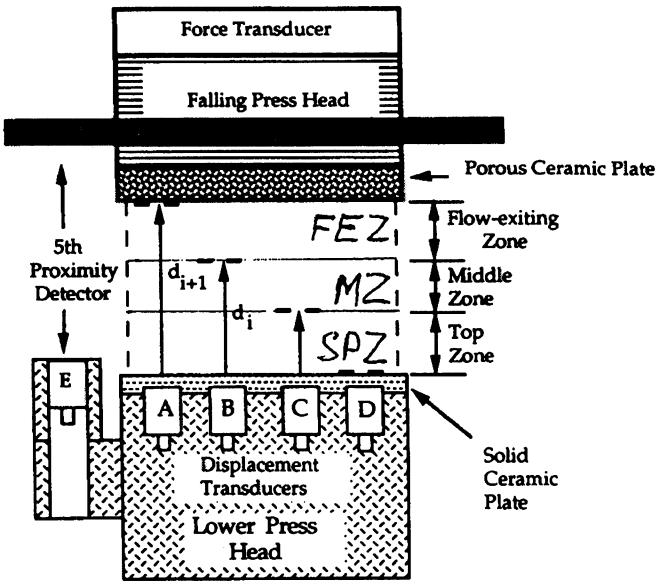

Figure E2. Press Heads Used by Burns for Drying Simulations.

These configurations allowed direct measurements of displacement in the nip as a function of the Z-coordinate and nip time. Despite the many experimental problems and difficulties that arose during the implementation of these systems, it seems that they are the most suitable methods for experimental observation of sheet compression and expansion in a nip.

The primary conclusion drawn from the results obtained by Burton and Burns is that the press configuration significantly affects the density profile of the sheets. Their work was conducted with porous incompressible ceramic plates functioning as water-receivers in place of compressible felts. As a result, they found that the density at the side of the sheet facing the porous ceramic plate was higher than the density on the opposite side. In contrast, the results of layered pressing, performed at IPST, indicated that when the sheet

was impulse dried in conjunction with a felt, the side of the sheet facing the felt had lower density than the side of the sheet facing the hot platen.

2.) Press configuration for sheet expansion measurement during nip opening:

To obtain realistic sheet expansion measurements, it was decided to conduct the experiments with felts. A schematic diagram of the press is shown in Figure E3.

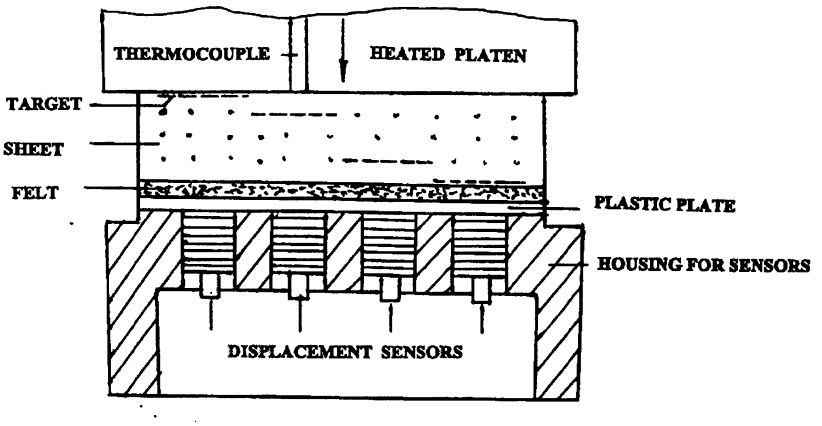

Figure E3. Schematic Diagram of the Press.

We intend to use four sensors for displacement measurements in the different levels of the sheet, and one sensor to track the displacement of the heated top platen. The effect of the heated platen position on the readings from the various sensors will be determined and corrected in the process of calibrating the sensor system.

The sheet will be impulse dried with a felt. To prevent deflection of the felt into the holes of the sensor housing (bottom plate), a plastic plate will be placed between the felt and top surface of the sensor housing. Potential plate materials were selected based on notched impact strength and hardness values [E8]. The final selecting will be made based

on a comparison of the performance of three materials: nylon, Lexan and acrylonitrile butadiene styrene.

Appropriate sensors were selected and ordered. Since their measurement range and accuracy determine the size of the sensor, the required measurement range was evaluated. The thickness of a sheet depends on its basis weight and ingoing solids. A 205-gsm sheet at solids 35% has a thickness of about 1 mm. The minimum thickness of a felt is about 2.2 mm, usually about 3 mm or more. The sensors will be mounted in the bottom platen of the press. The holes in the bottom platen will be drilled with space being cut out for better functioning of the sensors (not shown in the above schematic diagram). Deflection of the plate, between the felt and the bottom plate, should be minimized and its thickness will be of the order of 1.5 to 2.0 mm. For example, Burton's porous ceramic plates ranged from 1.7 to 2.0 mm. As a result, the thickness to be measured by the sensors will be in the range of 4.9 to 6.0 mm.

Since long-term stability, resolution, and thermal stability improve exponentially as the operating gap between the sensor and target decreases, the first half of the measuring range is recommended for high accuracy. This means that for our conditions, sensors with a measuring range of about 10 mm would be suitable. Preliminary review of available sensors indicated that the diameter of the sensor face is about 1.5 inches. This necessitates the use of a target having a diameter of 3.75 inches (sensors are unshielded). This means that even for a 5-inch diameter sheet, which is close to the maximum size for the MTS press, only one target would be able to be used.

3.) Selection of sensors and targets for compression measurements:

For this reason, it was decided to use sensors having a measuring range of up to 6 mm. This will likely result in nonlinear calibration curves. A partially shielded sensor, KD-2300-6C, manufactured by Kaman Instrumentation Corporation was selected.
To obtain maximum performance and stability the target should be at least 1.5 times the sensor diameter, for shielded sensors, and 3.5 times the sensor diameter, for unshielded sensors. Based on Kaman Instrumentation's recommendations, copper targets with a diameter of 31.8 mm, were selected. These are 1.65 times larger than the sensor face diameter of 19.3 mm. The diameter of the cut-out area is the same as the diameter of the target. The depth of the cut-out area is 7.2 mm.

The maximum sheet diameter for MTS pressing is 5 inches. For this sample size, the maximum applied pressure is approximately 1000 psi. For a larger sheet the available pressure decreases proportionally. Four targets, each of which is between 1.25 and 1.5 inches in diameter, can be placed in a 5-inch diameter sheet.

For good conductors such as copper or aluminum, operation is virtually independent of target thickness, down to one quarter of a skin depth. One skin depth is defined as the depth where the eddy current density is only 36% of what it is at the target surface. At two skin depths, the eddy current density is 13%. Skin depth may be calculated from equation

$$d = 50.3 (r/m/f)1/2, \text{ mm}$$

Where,

r = specific resistivity, mcom cm, (1.73 for Cu)

m = relative magnetic permeability, (1 for Cu)

f = frequency

At 1 Mhz, d= 66 mcm or 2.6 mils. Basing on these calculations, copper targets of 1 mil thickness and made of electroformed mesh were selected. The open area of the target was chosen to be 30%.

Kaman Instrumentation's multi purpose Variable Impedance Transducer KD-2300 and KD-2310 Series includes a sensor, cable, and a signal conditioning electronics package. The electronics consist of an oscillator, demodulator, linearization network, and amplifiers that provide an analog voltage that is directly proportional to the distance between the sensor face and any conductive target. The package includes an externally accessible zero, gain, and linearity controls. These systems require an externally regulated ±15 Vdc power supply such as the P-3400 or P-3500 Series. System synchronization is required to prevent beat interference (cross talk) between sensors when the sensors of two or more systems are mounted less than three sensor diameter apart.

The sensors and the target material are on order.

4.) Data Acquisition System:

In addition, a more versatile Data Acquisition System for the MTS press was developed. Now the output signals, that are proportional to the target displacement, are downloaded from the MTS Press directly to a MS-Excel worksheet. This enables easier graphing and requires less effort in post-measurement data manipulation. One experiment is saved as

one Excel workbook, single runs being saved on their own worksheets. In trials, the program has worked well and it can now be utilized for data collection.

5.) Future Work Plans:

- Once the sensors and the target material arrive, the sensors will be installed in the sensor housing and calibrated. The effect of adjacent targets and the top head of the MTS press on the calibration curve (output voltage vs. distance from the face of the sensor to the target) will be determined, and appropriate calibration procedures will be developed.

- The sheets with the embedded targets will be impulse dried on the MTS platen press. The following variables will be recorded as functions of time in the nip:

  - the total pressure curve,
  - the surface temperature of the platen,
  - the displacement of the top head of the press, and
  - the displacements of the targets embedded in the sheet.

- The value of the thickness, t_i, of each layer as a function of time in the nip will be calculated as the difference between the displacements of two targets positioned between two adjacent sheet layers, d_{i+1} and d_i. This will allow us to track the dynamics of sheet compression and sheet expansion in the nip during impulse drying.

- The data on the sheet compression and expansion will be incorporated in the theoretical model discussed in Section IV.D. of this report. Together, the data and model will allow us to better understand and control flash vaporization and steam venting during nip opening, and further reduce the furnish sensitivity of the impulse drying process.

While the goal of the dues-funded project (Project No. F001) is to expand the operating window of impulse drying technology, the objective of the DOE and Beloit-funded project (Project No. 3595) is to demonstrate that board grades can be successfully impulse dried on a continous, high-speed pilot paper machine. In the following five sections, progress toward meeting the goals of Project No. 3595 will be discussed.

F. High-Speed Infrared Detection of Coated Roll Surface Defects

1.) Summary:

Ceramic coatings have become an important component of paper-machine press rolls with their increased use in granite roll substitutes and recent use in impulse drying. Given these developments, one would like to know how well ceramic coatings withstand thermal and mechanical cyclic loading over an extended period of time. Using infrared thermography techniques, it should be possible to determine when and how the ceramic coatings fail; coating failures are detected by temperature differentials between a defect and the surrounding coating. To establish how well infrared thermography can detect defects in a ceramic coating, a study was conducted using a high-speed, high-resolution infrared thermal imaging and data acquisition system. A press roll rotating at 328 rpm (628m/min, 2061fpm), with coating defects of various shapes and sizes, was imaged. The defects were classified as either circular or line defects based on their shape and method of forming. Resolution of 2.38 mm (3/32 inch) was achieved with the circular defects and a resolution of 1.59 mm (2/32 inch) with the line defects. The dimensional accuracy of the method was also quantified. The successful identification of these defects supports the implementation of infrared imaging as a viable method of identifying coating failures at high roll speeds.

2.) Introduction:

Coated surfaces have been recognized [F1-F3] as an integral factor in preventing sheet delamination during impulse drying of linerboard. Coatings that possess low conductivity, low density, and low specific heat control energy transfer to the sheet, thus reducing flash evaporation inside the sheet during nip depressurization. Ceramics and some cermets

have these properties. Initially, machinable ceramics were tested with impulse drying, but recent developments have led to the use of plasma-sprayed ceramics and cermets. Plasma-spraying reduced the cost of ceramic roll coatings and made possible the use of cermet roll coatings.

This work is part of a larger study to determine the long-term durability of plasma spray coatings in the impulse drying application environment. As a first step in that work, a method for detecting roll coating defects while the roll is moving was in need of development. This paper discusses the experimental apparatus that was built to conduct the roll surface durability study and the methods to be used in detecting roll defects as they may develop with time.

Infrared detection of material defects is a commonly used NDE (Non-Destructive Evaluation) method [F4-F10]. A number of researchers have developed experimental techniques for detecting defects in coated materials using IR NDE. Connolly [F5], investigated detection of subsurface defects in various coating/substrate combinations, including ceramic/metal, metal/metal, and ceramic/ceramic structures. McKnight and Martin [F7], developed a method for detecting defects in organic coatings on steel substrates. Ogura and Sakajami [F6], investigated defects in metal plates with attention given to the differences between defects oriented either perpendicular or parallel to the plate. Satonake et al., [F8], performed a similar study which concentrated on defects in welds. All of these studies involved stationary objects. In addition, all the measurements were made using transient heating of the objects. The object was initially at ambient conditions; it was then heated for a short period of time (several milliseconds to several seconds). The infrared measurements were taken during that time period.

The study reported in this paper involved detecting small defects in a coated roll continuously maintained at an elevated temperature and rotating at over 300 RPM. The only similar study reported in the literature was by Lahdeniemi et al. [9]. That study reports on IR temperature measurements of paper-machine felts moving at 600-1200 m/min.

Coating failures are hypothesized to develop in either of two forms:

- A surface defect, where the bond between a section of coating and the substrate has failed and the section of coating is removed, exposing the metal surface below.
- A subsurface defect, where the bond between a section of coating and the substrate has failed but the coating remains on the object, creating an air-filled blister-type structure.

In this experimental set up, the induction heater produces eddy currents in the steel shell of the roll causing the shell to heat due to Joule heating. Thus, the first type of defect would appear as a hot spot because the ceramic coating around the defect would act as a thermal insulator. The second type of defect would appear as a cold spot because air has low thermal conductivity [7].

3.) Using Infrared Thermography to View Coating Failures:

As discussed previously, IR thermography is a widely used NDE tool for detecting surface and subsurface flaws in coated materials. IR detectors look at the intensity of

photon radiation emitted by an object. In theory the blackbody radiation intensity is governed by Planck's law, which varies with wavelength and temperature:

$$I_{\lambda,b}(\lambda,T)=\frac{2hc_o^2}{\lambda^5\left[\exp\left(hc_o/\lambda kT\right)-1\right]} \quad \text{(F1)}$$

Where λ is the wavelength, T is the absolute temperature of the blackbody, h is Plancks constant, c_o is the speed of light in a vacuum, and k is the Boltzmann constant [F11]. The IR scanner used in this study is a short wavelength scanner and only detects photon radiation with wavelengths in the 2 to 5.4μm range utilizing a limited solid angle [F7]. This allows temperature to be the only variable.

The objects imaged in this study are gray bodies and not blackbody emitters. The spectral properties of the object consist of the absorptivity (α), emissivity (ε), reflectivity (ρ), and the transmittance (τ). These factors all must be taken into consideration when determining the temperature of a gray object. Assuming the coatings are opaque, then the transmittance (τ) of radiation through the object is equal to 0. From blackbody theory, the sum of the absorptivity (α) and reflectivity (ρ) must equal 1. Kirchoff's law states: $\varepsilon = \alpha$, therefore, the object reflectivity can be determined from the emissivity. The AGEMA 900 system allows the object emissivity to be specified. The system also compensates for transmission through the atmosphere [F7, F10-F11]. For this study only relative temperatures were of importance, but it was attempted to record as accurate temperatures as was possible. Therefore, the emissivity of the coating surface was estimated to be 0.86 from the known emissivity of other like ceramic coatings and the atmospheric transmittance was calculated using an AGEMA algorithm.

4.) Equipment:

a. Roll/ Machine

Figure F1 shows the apparatus. The primary components of the apparatus consisted of a single-nip roll press; an induction heater used to heat the upper press roll; a high-speed, high-resolution thermal imaging system; and a continuous wet felt which passes through the press nip. The lower (unheated) roll had a 12.7-mm (0.5 inch) thick polyurethane coating. The upper (heated) roll had a three layer plasma sprayed coating. The base layer, applied directly to the steel roll, was a metal alloy bond coat. The middle and thickest layer, was a partially stabilized zirconia (PSZ) coat. The top, or outside, layer was a dense (reduced void volume) PSZ coat. The combined thickness was approximately 0.762 mm (0.030 inch). The top coating was diamond ground to a 1.01 μm R_a finish [F1]. The ceramic-coated roll was heated to 200°C (392°F) by the induction heating system. The induction heater produced electromagnetic eddy currents within the steel shell of the roll, resulting in heating of the shell. The heat was transferred from the steel to the thin ceramic coating by conduction. The roll constantly rotated beneath the induction heating coils, giving constant and even heating. The roll temperature (200°C) was chosen because it is comparable to the temperature at which an impulse dryer press would operate. The peak nip pressure was 6.9 MPa (1000 psi). A wet felt was passed between the two rolls to quench the heated roll and hence to create a cyclic thermal and mechanical loading on the coating. The rolls rotated at 328 rpm, which translated to 628m/min (2061 fpm) based on the 0.61-m (2 ft) roll diameter. This speed was comparable to conventional linerboard machine speeds.

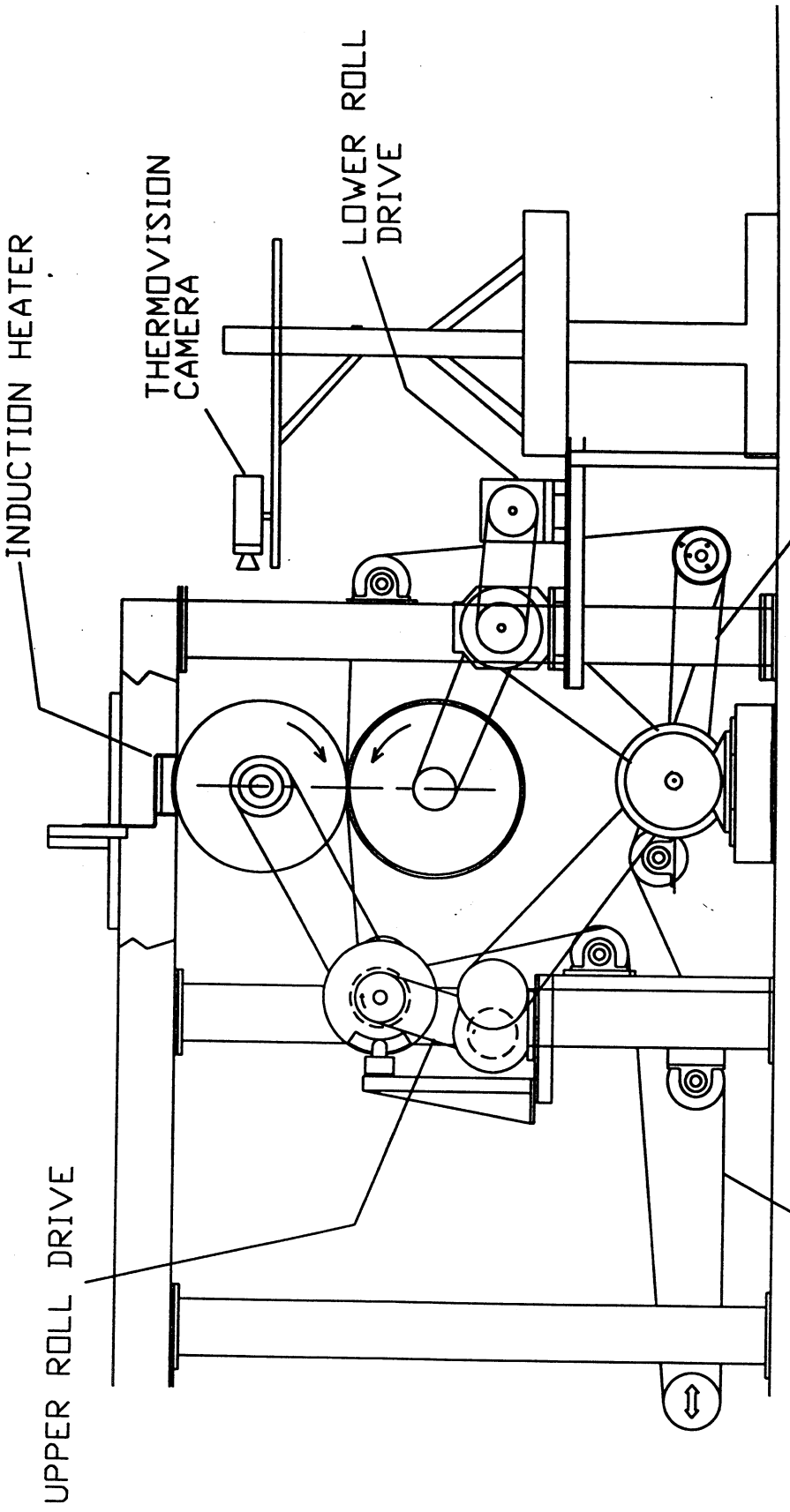

FIGUREF1. SIDE VIEW – ROLL DURABILITY TEST STAND

b. Defects

The defects were placed on the drive side of the roll in the machine direction. Forty-five defects, varying in shape, size, and depth, were made in the roll coating. The coating defects were produced using standard drill bits and milling machine bits for the circular defects and grinding wheels of a variety of thicknesses for the straight line patterned defects.

There were a total of 37 circular defects, 24 of which were made with standard drill bits. The bit sizes were: 0.79, 1.19, 1.59, 2.38, 3.18, 3.97, 4.76, and 5.56 mm (1/32, 3/64, 2/32, 3/32, 4/32, 5/32, 6/32, and 7/32 of an inch). The holes were placed in rows of three holes for each defect size, making a total of eight rows. Three holes were used for each size defect to increase the number of data points. This also made possible a study of variability across the roll in the horizontal direction. Depths of the defects were approximately the same for all defects, the center of the defect extended through the coating to the base metal. The remaining 15 circular defects were made using milling bits. Milling bits were used on the larger defects because as the drill bits size increased the tip camber also increased. The larger drill bits would produce an excessively deep defect, one that extended significantly into the base metal. The mill bits have a flat tip which allows for a shallow defect with a uniform depth. The mill bit sizes used were 3.97, 4.76, 6.35, 7.94, and 9.53 mm (5/32, 6/32, 8/32, 10/32, and 12/32 of an inch). The defects varied in actual size from the specified mill bit size due to cracking of the ceramic around the edges of the defect.

Seven of the remaining defects were comprised of different length, width, and depth lines. The line defects were made using a grinding wheel. Depth was determined by visually inspecting the defect to see whether the surface of the coating had been partially

penetrated or if the defect extended to the steel roll surface. The thickness of the line defects ranged from 0.40 to 3.18 mm (1/64 to 4/32 of an inch). Three defects were made to demonstrate the distinction between defects of the same shape, but with increasing thicknesses of 0.79, 1.59, and 3.18 mm (1/32, 2/32, and 4/32 of an inch). Another set of two defects were made to highlight the effect of varying thickness and lengths of line defects in the horizontal and vertical directions. These defects were more complex comprising at least five lines per defect. A set of two defects were made in the pattern of a diagonal cross to study the effect of imaging diagonal lines on the roll surface. These defects were made with varying depths (scraped to the bare steel or not to the bare steel) and different thicknesses: 0.40, 0.79, and 1.59 mm (1/64, 1/32, and 2/32 of an inch). The final line defect was made by scratching the surface of the ceramic coating.

c. Scanner/Data Taking

An AGEMA 900SW/TE thermal imaging system was used to acquire all of the data. The system is a high-speed, high-resolution thermography tool. It is comprised of a thermo-electrically cooled IR scanner, a high-speed system controller with a 1Gb hard disk and a 32 Mb ramburst for high-speed data acquisition, a high-resolution video monitor, and an external 1.3 Gb optical disk drive for data back-up and storage. The scanner was provided with a 40 degree FOV IR lens. The scanner has the capability of scanning at a rate of either 20 or 30 Hz. It also has the capability of line scanning at a rate of 3.5 kHz.

The scanner focal plane was positioned approximately 10 cm (4 inches) from the roll surface. Given the 40 degree FOV lens, the resulting image encompassed only the section of the roll containing the defects. The scanner imaged the roll through a PFA Teflon window (thickness = 2.29 mm (0.090 in.)) which was fixed to a stainless steel internally

cooled enclosure to prevent the scanner from being damaged by the high temperatures and the extreme humidity. The enclosure was cooled using a compressed air vortex cooler in conjunction with a thermocouple probe monitoring the temperature. The PFA Teflon window attenuated the IR transmittance to the scanner. The transmittance through this particular IR window was determined to be, $\tau = 0.26$. The transmittance was calculated using the AGEMA systems option of inputting an estimated transmittance value into the temperature calculation algorithm, in conjunction with a surface thermocouple probe on the coating surface. This transmittance was input into the temperature calculation algorithm to compensate for the attenuation.

Data was taken at a rate of 3.5 kHz over a 10-s period and recorded directly to the ramburst drive. The data was taken while the scanner was in line scanning mode. The thermal imaging system has the ability to create a single high-resolution image from a line scan file of multiple cyclic images that are triggered at each cycle. It accomplishes this by comparing all of the synchronized cyclic images and interlacing lines from different images together to form a more detailed image. To synchronize the line scan with the roll rotation a magnetic pick-up was added to the top roll shaft of the machine to trigger the system every roll revolution. The computer then compiled 40 revolutions of data into one complete high-resolution line sequence of one roll revolution that contained 3227 lines.

5.) Results:

Results were analyzed using the AGEMA Erika software, Microsoft Excel for 3-D surface plots, and Harvard Chart XL for 2-D contour plots. The AGEMA software was set up to dump an image file into an ASCII format file that then can be imported into

DOS. The file format was set up in the form of a 2-D pixel array with the individual array element values corresponding to the temperature associated with the pixel.

Each defect was measured by a 1/64-inch scale (error = ±1/128 inch) on the roll surface to find the actual dimensions of the defects. The thermal image of the defects were inspected to find the dimension of a single pixel. The AGEMA system has the capability of analyzing images on the pixel level of resolution. To determine the relationship of a pixel to a unit of length the distance between the centers of the circular defects were measured in the cross machine direction. The true distance between centers was physically measured on the roll surface. This value was divided by the corresponding number of pixels to determine the unit of length to pixel relationship. The AGEMA software was then used to measure the diameters, lengths, and widths of the defects in pixels which were then converted to a unit of length.

The imaged section of the roll face was 129.5-mm (5.1 inches) wide. The acquired image had an obvious temperature gradient across the roll face. The temperature gradient made possible the comparison of similar defects at different temperatures. The gradient ranged from 163°C (325°F) at right edge of the roll face to 193°C (379°F) at the left edge of the roll face. The cause of the gradient was due to the felt/roll interaction. Since the felt was only in contact with the center 0.38m (15 inches) of the 0.61m (24 inches) roll width, 0.11m (4.5 inches) on each edge of the roll face was not exposed to the cooling effect of the felt. This created a parabolic temperature profile across the portion of the roll face that was in contact with the felt, with the edges of the felt warmer than the center.

a. Resolution

The reconstructed images were comprised of 3227 lines (or 3227 pixels in length). This number of lines produced an isomorphic image of the coating (an image that is scaled equally in the vertical and horizontal axis). Based on a roll diameter of 0.61m (2 ft), the resolution of the image was the circumference (0.61 * π m) divided by 3227. This gave a resolution of 0.593 mm/line (0.0234 inch/line). This resolution corresponds with the value of 0.572 mm/line (0.0225 inch/line) calculated from the center-to-center measurements, and showed that the resolution around the roll (vertical) was roughly equivalent to the resolution across the roll (horizontal).

b. Circular Defects

The thermal images of the circular defects had good resolution and well-defined shapes for the larger diameter sizes. The minimum hole diameter identified using the AGEMA thermal analysis software was 2.38 mm (3/32 inch). This was determined through the measurement of the pixels that comprise the defects in the thermal image. The drill holes of sizes 1.59 mm (2/32 inch), 1.19 mm (3/64 inch), and 0.80 mm (1/32 inch) were not visible with the thermal imaging equipment. These defects apparently were not generating enough of a temperature difference to be visible. The 1.59-mm (2/32 inch) defect was discernible on the 3-D surface plots, but it was very difficult to distinguish between the defect and thermal abnormalities in the coating surface. The 1.19-mm (3/64 inch) and 0.80-mm (1/32 inch) defects were not detectable on the 3-D surface plots. After examination of the thermal data in spreadsheet format, the 1.19-mm defects could be identified.

It is believed that the last three rows of drill defects were difficult to distinguish because of a low temperature difference (ΔT) between the surface of the defect and the surface of the defect surroundings. The maximum defect temperature ($T_{mx,def}$) was low compared with the other defects. This would cause a low ΔT due to the average surrounding temperature ($T_{avg,surr}$) remaining constant. After visual inspection of the defects, it was determined that these defects did not penetrate into the steel shell below the cermet. This prevented the steel shell from being exposed, which caused the remaining cermet coating to become an insulator (due to the low thermal conductivity of the cermet) and decreased the $T_{mx,def}$. Therefore, for good defect recognition, the coating must be fully removed. Partial removal that retains a thin layer of cermet on the steel shell does not produce a large enough temperature difference to accurately determine if a small defect is present.

It was found that the actual diameter of the circular defects was smaller than the diameter measured using the AGEMA software (Figure F2). It is believed this is due to edge effects. This may be caused by thermal radiation from the higher temperature bottom of the defect to the lower temperature sides of the defect. An analysis of a cross section of the thermogram showed a ramping of temperature outside and inside the boundary of a defect.

Cross-sectional analysis of the thermograms also showed that the mill defects plateau at a maximum temperature with gradients on the defect boundaries. The drill defects peak at a maximum temperature and have a sinusoidal shape. It is believed this observation can be explained by the differences in the geometry of the mill and drill defects.

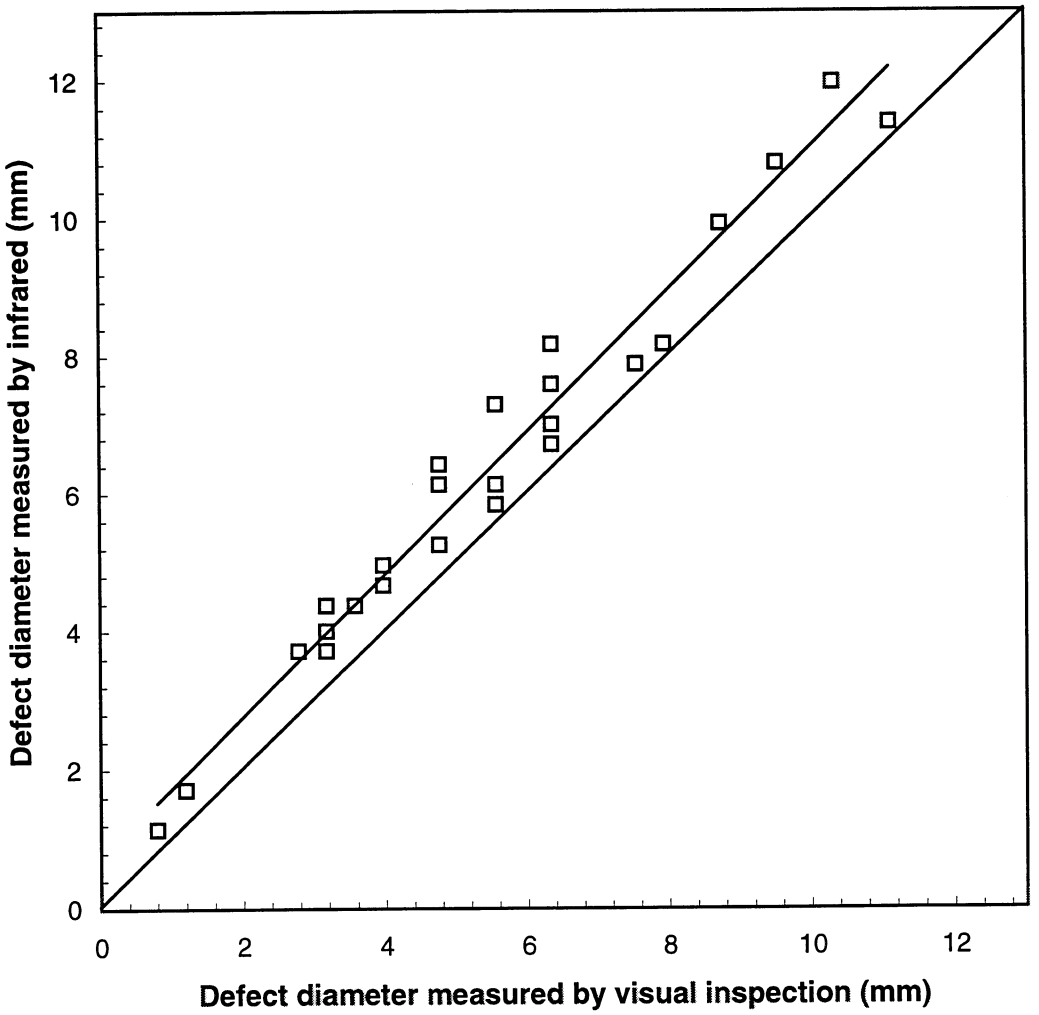

Figure F2 - Comparison of defect diameters (mm) by method of detection

The geometry of the defects can be modeled as a cavity, the mill defects having a cylindrical cavity and the drill defects, a conical cavity. The geometry of the mill defects has a flat interior surface with all of the cermet coating removed, exposing the steel surface below. The drill defects have sloped sides that extend to a central point below the surface of the roll; the camber of the defects is assumed to be that of the drill bits ~118 degrees. Therefore, the flat surface of the mill defects produces a temperature plateau, and the drill defects produce a peak temperature.

Through the use of the 2-D spreadsheet data and the AGEMA software, a comparison between the peak defect temperature and the average of the temperature immediately surrounding the defect was made. This showed that the temperature differential between the defect and its surroundings remained constant along the CD of the roll. Furthermore, because of the presence of a temperature gradient along the CD of the roll face, this analysis showed that defects of similar size, shape, and depth are independent of their surrounding temperature and will consistently show an equal temperature difference (see Figure F3).

It was also observed that as the defect diameter increased the temperature difference between the defect and its surroundings flattened out. Figure F4 shows a sloped set of data which flattens at the larger diameters (which are mainly mill defects). It is believed that the smaller defects did not have as large DT due to the lower surface area of exposed steel. The smaller drill defects are shallower than the large diameter drill defects; due to the conical geometry, the shallower defects have less surface area of exposed steel. As stated before, the exposed steel surface generates the maximum defect temperature.

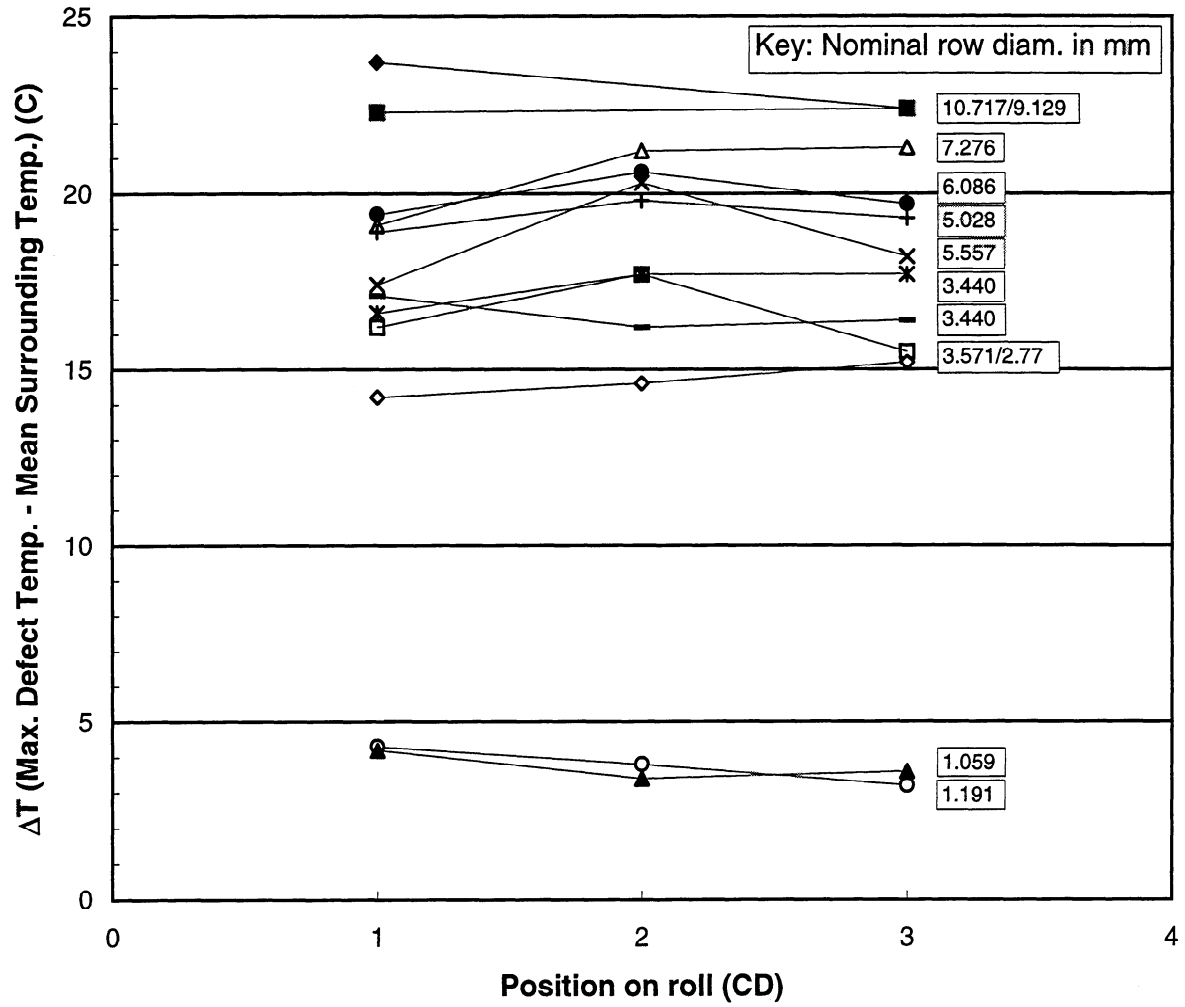

Figure F3 - Temperature differentials for circular defect rows (mill and drill bits)

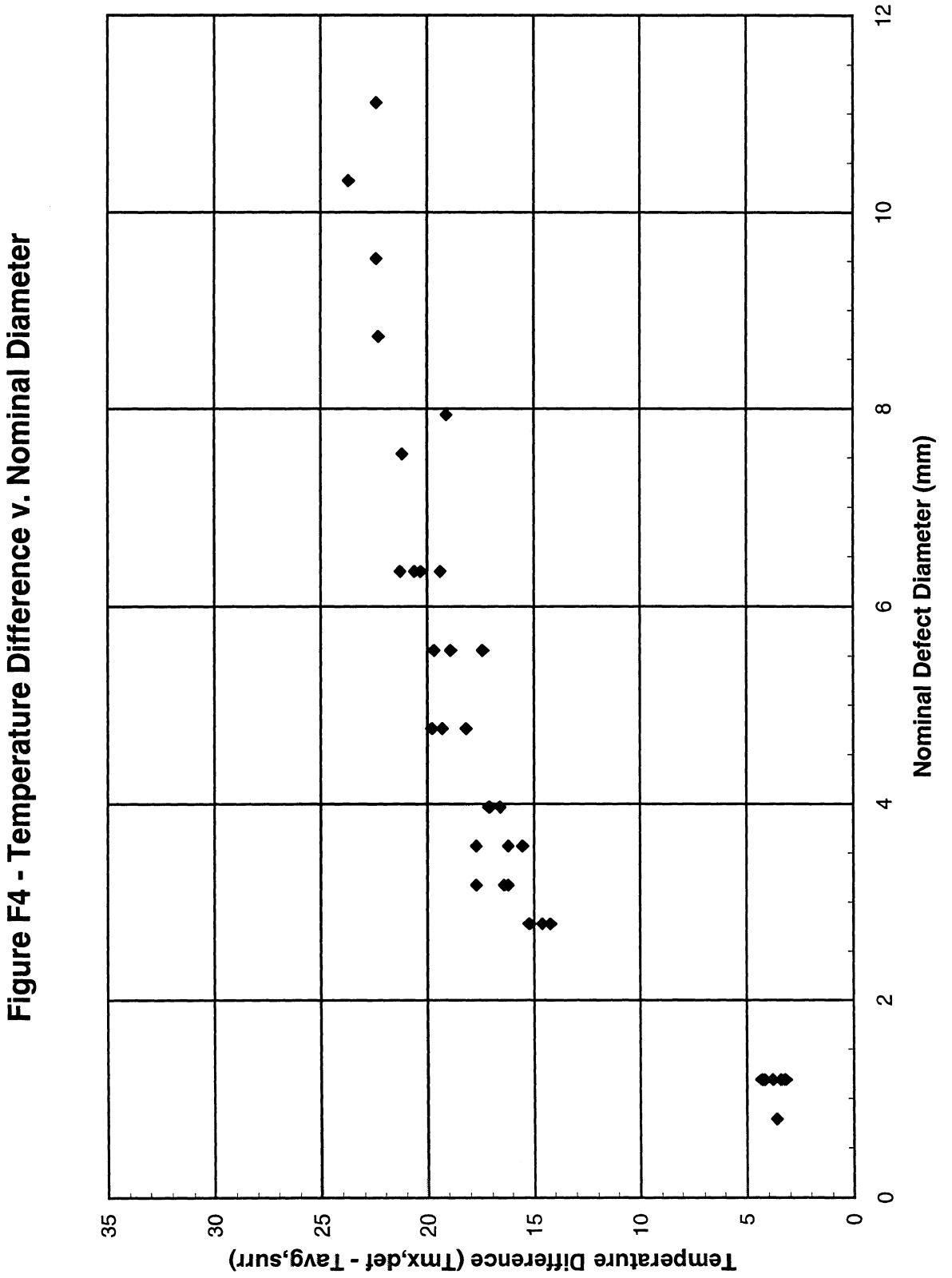

Figure F4 - Temperature Difference v. Nominal Diameter

c. Line Defects

The line defects proved consistent with the circular defects in as much as the narrowest detectable line width with the thermal imaging system was 1.59 mm (2/32 inch). These images were again analyzed using the AGEMA software, 3-D surface plots in Microsoft Excel, and two-dimensional topographical contour plots in Harvard Chart XL.

The greater detectability of line defects can be explained by the temperature differential between the defect and the surrounding surface. Infrared scanners determine temperature by detecting the intensity of infrared radiation absorbed by the scanner. Therefore, a larger temperature differential between the defect and the surrounding surface will render the defect more detectable. Circular and line defects with similar widths contained different temperature differentials. The difference is attributed to the shape of the defects; the line defects had square edges and the circular defects had sloped edges. The defect shape was dependent on the method of defect fabrication, which was previously explained. Using a 3-D surface plot of the defects in Excel, the cross-sectional profile of the 1.59 mm (2/32 inch) circular and line defects were analyzed. The 1.59-mm (2/32 inch) line defects were recognizable on the AGEMA system, but the 1.59-mm (2/32 inch) circular defects were not. It was observed that the circular defect profile contained a smaller temperature gradient at the defect edge (see Figure F5).

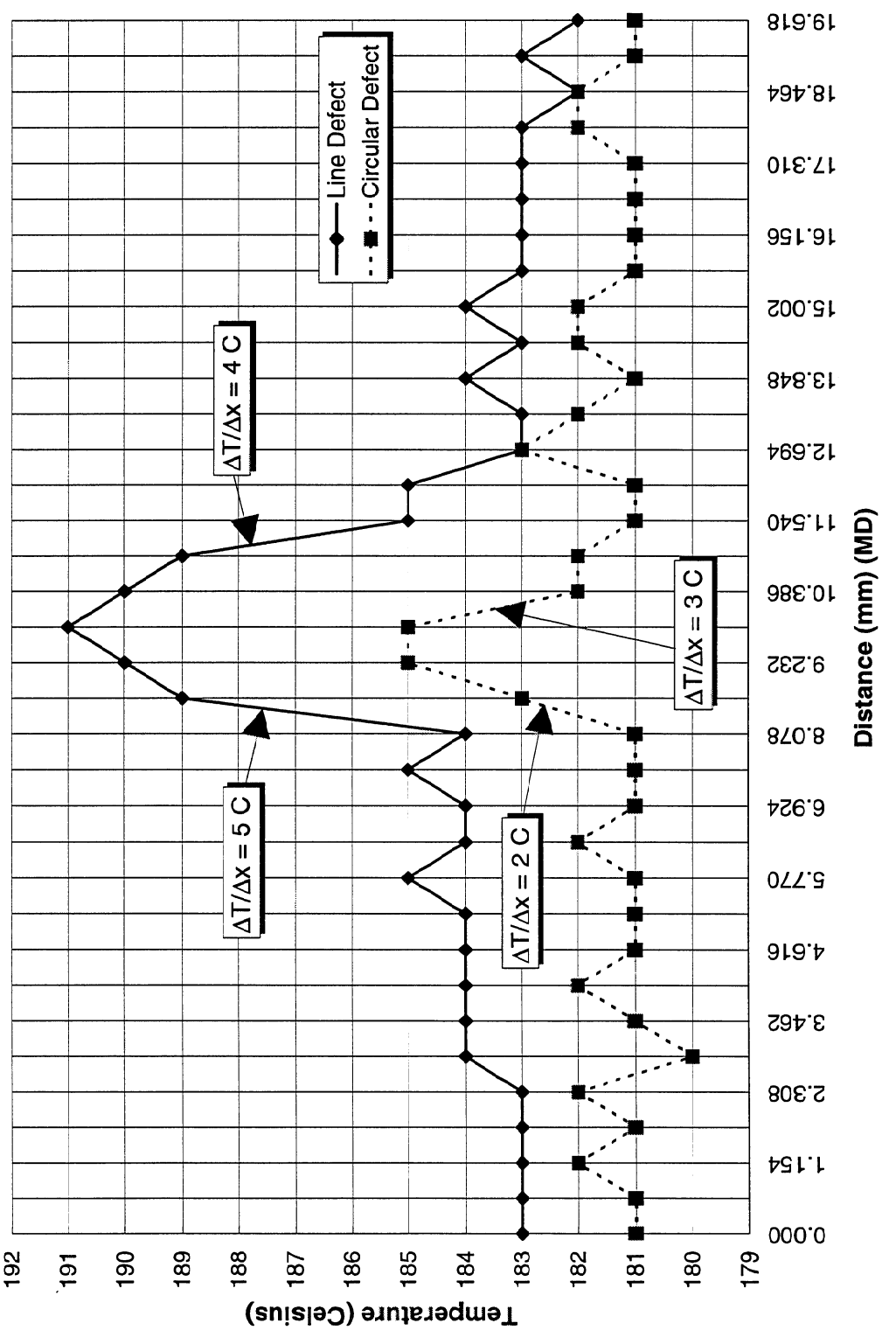

Figure F5 - MD Temperature Profile Comparison - Line v. Circular Defects (~1.39 mm)

The cross line defects followed a pattern consistent with the other line defects. Each defect was comprised of two lines, and each line was of a different thickness. The crosses also had lines of different depths, either extending completely to the metal surface or only partially through the cermet coating. A 0.40-mm (1/64 inch) line did not extend through the cermet. This line was not detected by the AGEMA system. A line of 0.79 mm (1/32 inch) showed a temperature of less than the temperature of the surrounding environment. This line was deeper than the 0.40-mm (1/64 inch) line, but did not extend to the metal. The line of 1.59 mm (2/32 inch) was clearly visible and had an increase in temperature of approximately 4 to 5 degrees centigrade over the surrounding temperature; this line was cut to the metal. It is believed that the 0.40-mm (1/64 inch) line was not detected because it did not penetrate deep enough into the cermet coating to provide a large enough temperature differential between the defect and the surrounding coating.

The two line defects comprised of vertical and horizontal lines demonstrated similar results. The first defect contained lines of the same thickness, 0.79 mm (1/32 inch), but one-half of the defect had lines cut to the metal and the other half had defects that were not cut to the metal. The lines that were not cut to the metal shell were detected as having a negative temperature differential with the surrounding coating surface. The opposite was observed with the lines cut to the metal shell, these lines were detected as having a positive temperature differential. The second defect showed a positive temperature differential on every line. The lines were all approximately 1.59-mm (2/32 inch) thick. Negative temperature differentials were observed on the tips of many of the lines. The line tips ranged from 0.40 to 0.79 mm (1/64-1/32 inch) in thickness. Also, the tips of the lines were sloped because of the curvature of the grinding wheel. This created a cut not to metal, but only into the cermet coating.

One possible explanation why some lines produced negative temperature differentials was that these lines were of narrow thicknesses. Once the roll was stopped, the defects were examined. The narrow defects had felt fibers embedded in the defect, possibly entrapping air and producing a blister like defect or altering the emissivity at that location.

6.) Conclusions:

The resolution at which surface defects can be detected by thermal imaging was determined. The smallest circular defect that could be detected was 2.38 mm (3/32 inch) in diameter. The smallest detectable surface scratches (line defects) had a width of 1.59 mm (2/32 inch). This was slightly better than for circular defects. This was attributed to the cross-sectional geometry of the line defects, which allows a greater thermal gradient at the edge of the line defect.

Circular defects on the same horizontal axis demonstrated similar temperature differentials between the defect and the surrounding coating. These differentials remained similar despite the presence of a temperature gradient along the same axis. The temperature differentials decreased as the defects became smaller in diameter.

The differences between the measurements made using the AGEMA system and the physical measurements of the roll are believed to be due to edge effects. A small amount of heat is believed to be conducting past the edge of the defect and transferring to the surrounding coating. This creates a defect on the thermal image that is slightly larger (0.58 to 1.15 mm) in diameter than the actual defect.

The technique of using high-speed infrared imaging to detect roll coating failures has proven to be an excellent method. The resolution achieved with this method can detect defects that could escalate into costly damages to paper rolls and press sections.

G. Status of Roll Coating Durability Test

The objective of the Roll Coating Durability Test is to quantify the durability of four specific coatings: Beloit "E," Beloit "A," NiCr/ZrO, and Beloit "AZ". Three are proprietary coatings and one was designed by IPST. Documentation was in the form of infrared thermography, using a high-speed IR scanner. The initial stage of the test, which is to mechanically and thermally cycle the coatings, is nearing completion. Future stages, doctoring the coatings and running linerboard through the nip, are outlined below.

1.) Status/Test Conditions:

The roll has been subjected to mechanical and thermal cyclic loading for approximately 4.56 million cycles. These cycles have accrued over the past six months. An initial break-in period at room temperature accounts for 334,000 cycles.

Two different felt types have been used for the test which were supplied by Albany International. Both felts were 0.38 m (15 inch) wide. The roll was 0.61 m (24 inch) wide. Each have exhibited degradation and have deposited residue on the roll coatings, which had to be removed. Felt moisture content ranged from 25-30% for both felt types. Felt type 1 was initially placed on the roll upside-down and run backwards (the felt was turned right side up one-third of the way through the test). It was run for approximately 3.36 million roll cycles (1.42 million cycles upside-down). This felt showed felt degradation (shedding of batting) and deposits on the roll coating surfaces. The felt was run until a significant amount of batting fibers had deteriorated and base fabric fibers could be seen. Felt type 2 was run for 1.2 million cycles and in the correct direction and orientation. This felt type had an increased deposit rate on the roll coatings over felt type

1 but did not show an increased amount of felt degradation. It was observed that the residue deposited on the coatings was easier to remove on the two outer coatings: Beloit "E" and Beloit "AZ". It is believed this was due to the fact that these coatings maintained a higher temperature during the test than the two center coatings. Also, felt deposits would form in circumferential strips on the roll surface. This may be due to an uneven heating of the roll or an uneven felt wash.

The entire test has been run under the same process conditions. Ranges can be seen in the table below. The temperature range is due to a CD roll temperature profile which results in lower temperatures at the roll center and higher temperatures at the roll edges. The felt moisture and web velocity were varied during the test. A Uhle box was not used on the felt. A doctor blade was not used on the roll. Test conditions:

Peak Temperature Range	180 - 230 °C	356 - 446 °F
Nip Peak Pressure	6.9 MPa	1000 psi
Web Velocity Range	305 - 762 m/min	1000 - 2500 fpm
Felt Moisture Range	25 - 30%	
Felt Tension	4.4 kN/m	25 pli

2.) Future Testing:

a. Doctoring

A wear study will begin immediately following the completion of the cyclic loading stage of testing. A doctor blade will be placed on the roll during operation. The doctor loading for each individual coating will be monitored. The thickness of the coatings will be

measured for decreases in thickness (total material removed) by a magnetic induction instrument which will be calibrated for each coating.

A doctor blade holder is already installed on the exit side of the nip of the upper roll. The blade angle will be predetermined and will not be adjustable (angle range 27 to 30 degrees). The blade holder oscillates with a stroke of about 15 mm (0.59 inch). The blade loading is controlled by a threaded rod connected to the blade holder lever arm. The blade used for this test is a Vickery Biovick Super synthetic blade. It is designated for high temperature rolls and has a 1.4-mm (0.055 inch) thickness.

Infrared imaging of the coatings, while the blade is in contact with the roll, will be performed. The IR images will show abnormal wear patterns due to the doctor blade in the form of hot streaks on the coatings [G1]. The hot streaks can be correlated to the pressure profile of the doctor blade.

While the doctor blade is in contact with the cermet coatings, it is hypothesized that the coatings will wear in the z-direction. The method of magnetic induction is to be used for measuring the thickness of the coatings. This will allow coating wear to be correlated to blade pressure over time.

b. Doctoring Test Plan

Three data acquisition tasks will need to be performed in this study: recording of doctor blade loading data for each coating (an exact method is being developed), measuring of thickness changes in each coating, and IR imaging of the coatings while the doctor blade is in contact with the roll.

The test will be stopped when:

- A coating fails due to doctor blade loading
- The doctor blades wear to an unusable point

Doctor Blade Loading

Multiple doctor blade loading levels will be used. The blade loads will be: 87.6, 175.2, 262.8, and 350.4 N/m (0.5, 1.0, 1.5, and 2.0 pli). These loads are equivalent to the average loading range of granite press rolls. Continuous observation of the blade once it contacts the roll will be needed due to rapid blade wear during the first 30 min of contact. The blade will continue to decrease in load as the blade wears; therefore, the blade load will need to be checked on a regular basis to guarantee that proper loading is applied.

Higher blade loads will be used after the initial load range is completed. The higher loads will be on the order of 0.9 kN/m (5 pli) higher than the initial cases.

Coating Thickness Measurement

The measurement of coating thickness will be performed while the roll is in a static position. It has not been determined if the heat of the roll will be a factor in the thickness measurement. Thickness measurements would be made either on a daily basis or on a three-day basis, dependent on heat being a factor in the measurement. The measurements will be made at the same positions on the coatings and will be made at multiple locations in the CD.

IR Thermography

Infrared thermograms of the entire roll surface and the individual roll coatings will be recorded dynamically. A procedure similar to the stage 1 thermography will be utilized. infrared data will be taken at least once a day. The objective is to correlate wear patterns with thermal data.

c. Sheet Feeding

It has been proposed that after the wear study is performed, linerboard made on the Formette Dynamique will be impulse dried using the test coatings. The sheets may be uniform and nonuniform (wad simulation) in density and caliper.

By feeding sheets through the press nip, more informative data may be determined from the coatings:

- Release properties of the coatings.
- Shock-loading (wads) results.
- Ability of sheets to be properly doctored from coatings if sticking occurs.

This stage of the test is still in conception and a test plan has not been drawn up.

3.) Scanning Electron Microscope (SEM) Analysis of Coating Defects:

Extremely small defects were found in the roll coatings upon observation with a magnifying glass (30X). The defects could best be described as "divots" in the coating surface. All the coatings have been found to have at least one of these surface divots. The divots are undetectable by the IR scanner due to the small size. The divots were documented using acetyl-cellulose tape which adheres to the surface and is set by a Formvar, 3% in ethylene dichloride, solution.

The acetyl-cellulose tape was gold-sputtered coated and then viewed under the SEM. The average diameters were calculated for each divot:

Replication ID#	Coating	Diameter (μm)
17	Beloit "AZ"	375
21 (duplicate of 17)	Beloit "AZ"	375
18	Beloit "E"	580
15	Beloit "A"	580

It is believed these divots are small chips that have been removed from the coating. The divots were found approximately four months into stage 1 of the test. The divots do not have a general pattern on the coatings. The only obvious pattern is on the Beloit A coating. The pattern is a concentration of divots in a 20-mm (0.79 inch) circumferential bandwidth. A portion of felt type 1 that had exposed base fibers ran against the coating surface. This could have caused high localized stresses in the coating at these locations due to the base fibers contacting the surface (base fibers are thicker and harder than the batting fibers). The Beloit "E" coating only had one divot.

The tape replications were made also to document the coating surfaces at this point in the test. A comparison with the original micrographs made from the replication process at Beloit showed the current surface with much more contamination than was originally present. It is believed that the small particles that are found on the surfaces are deposits

and dirt (from the water and the felt). The coatings were cleaned prior to replication, but a thin-film residue was left on the surfaces, especially the Beloit "A" coating.

Due to the small thickness of the replicating tape (0.034 mm), the depth of the divots could not be determined. Future plans are to replicate the coatings with a silicon-based paste that may be strong enough to be removed from the interior of the divots. The depth of the divots may then be calculated using the laser confocal microscope.

H. X4 Wet Pressing Results From January 1997 Start-up

1.) Introduction:

Before running the impulse drying trial on the Beloit X4 pilot machine, in March, it was necessary to check out the induction heater and demonstrate that linerboard could be made on the pilot machine. A January pre-trial experiment was scheduled to answer these questions. The results of that experiment are described in this section.

Objective: Try to make 205 gsm linerboard rolls using only wet pressing.

Conditions: Repulped roll stock at ~670 ml CSF,
10-inch shoe in ENP, speed 1250 fpm,
Post nip option 1: single felt, (roll wrap option 1)
Sample felt: CSX

2.) Procedures:

On January 15, 1997, paper was successfully reeled at the dry end, and the basis weight was brought to ~205 gsm. The measured reel moisture was about 13%. A sample was obtained from the reel and the CD grammage variability was measured at Beloit. The overall average was 192.40 gsm, with a standard deviation of 5.72 gsm.

The press section has a bi-nip roll press followed by an ENP press. The ENP roll had a cover of Beloit "E" material. Table H1 lists some of the press parameters.

Table H1. Press parameters. Solids determined from grab samples.

Position	Press Loadings	Web Solids
Exiting ENP	400, 600, 6000 pli	48%
Exiting ENP	400, 600, 6000 pli	50%

Physical property tests were also performed at Beloit and are tabulated in Table H2.

Table H2. Sheet properties from reel samples.

Test	Result
Grammage	209.2 gsm
Caliper	345.8 μm
Apparent Density	0.605 g/cm^3

On January 20, 1997, a roll of 205 gsm paper was produced. This roll was sent to IPST for future testing. The same press loadings were used, except as noted. Listed in Table H3 are some of the machine parameters.

Table H3. Wet end machine parameters. Solids determined by grab samples.

Position	Press Loadings	Web Solids
Exiting ENP	400, 600, 6000 pli	48.5%
Exiting ENP	400, 600, 6000 pli	47.8%
Wire	n/a	25.5%

On the following day, January 21, 1997, the ENP roll was heated to 325°F and an attempt was made to thread a paper web through the press section. The paper stuck to the roll before the web could be broken back to the former. Attempts to clean the roll failed and it was decided to cool the roll down to facilitate cleaning. After cleaning the

paper off of the roll, two areas of cover failure were noticed, as described in the next section.

I. Preliminary Analysis of the January 1997 Roll Cover Failure

1.) Events leading up to the roll cover failure:

a.) DAY 1-4 (January 14-20, 1997)

Start-up after major rebuild

- Resolve mechanical issues
- Set process parameters to run board

The plan was to start at 100 gsm basis weight and increase up to 200. However, machine operating problems prevented threading of the dryers. The problems were corrected overnight. There were problems threading the dryers. Since draw and steam pressures needed to be adjusted. Paper was eventually brought to the reel and a roll started. By the end of the second day, 205 gsm paper was made and reeled. Reel moisture was about 13%.

Part of the third day's objectives was to start at 200 gsm and thread at that weight. After an attempt to thread 200 gsm with ensuing difficulties, it was decided to cut back to 150 gsm for threading. While trying to bring the basis weight up to 200 gsm, one of the boilers lost gas pressure and shut down. We think that high demand that day dropped the main line pressure (it was a bitterly cold day).

On the fourth day we made a 205 gsm roll of wet pressed paper. We also took web samples to determine ingoing and outgoing solids.

b.) DAY 5 (January 21, 1997)

Objective: Try to make 205 gsm linerboard rolls using the steambox and impulse dryer.

Conditions: Repulped roll stock at ~670 ml CSF, Impulse drying with CSX felt, 10-inch shoe in ENP, speed 1250 fpm.

Started by heating the ENP roll to 325°F. Once the roll stabilized, a 130-gsm web was treaded to the press section. On the first attempt, some paper stuck to the roll and wrapped around the roll while some paper was observed going down the sample felt. When the paper hit the nip, the IR temperature indicator dropped from ~314°F to ~240°F (visual observation). The contact thermocouple readings dropped no lower than about 300°F.

After the roll temperature dropped and started to recover to about 260°F (IR), protection interlocks tripped, shutting down the heater. The heater was raised and the roll allowed to cool to help facilitate cleaning of the roll. Protection interlocks were cleared. As the roll cooled two areas of the cover failure were discovered. The reasons for the cover failure are not known at this time.

There are a number of procedural changes, listed below, that should help reduce the potential for cover failure during the next impulse drying trial.

- Run the impulse dryer with a wet felt for a least a day prior to drying paper. This will thermally cycle the cover to relieve residual stresses and test the cover for thermal shock resistance.
- Add a felt shower that can be turned on and off from the control panel. This would simulate feeding a web and producing a thermal shock. By controlling the water flow, different conditions can be simulated and the heater controls adjusted to compensate for the temperature drop.
- Switch to felt wrap option 2. With this option, there is no need to stick the paper to the roll for threading and the roll temperature can be raised well above the sticking range.
- Start with the roll temperature well above the sticking range. If there are threading problems, then the temperature can be gradually lowered.
- Station people to observe each part of the press during threading and continuously record controller data. This will not reduce any problems, but will give us a more complete data set if a problem occurs.

2.) Immediate examination of the roll:

First, some additional observations from the trial date (1/21/97). The doctor blades were changed that morning so that new blades were used when the roll was heated. Also, the web may have folded over during threading. Normal water is used on the X4 machine (hard water). Although the doctor blades seem to do a good job of scraping the calcium

off of the roll, there may have been enough between the nip and the doctor to influence sticking. Beloit has already initiated steps to get conditioned water to the press felt showers.

The HTP roll was removed from the machine and placed on blocks for examination on Thursday, January 23. Two large areas of the coating came off of the roll at about the same angular location. Both patches were about 4 inches by 8 inches, with the longer dimension around the roll. There are two areas, of about the same size, where the is blistered. Pieces of ceramic started to fall off of these areas during the roll removal process. In the areas where the coating failed, the pieces of coating came off as small tiles with relatively square edges. The remaining cover in the failed areas was relatively smooth, indicating that the failure occurred at a specific plane within the coating.

The whole surface of the roll cover appears to be covered with microcracks, although it is difficult to see them at the roll edges except for the dubs (calcium deposits highlight the dub cracks). For most of the roll, the microcracks appear to be randomly shaped with a 'tile' size of about 1/8-inch by 1/8-inch. However, in the area where the failures occurred, the tiles form a rectangular grid and are much larger, typically about 3/16-inch by 3/8-inch. The larger tiles cover a CD band that extends about 14 inches around the circumference. All of the tiles within the band were of the larger size, with a small transition area (about 1 inch) to the smaller size covering the rest of the roll.

The leading edges of the two blistered regions have a much wider CD crack. These cracks appear to have paper imbedded in them and may have been the starting points for the blisters. As the large cracks formed, the tiles would be displaced, causing the coating to raise into a blister.

The roll surface that saw paper is covered with a light brown film (probably lignin). There are two MD bands, corresponding with the cover failures, that have a much darker film. There are also two CD bands of stuck paper fibers. The first band trails the failure zone by about 24 inches and is about 3-inches wide. The second band trails the first by about 9 inches, has fewer stuck fibers, and is also about 3-inches wide.

The doctor blades showed obvious damage when removed. The first blade had two areas, corresponding to the cover failures, which had extensive abrasion damage. The second blade had much less damage and had paper stuck to the leading edge. Several wads of creped paper were recovered from the save-all pan behind the second doctor blade. A couple of these wads had pieces of coating in them and several loose pieces of coating were also recovered. One of the wads was glazed on one side and may have been rubbed against the hot roll by the doctor blade. This may be the cause of the MD dark bands on the roll.

Although the reason for the coating failure is not known at this time the following information was obtained.

- A 14-inch CD band of the roll probably had a different history than the rest of the roll, causing it to microcrack in a different pattern. Either the roll was processed differently in that area or it saw a different thermal history, or both.
- Larger microcrack domains (tiles) seem to be more susceptible to damage than smaller domains.
- Paper sticking must be eliminated or at least reduced.

Before deciding on a replacement roll cover, Beloit and IPST will do numerous experiments to attempt to duplicate the coating failure and to test alternative coatings.

- Beloit will run thermal cycling MTS tests on platens with different coatings to try to produce microcracks.
- Beloit will install an "G" covered roll into the HRP and thermally cycle it to determine its durability.
- Beloit will run MTS sticking tests with "E," "F," and "G" using linerboard samples.
- IPST will perform coupon shear tests with coatings "E", "F" and "G".
- IPST will do a literature search on plasma sprayed coating durability and failures.
- IPST will continue doctoring experiments on the durability test stand.
- IPST will try to calculate the stresses produced in the cover coating during doctoring.

After these experiments are complete, a decision on which coating should be deposited onto the HTP roll will be made. At least, the direction of the neccessary design change will be known. The goal of this work is to have a roll coating on the HTP roll ready for IPST's virgin furnish trial on the HTP trials the weeks of the 7th and 14th of July 1997.

As it is desirable to continue to explore the reasons for the failure of the "E" coating, the remainder of the January start-up experiments will be attempted with a new "E" coated roll in March of 1997.

J. Literature Review Of Plasma Sprayed Coating Failure Mechanisms:

The following brief literature survey was undertaken by IPST after the coating failure. The review serves the purpose of bringing out factors that might not be otherwise considered.

1.) General Reviews of Thermal Barrier Coatings:

Thermal barrier coatings consist of a ceramic insulating layer applied over an intermediate metallic bond coat layer [J1]. Both are applied by plasma spraying. The properties and service life of these coatings depends on factors such as plasma spraying parameters, powder quality, bond coat and substrate chemistry, ceramic coating composition, microstructure, and layer thicknesses as well as the thermal and chemical environment in which the coating will be used.

The three components of the coating each have different requirements. Thermal expansion of the substrate dictates the thermal expansion of the ceramic. The bond coat performs three functions. It needs to provide stress-relief, oxidation resistance, and a "key" for firm mechanical adhesion of the ceramic coating.

The ceramic material must be refractory, chemically inert, possess good mechanical strength and thermal shock resistance, have good wear and erosion resistance, be phase stable and possess low thermal conductivity, and have a thermal expansion coefficient similar to that of the substrate.

With regard to failure mechanisms and life modeling, Miller [J2] notes that prolonged exposure to a high-temperature oxidizing environment may lead to coating failure. The stresses leading to failure may result from thermal expansion mismatch between the ceramic and metallic layers and be strongly influenced by bond coat oxidation. Other factors including possible ceramic sintering and bond coat inelasticity may also play a role in coating failure. The actual failure is generally within the ceramic layer near the bond coat layer. Failure is believed to be the result of slow crack growth and microcrack link-up within the ceramic.

The thickness of thermal barrier coatings is typically in the range of 0.004 to 0.024 inches. Before the bond coat is applied, the substrate is typically roughened by grit blasting with aluminum oxide to increase the adherence of the bond coat to the substrate.

Thermal barrier coatings are generally observed to fail by spalling within the ceramic layer at a location near the irregular ceramic/bond coat interface [J3]. Spalling is characteristic of "compressive failure," i.e., failure which occurs when the ceramic has been placed in biaxial compression parallel to the interface and tension perpendicular to this interface. The fact that coatings show a greater tendency to fail in compression than in tension contrasts with the conventional view of monolithic ceramics. Monolithic ceramics may break under tension. Coatings will crack perpendicular to the interface, but such cracks may even be beneficial because they may serve to arrest cracking parallel to the interface. The stresses leading to compressive failure can arise during rapid heating or after cooling. Stresses are encountered on rapid heating because of the temperature gradients which develop throughout the thickness of the coating. Stresses are encountered after cooling because of thermal expansion mismatch between the ceramic and the metallic layers. These cooling stresses may increase as the "stress-free temperature" of the

ceramic/metallic system increases by any of several possible high-temperature stress relaxation processes. Cooling mode compressive stresses tend to maximize near the interface, where failure is observed. It should be noted that unlike most other applications, the impulse drying roll is not heated on the outer surface of the coating, but inductively in the metallic substrate beneath both the outer coating layer and the metallic bond coat.

If delaminated specimens are cycled in a furnace, the heat flux is too low to cause spalling of the ceramic. Rather, tensile cracks perpendicular to the interface develop in the delaminated region. These tensile cracks must result from the increased circumference of the material above the gap in the ceramic layer as it expands. This could suggests that the perpendicular cracks in the impulse drying roll happened after the coating had already delaminated.

Thermal barrier coatings may either be duplex coatings or three-layer coatings. The duplex coating consists of a metallic bond coat over a metallic substrate and a ceramic layer deposited onto the bond coat. The three-layer coating adds an additional metallic or mixed ceramic-metallic layer between the bond coat and the ceramic. The advantage of the three-layer coating is that it provides enhanced accommodation of thermal expansion mismatch effects between the ceramic and the bond coat [J4].

Degradation mechanisms for thermal barrier coatings on gas-turbine blades are generally agreed to be the consequence of the propagation of cracks parallel to, or coincident with, the ceramic-bond coat interface. The primary cause of this failure is stress-related, particularly to the stresses induced by thermal expansion mismatch between the ceramic and metallic layers with the stresses being markedly influenced by temperature-time

processes such as bond coat oxidation. Stresses induced by thermal expansion mismatch appear most consistent with the failure location, but the stress will be tensile in the coating, but compressive in the substrate. Work on the tensile and fatigue testing of the ceramic coatings shows that it is difficult to cause coating spallation due to tensile stresses if the coating is thin, but in contrast, compressive stresses in the plane of the coating can readily cause spallation and failure.

2.) Failure Modes:

In a study by Diaz [J5], coatings having a continuous bond coat remained attached to the substrate after thermal treatment. In contrast, coatings having a discontinuous bond coat of nonuniform thickness failed. It was argued that the nonuniform bond coat thickness could have added extra residual stress on the ceramic coating during thermal treatment. As spallation occurred after the specimens were raised to 700°C, in both inert gas (argon) and oxidizing (air) environment, bond coat oxidation could be excluded as a contributing factor.

Kokini, et al., [J6], examined the mechanism of stress relaxation and its impact on thermal barrier cracking. They postulated that when the ceramic surface of a thermal barrier coating is subjected to a large heat flux, a compressive in-plane stress is developed owing to the large surface temperature. They stated that after 2 hours of steady state heating, this compressive stress relaxes (i.e. becomes smaller). Thus, upon uniform cooling to room temperature, the stress on the ceramic surface becomes tensile and leads to initiation of surface cracks.

They express the stress relaxation behavior of a material through the strain rate ε_c,

$$\varepsilon_c = A\sigma^n \exp\{-\Delta H/RT\}$$

Where,

σ	=	Von Mises equivalent stress
ΔH	=	Activation energy
R	=	Universal gas constant
A, n	=	Constants

For the impulse drying press roll, the roll cover will experience high frequency thermal cycling where the time between the end of the heating part of the cycle and the start of the cooling part of the cycle is measured in fractions of a second. As stress relaxation is generally a slow process, it is reasonable to assume that it does not contribute to the problem encountered in the January 1997 experiment.

While thermal stresses arising from the mismatch of thermal expansion coefficient often is the cause of coating failures, Levit, et al., [J7], note that another source of internal stresses is residual stresses. These arise from the plasma spraying process and are associated with the rapid cooling of molten or partially molten droplets, impacting on the cool substrate. They suggest that controlling the substrate temperature during deposition can influence the sign and magnitude of these stresses. They further note that, under the right conditions, the presence of compressive residual stresses may have the beneficial effect of

reducing the magnitude of detrimental thermal stresses and prolong the service life of the coating.

They report on the measurement of and prediction of residual stresses in thermal barrier coatings. They found that the substrate temperature, maintained during deposition of the coating, strongly affects the residual stress distribution in the finished ceramic coating. Their experimental and theoretical work shows that the residual stress on the surface of the resulting ceramic coating was a linear function of the temperature at which the substrate was maintained during coating deposition. The residual stress at the outer surface of the ceramic was most positive (in tension) at a low substrate deposition temperature of 75°C and was most negative (in compression) at high substrate temperature of 500°C. The residual stresses within the ceramic coating are not uniformly distributed throughout the thickness, but gradually change, with a tendency to the compressive state toward the substrate. Thus the ceramic near the interface with the substrate was found to be the most compressed.

Multiple cracks that are perpendicular to the ceramic-bond coat interface are called "segmented." They are formed in regions where high residual tensile stresses are present. Microcracks that are parallel to the coating-substrate interface are found in regions of the coating where there are residual compressive stresses. These microcracks may be linked to pores and to poorly bonded intersplat regions, and may provide a pathway allowing parallel interfacial cracks to grow and relax the residual stresses in the coating.

Levit [J7] notes that it is commonly assumed that compressive stresses are desirable in the deposited top layer, since they prevent the formation and propagation of cracks. Such a state of stress in the ceramic coating used by Levit occurred when the temperature of

the substrate during deposition was higher than 400°C. However, microcracking parallel to the interface may appear in the region of high-compressive stresses near the ceramic - substrate interface and these can lead to separation (spalling) of the deposited layer. In any case, Levit found that a "stress-free" coating was produced when his coating was applied at a substrate temperature of 400°C.

During the January 1997 experiment, we observed both segmentation and spalling. The work of Levit suggests that we can reduce the likelihood of spalling by reducing the substrate temperature during the coating application. This, however, may also result in more segmentation. Hence, one should prudently consider alternate coating materials and coating thicknesses.

Functionally graded coatings can sustain multiple cracking upon thermal and mechanical loading. Bao, et al. [J8] have found that their fracture behavior can be characterized by the local volume fraction of metal in the coating. Compared with pure ceramic coatings, grading of a coating can significantly reduce its crack driving force. It was found that under mechanical loading, the effect of gradation on the crack driving force, was relatively small. However, under thermal loading, the influence of coating gradation can be significant. This suggests that a press roll operating at low uniform temperature in a wet press would not require a graded coating. However, a roll coating that experiences thermal loading as well as mechanical loading, such as an impulse drying press roll, should be graded.

Following Bao [J8], we consider a series of multiple cracks that are perpendicular to the plane of the substrate and are separated by a distance of **2L**. These cracks start at the outer surface of the coating and have a depth into the coating of **a**. The coating is assumed to have a thickness of **h**.

The normalized energy release rate is defined as, $\zeta \bar{E}_m / \sigma^2 h$

Where,

ζ = energy release rate

$\bar{E}_m = E_m/(1-\nu_m^2)$ = Young's modulus of metal phase

σ = average stress

ν_m = Poisson's ratio of metal phase

Bao found that the normalized energy release rate was a function of the volume fraction of metal phase in the coating, the normalized crack length, a/h, and the normalized crack spacing, L/h.

For low normalized crack lengths (a/h << 1), the normalized energy release rates for ceramic and graded ceramic coatings were about the same. However, for deeper cracks (a/h~1) the graded-ceramics were found to have significantly lower normalized energy release rates as compared to the pure ceramics. We note that the coating that failed in the January experiment exhibited two types of cracks. There were microcracks over all of the roll surface. These randomly shaped cracks were about 0.06 inches apart. However, in the region where the coating failure occurred, the cracks were 0.09 inches apart in one direction and 0.19 inches apart in the other direction and had a depth of about 0.041

inches. We note that the January 1997 ceramic coating had a thickness of 0.048 inches. Hence, in the region of the failure, the normalized crack length was a/h = 0.85 and the normalized crack spacing, L/h, was 1.88 in one direction and 3.96 in the other.

Bao found that for a given normalized crack length, the energy release rate increased with an increase in the normalized crack spacing. We infer from this that the farther apart the cracks, the faster they propagate and the more likely they are to be involved in the failure.

Consider a thin ceramic coating on a thick metal substrate, under plane strain conditions. Bao found that the residual stress, σ_T, due to thermal expansion mismatch is given by,

$$\sigma_T = \frac{(\alpha_m - \alpha_c)(T - T_o)E_c}{(1 - \nu_c^2)}$$

where T is the current temperature and T_0 is the "stress-free" temperature (the temperature of the substrate during coating). Since the thermal expansion coefficient of the ceramic α_c is usually lower than that of the metal, α_m, the residual stress is compressive when $T < T_0$.

For a thin functionally graded ceramic/metal coating on a thick metal substrate, Bao found that the residual stress in the coating is given by,

$$\sigma_T(x) = \frac{[\alpha_m - \alpha(x)](T - T_0)E(x)}{1 - \nu^2(x)}$$

where $\alpha(x)$, $E(x)$ and $\nu(x)$ are the effective properties of the graded coating.

Bao assumed that the local volume fraction of metal in the ceramic coating, $g(x)$, obeyed a power law relation,

$$g(x) = g_0 + (1 - g_0)(x/h)^n$$

It was also assumed that at the coating - substrate interface, the volume fraction of metal is unity ($g(h) = 1$) and $\sigma_T(h) = 0$.

Hence, the residual stress decreases with x. This implied to Bao that under the same applied tensile load, the functionally graded coating might be more prone to cracking at temperatures below the "stress-free" temperature ($T < T_0$) compared with the pure ceramic coating. On the other hand, when $T > T_0$, the tensile thermal stresses in a functionally graded coating would be lower than in a pure ceramic coating, as would be the fracture driving force.

The cracking of a functionally graded coating under a combination of thermal load, σ_T, and mechanical load, $\sigma > 0$, was also considered by Bao. The total stress intensity factor, K, due to both thermal and mechanical loads, was shown to have the form,

$$\frac{K}{\sigma\sqrt{h}} = \left[\sqrt{\psi} + \frac{\sigma_T}{\sigma}\sqrt{\phi}\right]\sqrt{\frac{\overline{E(a)}}{\overline{E}_m}}$$

It was noted that when $\alpha_m > \alpha_c$ and $T < T_o$, $\frac{\sigma_T}{\sigma} < 0$.

Thus, for certain values of $\frac{\sigma_T}{\sigma}$, the total stress intensity factor, K, can become negative, which implies that crack growth in the functionally graded coating would be prohibited.

While much is known about the failure mechanisms of thermal barrier coatings, Bartlett [J9] reminds us that the state-of-the-art is still expanding. He states that coating lifetime is limited by its susceptibility to failure upon isothermal or cyclic heat treatment. That because of thermal expansion mismatch, the ceramic coating is under nominal biaxial compression after any kind of post-spray treatment. Thus, failure occurs by buckling and spalling of the coating, which in turn requires the existence of a flaw of critical size at the interface or near the interface region.

He notes that, typically, a bond coat of composition MCrAlY (where M can be Co, Ni, or Fe) is applied to the substrate prior to application of the ceramic top coat. This bond coat provides additional oxidation protection to the substrate and enhances adhesion of the ceramic. However, heat treatment of the samples in air can lead to the formation of a reaction product layer at the bond coat/top coat interface. Cracking and failure near the interface, which is a prerequisite for spalling, has been correlated with the presence of this layer [J28], though its effect is not well understood. For example, he notes that cracking has been observed to occur at the interface as well as in the ceramic coating in the vicinity of the interface. These failure modes are often referred to as "adhesive" and "cohesive" failures, respectively. However, Bartlett claims that there does not exist an understanding of the relationships between the various mechanical and thermal properties of the

constituents and these types of failure, nor have the sources of the stress generating the cracking been explicitly identified.

3.) Conclusions:

We conclude from this brief literature review that the following are important design considerations:

- Expected operating temperature range of the various layers of the coating as well as the temperature of the substrate during plasma spraying.
- Temperature dependence of the thermal and mechanical properties of the various layers of the coating.
- Thickness of the various layers of the coating.
- Metal grading function for the ceramic layer.
- Oxidation resistance of the bond coat.

A number of additional recent publications have been found that will, at a later date, be included in the survey. We include these [J11-J27] in the list of references.

The factors that come out of the literature survey will be brought into the decision regarding the choice of a replacement coating for the planned July 1997 pilot paper machine experiments.

References

A1. Crouse, J. W., Sprague, C. H., and Woo, Y. D., "Delamination - Stumbling Block To Implementing Impulse Drying Technology For Linerboard," Tappi J. 72, No. 10: 211-215 (Oct. 1989).

A2. Burkhead, J. R., Burns, J. R., Lindsay, J. D., and Orloff, D. I., "Effect Of Felt Saturation On Delamination In Impulse Drying," Tappi Eng. Conf. (Atlanta) Proc. (Book 1): 367-375 (Sept. 11-14, 1989).

A3. Back, E. L., "Press Drying/Impulse Drying - Limited Possibilities," Svensk Papperstid. 93, No. 7: 131-132, 134, 136, 138 (April 26, 1990).

A4. Back, E. L., "Hot-Pressing," Przegl. Papier. 47, No. 3: 103-110 (March 1991).

A5. Back, E. L., "Why Is Press Drying/Impulse Drying Delayed?," World Pulp Pap. Technol. 1992: 153-156 (1992).

A6. Stenstrom, S., "Drying and Energy," Eucepa 24th Conf. Proc. (Stockholm), Pap. Technol.: 220-235 (May 8-11, 1990).

A7. Stenstrom, S., "Delamination in Impulse Drying: Some Comments to Improve Dryer Design," Tappi J. 73, No. 9: 259-260 (Sept. 1990).

A8. Pulkowski, J. H. et al., "Heated Extended Nip Press with Porous Roll Layers," U.S. Patent No. 4,874,469, Filed August 27, 1987.

A9. Kloth, G. R., Orloff, D. I., and Rudemiller, G. R., "Method and Apparatus for Drying Web," U.S. Pat. 5,101,574. Issued April 7, 1992. Filed: U.S. Appln. 417,261 (Oct. 15, 1989).

A10. Lenling, W. J, and Orloff, D. I., "Method and Apparatus for Drying Web," U.S. Pat. 5,272,821. Issued December 28, 1993. Filed: U.S. Appln. 643,524 (January 18, 1991). Priority: U.S. Appln. 417,261 (October 15, 1989). U.S. Pat. 5,101,574. [Engl.] Cf. U.S. Pat. 5,101,574.

A11. Orloff, D. I., "Method and Apparatus for Drying Web," U.S. Pat. 5,353,521. Issued October 11, 1994. Filed: U.S. Appln. 758,775 (September 12, 1991). Priority: U.S. Appln. 417,261 (October 15,1989). U.S. Pat. 5,101,574. [Engl.] Cf. U.S. Pat. 5,101,574.

A12. Orloff, D.I., "Impulse Drying Of Linerboard: Control Of Delamination," Journal Of Pulp And Paper Science, 18(1), J23-J32 (January 1992).

A13. Orloff, D.I., And Sobczynski, S.F., "Impulse Drying Pilot Press Demonstration: Ceramic Surfaces Inhibit Delamination," Paper Technology 34(10): 24-33 (December 1993).

A14. Orloff, D.I., and Lindsay, J.D, "The Influence of Yield, Refining and Ingoing Solids on the Impulse Drying Performance of a Ceramic Coated Press Roll," Proceedings of the Tappi Papermakers Conference, 85-93, Nashville, 1992.

A15. Orloff, D.I., "Impulse Drying of Recycled Multi-Ply Linerboard: Laboratory-Scale Studies", Tappi J. 77(2):169-179 (February 1994).

A16. Boerner, J., and Orloff, D.I., "The Effect of Basis Weight and Freeness on Sheet Permeability and Critical Impulse Drying Temperature", Tappi J. 77(2):163-168 (February 1994).

A17. Orloff, D. I., and Phelan, P. M., "Heat Transfer During Impulse Drying; Influence of Press Impulse and Pressure Profile," Heat and Mass Transfer in Pulp and Paper Processing (Seyed-Yagoobi, J., and Anderson, D. W., Ed.): 17-23 (1993; American Society Of Mechanical Engineers).

A18. Orloff, D.I., Phelan, P.M., and Crouse, J.W., "Linerboard Drying on a Sheet-Fed Pilot Impulse Drying Shoe Press," Tappi J. 78(1):129-141 (January 1995).

A19. Phelan, P.M., Kerschner, C.M., and Orloff, D.I., "The Effect of Thermal Mass and Peak Pressure on Impulse Drying Energy Transfer," Tappi J. 79(11):131-137 (November 1996).

A20. Miller, R. R., " Multipulse Units Boost Drying Rate, Reduce Sheet Delamination Problems," Pulp Pap. 65(5): 145-149 (May 1991).

A21. Crouse, J. W., "Heavy-Weight High-Temperature Pressing Apparatus," U.S. Patent No. 5,439,559, Filed February 14, 1994.

A22. Babinsky, V. A., Mumford, W. G., "Chambered-Nip Drying of Paperboard Webs," U.S. Pat. 5,404,654. Issued April 11, 1995. (Filed U.S. Appln. 52,981 (April 27, 1993).

A23. Orloff, D.I., "Commercialization of Impulse Drying," 1994 IPST Executives' Conference Proceedings, 23-25, (May 11-12, 1994).

A24. Orloff, D.I., et al., "Method and Apparatus for Drying a Fiber Web at Elevated Ambient Pressures," U.S. Patent Number 5,598,642, (Issued February 4, 1997).

A25. Orloff, D.I., et al., "Method and Apparatus for Drying a Fiber Web at Elevated Ambient Pressures," U.S. Patent Application Serial No. 08/618,294, (Filed March 18, 1996.)

D1. Lindsay, J. D., "Anisotropic Permeability of Paper: Theory, Measurements, And Analytical Tools," IPC Technical Paper Series #298, (1988).

D2. Lindsay , J. D., and Brady, P. H., "Studies of Anisotropic Permeability with Applications to Water Removal in Fibrous Beds," IPST Technical Paper Series #417, (1992).

D3. Lenling, W. J., Smith, M. F., and Orloff, D. I., "Thermal Coating Development for Impulse Drying," Jour. Of Thermal Spray Technology, 2(2):173-178,(1993).

D4. Orloff, D. I., "Impulse Drying of Linerboard: Control of Delamination,"

Proceedings: 77th Annual Meeting: Technical Section of the Canadian Pulp and Paper Association, January 31 and February 1, 1991, B9-B25.

D5. Bloom, F., Hojjatie, B., and Orloff, D. I., "Analysis of a Crown-Compensated Impulse Drying Press Roll : The Lubrication Problem," Tappi J. 79(9):164-173, (1996).

D6. Orloff, D. I., Patterson, T., et al., "Opening the Operating Window of Impulse Drying," A Project Report to the Member Companies of The Institute of Paper Science and Technology, Project F0001, Report 13, September 1996.

D7. Dey, S. K., "Numerical Solution of Nonlinear Implicit Finite Difference Equations of Flow Problems by Perturbed Functional Iterations," In W. Kollman (Ed.), Computational Fluid Dynamics, 543-602, Hemisphere, Washington, D. C., 1980.

D8. Dey, S. K., "Perturbed Iterative Solution of Nonlinear Equations with Applications to Fluid Dynamics," J. Comp. and Appl. Mathematics, 3(1):15-30, (1977).

D9. Dey, S. K., "Numerical Studies of a Perturbed Iterative Scheme with Applications to Coupled Nonlinear Systems of Equations," Argonne National Lab., Appl. Phys. Div., Anl/Fpp/Tm-96, September 1977.

D10. Dey, S. K., "Perturbed Iterative Solution of Coupled Nonlinear Systems with Applications to Fluid Dynamics," J. Comp. And Appl. Mathematics, 4(2):117-128, (1978).

E1. Szicla, Z. and Paulapuro, H., "Changes in Z-Direction Density Distribution of Paper in Wet Pressing, " J. Of Pulp And Paper Sci.: 15(1):J11-J17 (January 1989).

E2. Zavaglia, J.C. and Lindsay, J.D., "Flash X-Ray Visualization of Multiphase Flow During Impulse Drying," Tappi J., September, 1989, 79-85.

E3. Burns, J.R., "An Investigation of Z-Direction Density Profile Development During Wet Pressing," Ph.D.Thesis, Institute Of Paper Science And Technology, April 1992.

E4. Burns, J.R., Conners, T.E., and Lindsay, J.D., "Dynamic Measurement of Density-Gradient Development During Wet Pressing," Tappi J., 73(4):107-113(1990).

E5. Burton, S.W., "An Investigation of Z-Direction Density Profile Development During Impulse Drying," Ph.D. Thesis, Institute of Paper Chemistry, January 1987.

E6. Chang, N.L., "Dynamic Compression of Handsheets," Proc. Tappi Eng. Conf., 1978, 93-106.

E7. Devlin, C.P., "An Investigation of the Mechanism of High-Intensity Paper Drying," Ph.D. Thesis, Institute of Paper Chemistry, June 1986.

E8. Budinski, K., "Engineering Materials: Properties and Selection," 2nd Edition.

F1. Orloff, D. I., "Impulse Drying of Linerboard: Control of Delamination," 77th Ann. Meet. Can. Pulp and Paper Assoc., Montreal, Canada, January 1991.

F2. Orloff, D. I., and Sobczyniski, S. F., "Impulse Drying Pilot Press Demonstration: Ceramic Surfaces Inhibit Delamination," Presented at SPCI-92, Bologna, Italy, May 19-20, 1992.

F3. Lenling, W. J., Smith, M. F., and Orloff, D. I., "Thermal Coating Development for Impulse Drying," Journal Of Thermal Spray Technology, 1993, 173-178.

F4. Young, H.T., and Chou,T. L., "Investigation of Edge Effect from the Chip-Back Temperature Using IR Thermograhpic Techniques," Journal Of Materials Processing Technology, 1995, 213-224.

F5. Connolly, M. P., "A Review of Factors Influencing Defect Detection in Infrared Thermography: Applications to Coated Materials," Journal of Nondestructive Evaluation, 1991, 89-96.

F6. Ogura, K., and Sakagami, T., "A New Inspection Technique for Small Flaws and Defects Using Infrared Thermography," ASME, Advances In Electronic Packaging, 1992, 909-915.

F7. McKnight , M. E., and Martin, J. W., "Detection and Quantitative Characterization of Blistering and Corrosion of Coatings on Steel Using Infrared Thermography," Journal Of Coatings Technology, 1989, 57-62.

F8. Satonaka, S., Ohba, H., and Shinozaki, K., "Nondestructive Evaluation of Weld Defects by Infrared Thermography," Proc. of the 14th Intl. Conf. on Offshore Mechanics and Artic Engineering-ASME, 1995, Vol. 3, 305-312.

F9. Lahdeniemi, M., Ekholm, A., and Santamaki, O., "IR Frequency Analysis In Paper Industry," Proc. Of SPIE, Thermosense XVIII, 1996, 2-4.

F10. Thermovision 900 Series User's Manual, AGEMA Infrared Systems, Danderyd, Sweden, 1993.

F11. Incropera, F. P., and Dewitt, D. P., Fundamentals of Heat and Mass Transfer, 3rd Edition, John Wiley & Sons, 1990.

G1. Renner, G., "Troubleshooting the Yankee dryer: Temperature Variations Caused by Condensate," TAPPI J., June 1989, 119-122.

J1. Taylor, R. and Brandon, J. R., "Microstructure, Composition and Property Relationships of Plasma-Sprayed Thermal Barrier Coatings,"Surface and Coating Technology, 50 (1992) 141-149.

J2. Miller, R., "Current Status of Thermal Barrier Coatings - an Overview," Surface and Coating Technology, 30 (1987) 1-11.

J3. Liebert, C. H., and Miller, R. A., "Ceramic Thermal Barrier Coatings," Industrial Engineering Chemistry Production Research And Development, 23 (1984) 344-349.

J4. Rhys-Jones T. N., and Toriz, F. C., "Thermal Barrier Coatings for Turbine Applications in Aero Engines," High Temperature Technology, 7(2) (1989) 73-81.

J5. Diaz, P., Edirisinghe, M. J., and Ralph, B., "Microstructural Changes and Phase Transformations in a Plasma-Sprayed Zirconium-Yttria-Titania Thermal Barrier Coating," Surface and Coating Technology, 82 (1996) 284 -290.

J6. Kokini, K., Takeuchi, Y. R., and Choules, B. D., "Surface Thermal Cracking of Thermal Barrier Coatings Owing to Stress Relaxation: Zirconia Vs. Mullite," Surface and Coating Technology, 82 (1996) 77 - 82.

J7. Levit, M., Grimberg, I., and Weiss, B. Z., "Residual Stresses in Ceramic Plasma-Sprayed Thermal Barrier Coatings: Measurement and Calculation," Materials Science and Engineering, A206 (1996) 30 - 38.

J8. Bao, G. and Wang, L., "Multiple Cracking in Functionally Graded Ceramic/Metal Coatings," International Journal of Structures, 32(19) 2853 - 2871(1995).

J9. Bartlett, A. H., and Maschio, R. D., "Failure Mechanisms of a Zirconia - 8 Wt% Yttria Thermal Barrier Coating," Journal of the American Ceramic Society," 78(4) 1018 - 1024 (1995).

J10. Kokini, K., and Takeuchi, Y. R., "Initiation of Surface Cracks in Multilayer Ceramic Thermal Barrier Coatings Under Thermal Loads," Materials Science and Engineering, A189 (1994) 301-309.

J11. Joshi, S. V., and Srivastava, M. P., "On the Thermal Cyling Life of Plasma - Sprayed Yttria - Stabilized Zirconia Coatings," Surface And Coatings Technology, 56 (1993) 215-224.

J12. Lee, J. D., Ra, H. Y., Hong, K. T., and Hur, S. K., "Analysis of Deposition Phenomena and Residual Stress in Plasma - Spray Coatings," Surface and Coatings Technology, 56 (1992) 27-37.

J13. Bordeaux, F., Moreau, C., and Saint Jaques, R. G., "Acoustic Emission Study of Failure Mechanisms in Tic Thermal Barrier Coatings," Surface And Coatings Technology, 54/55 (1992) 70-76.

J14. Harding, M., "Computer Simulation of Plasma - Sprayed Coatings I. Effective Bulk Properties and Thermal Stress Calculations," Surface and Coatings Technology, 48 (1991) 147-154.

J15. Wu, B. C., Chang, E., Chao, C. H., and Tsai, M. L., "The Oxide Pegging Spalling Mechanism and Spalling Modes of ZrO_2 8wt% Y_2O_3/Ni - 22Cr - 10Al - 1Y Thermal Barrier Coatings under Various Operating Conditions," Journal Of Materials Science, 25 (1990) 1112-1119.

J16. Berndt, C. C. "Instrumented Tensile Adhesion Tests on Plasma-Sprayed Thermal Barrier Coatings," Journal of Materials Engineering, 11(4):275-282 (1989).

J17. Gault, C., Boilevin, S., and Desplanches, G., "Elastic Properties of Ceramic and Ceramic-Metal Thermal Barrier Coatings," Conference Proceeding of the Institute of Ceramics, Stoke-At-Trent, UK, Science and Ceramics 14 (1988) 389-394.

J18. Suga, T., Kvernes, I., and Elssner, G., "Fracture Energy Measurements of Ceramic Thermal Barrier Coatings," Zeitschrift Fur Werkstofftechnik 15(11):371-377(1984).

J19. Case, M., and Kokini, K., "Thermally Induced Initiation of Interface Edge Cracks in Multilayer Ceramic Thermal Barrier Coatings," Ceramic Coatings - American Society Of Mechanical Engineers, Materials Division 44 (1993) 149-162.

J20. Erdogan, F., and Chen, Y. F., "Interfacial Cracking of FGM/Metal Bonds," Ceramic Coatings - American Society Of Mechanical Engineers, Materials Division 44 (1993) 29-37.

J21. Kokini, K., Takeuchi, Y. R., and Choules, B. D., "Thermal Crack Initiation Mechanisms on the Surface of Functionally Graded Ceramic Thermal Barrier Coatings," Ceramics International, 22 (1996) 397-401.

J22. Stecura, S., "Two-Layer Thermal Barrier Coatings I: Effects of Composition and Temperature on Oxidation Behavior and Failure," Thin Solid Films, 182 (1989) 121-139.

J23. Wu, B. C., and Chang, E., Thermal Cyclic Response of Yttria - Stabilized Zirconia/Conicraly Thermal Barrier Coatings," Thin Solid Films, 172 (1989) 185-196.

J24. Vandehaar, E., Molian, P. A., and Baldwin, M., "Laser Cladding of Thermal Barrier Coatings," Surface Engineering, 4(2) (1988) 159-172.

J25. Berndt, C. C., and Miller, R. A., "Failure Analysis of Plasma-Sprayed Thermal Barrier Coatings," Thin Solid Films, 119 (1984) 173-184.

J26. Choules, B. D., and Kokini, K., Proc. Symp. Ceramic Coatings, ASME Md, 44 (1993), 73 - 86.

J27. Kokini, K., and Choules, B. D., Composites Eng., Special Issue On Functionally Graded Composites, 1995, In Press.

VI. Appendix AA.

The Mathematical Formulation of the Model for Pore Expansion during the Impulse Drying of Paper

The first of the two equations for the i^{th} pore has the general form

$$\frac{d}{dt}\left(m_i(t)\frac{dh_i}{dt}\right)+k_i(t)h_i(t)=\mathcal{F}_i(t) \tag{A.1}$$

where $k_i(t)$ is the effective stiffness of the fibers, which are thought of as comprising the lateral surface of the i^{th} pore, $h_i(t)$, as defined below, represents the stretching of the fibers beyond their initial, equilibrium lengths $H_i(0)$, and $m_i(t)$ is the effective mass of those fibers. For $m_i(t)$ we have

$$m_i(t)=m_i^f+m_i^w(t) \tag{A.2}$$

where m_i^f is the effective mass of the (dry) fibers comprising the lateral surface of the i^{th} pore, while $m_i^w(t)$ is the mass of water contained in those fibers at time t. The function $k_i(t)$ represents the time-dependent effective stiffness that would be obtained by replacing all of the fibers forming the lateral surface of the pore by an elastic spring joining the upper and lower surfaces of the pore; it is time-dependent because it must depend not only on the effective stiffness of an individual dry fiber, say, k_D but, also on the mass $m_i^w(t)$ of water in the fibers comprising the lateral surface of the i^{th} pore; i.e.,

$$k_i(t) = \kappa(m_i^w(t), k_D) \tag{A.3}$$

Finally, in (A.1),

$$h_i(t) = H_i(t) - H_i(0) \tag{A.4}$$

where we assume that $H_i(0)$ is the (unstretched) equilibrium length of the fibers comprising the lateral surface of the i^{th} pore, and

$$\mathcal{F}_i(t) = \pi (R_i^2 - r_i^2) p_i(t) \tag{A.5}$$

is the force generated by the pressure field $p_i(t)$ which acts on the (effective) solid upper boundary of the i^{th} pore. Associated with (A.1) are the initial conditions

$$h_i(0) = 0, \ \dot{h}_i(0) = 0. \tag{A.6}$$

Remark: Because of (A.2) and (A.3), the coefficients of $h_i(t)$ and its derivatives on the left-hand side of (A.1) will depend not only on $p_i(t)$ but on $p_{i-1}(t)$ and $p_{i+1}(t)$ as well. This is because the computation of $m_i^w(t)$, as we shall see below, is influenced by the venting of water vapor into and out of the i^{th} pore.

Remark: The 'swelling' of the sheet, at time t, will be determined, once $H_i(t)$ for $i = 1,\ldots,n$, has been computed, by

$$\delta(t) = \sum_{i=1}^{n} h_i(t). \tag{A.7}$$

We now proceed with the derivation of the second model equation which mediates the evolution of $p_i(t)$ and $H_i(t)$, $t > 0$, $i = 1,\ldots,n$. We let

$m_i^g(t) \equiv$ mass of gas (water vapor) in the i^{th} pore at time $t \geq 0$ (A.8)

and

$\left(\frac{dm_i^g}{dt}\right)^V \equiv$ rate of change of the mass of gas (water vapor) in the i^{th} pore, at time t, due to vaporization of water in the fibers comprising the lateral surface of that pore. (A.9)

Also,

$\left(\frac{dm_i^g}{dt}\right)^O \equiv$ rate of change of the mass of gas (water vapor) in the i^{th} pore, at time t, due to the venting of gas out of that pore (A.10)

while

$\left(\frac{dm_i^g}{dt}\right)^I \equiv$ rate of change of the mass of gas (water vapor) in the i^{th} pore, at time t, due to the venting of gas into that pore. (A.11)

Then,

$$\frac{dm_i^g}{dt} = \left(\frac{dm_i^g}{dt}\right)^V + \left(\frac{dm_i^g}{dt}\right)^O + \left(\frac{dm_i^g}{dt}\right)^I \quad (A.12)$$

where, as a consequence of Darcy's law, it will follow that for each $i = 1,\ldots,n$

$$\left(\frac{dm_i^g}{dt}\right)^{O} < 0. \tag{A.13}$$

Also, for $i = 1,\ldots,n-1$

$$\left(\frac{dm_i^g}{dt}\right)^{I} = -\left(\frac{dm_i^g}{dt}\right)^{O} > 0 \tag{A.14}$$

while

$$\left(\frac{dm_n^g}{dt}\right)^{I} = 0. \tag{A.15}$$

Thus, an alternative form for (A.12) is

$$\frac{dm_i^g}{dt} = \left(\frac{dm_i^g}{dt}\right)^{V} + \left(\frac{dm_i^g}{dt}\right)^{O} - \left(\frac{dm_i^g}{dt}\right)^{O} \tag{A.16a}$$

for $i = 1,\ldots,n-1$ and

$$\frac{dm_n^g}{dt} = \left(\frac{dm_n^g}{dt}\right)^{V} + \left(\frac{dm_n^g}{dt}\right)^{O}. \tag{A.16b}$$

Because it is assumed there is no water seepage out of the pores, any water loss in the i^{th} pore must be due to the vaporization of water; i.e.,

$$\left(\frac{dm_i^g}{dt}\right)^{V} = -\frac{dm_i^w}{dt}, i = 1,\ldots,n. \tag{A.17}$$

Thus, if we let

mass of gas (water vapor) generated in the i^{th} pore,

$m_i^{g,\mathrm{V}}(t) \equiv$ from time $t = 0$ to the present time t, as a result (A.18)

of the vaporization of water in that pore

then an integration of (A.17) yields

$$m_i^w(t) = -m_i^{g,\mathrm{V}}(t) + C. \tag{A.19}$$

More specifically,

$$m_i^{g,\mathrm{V}}(t) = \int_0^t \left(\frac{dm_i^g}{d\tau}\right)^{\mathrm{V}} d\tau \tag{A.20}$$

so that $m_i^{g,\mathrm{V}}(0) = 0$. Setting $t = 0$ in (A.19) yields, therefore, $C = m_i^w(0)$, in which case, by (A.19) and (A.20)

$$m_i^{\mathrm{w}}(t) = m_i^w(0) - \int_0^t \left(\frac{dm_i^g}{d\tau}\right)^{\mathrm{V}} d\tau. \tag{A.21}$$

Employing (A.21) in (A.2), we find for the effective mass, $m_i(t)$, of the (partially saturated) fibers comprising the lateral surface of the i^{th} pore

$$m_i^{\mathrm{w}}(t) = m_i^f + m_i^w(0) - \int_0^t \left(\frac{dm_i^g}{d\tau}\right)^{\mathrm{V}} d\tau. \tag{A.22}$$

We now introduce some additional notation; we let

$u_g^i(t) \equiv$ energy density, at time t, of the gas (water vapor) in the i^{th} pore (A.23a)

$u_l^i(t) \equiv$ energy density, at time t, of the water in the i^{th} pore (A.23b)

$v_g^i(t) \equiv$ specific volume, at time t, of the gas (water vapor) in the i^{th} pore (A.23c)

$v_l^i(t) \equiv$ specific volume, at time t, of the water in the i^{th} pore. (A.23d)

In (A.23c,d) we have $v_g^i(t) = 1/\rho_g^i(t)$ and $v_l^i(t) = 1/\rho_l^i(t)$ where $\rho_g^i(t)$ and $\rho_l^i(t)$ are, respectively, the water vapor and water densities in the i^{th} pore at time t. Because the sheet is now assumed to be in a supersaturated state, we have

$$u_g^i(t) = u_g(p_i(t)),\ u_l^i(t) = u_l(p_i(t)) \tag{A.24a}$$

$$v_g^i(t) = v_g(p_i(t)),\ v_l^i(t) = v_l(p_i(t)) \tag{A.24b}$$

for each i, $i = 1,\ldots,n$. We also set

$v_g^i(t) \equiv$ velocity of the gas (water vapor) in the i^{th} pore as it exits that pore through the capillary at the top of the pore of effective radius r_i and effective length l_i. (A.25)

Then, for $i = 1,\ldots,n$,

$$\left(\frac{dm_i^g}{dt}\right)^{\circ} = \pi r_i^2 \rho_g^i(t) v_g^i(t) \equiv \pi r_i^2 v_g^{-1}(p_i(t)) v_g^i(t). \tag{A.26}$$

By virtue of Darcy's law, for $i = 1,\ldots,n$, we have at time t the (approximate) relationship

$$\frac{p_{i-1}(t)-p_i(t)}{l_i}=-\frac{\mu_g}{K_i}v_g^i(t) \tag{A.27}$$

where μ_g is the viscosity of the water vapor, at the current saturation temperature, and K_i is the effective permeability of the top surface of the i^{th} pore. If we measure increasing distance through the thickness of the sheet from the top of the sheet, and use the experimentally observed fact that $p_{i-1}(t) > p_i(t)$, $i=1,\ldots,n$, $t>0$, then (A.27) yields $v_g^i(t) < 0$ thus indicating that the water vapor does, indeed, vent upward; i.e., in the direction of decreasing distance from the top of the sheet.

Solving (A.27) for $v_g^i(t)$ and substituting the result into (A.26) we obtain, for $i=1,\ldots,n$,

$$\left(\frac{dm_i^g}{dt}\right)^{\mathrm{O}}=-\frac{\pi K_i r_i^2}{\mu_g}\upsilon_g^{-1}(p_i(t))\left\{\frac{p_{i-1}(t)-p_i(t)}{l_i}\right\} \tag{A.28}$$

so that (A.13) is, indeed, satisfied. Also, by virtue of (A.14) and (A.28), with $i \to i+1$, for $i=1,\ldots,n-1$,

$$\left(\frac{dm_i^g}{dt}\right)^{\mathrm{I}}=\frac{\pi K_{i+1} r_{i+1}^2}{\mu_g}\upsilon_g^{-1}(p_{i+1}(t))\left\{\frac{p_i(t)-p_{i+1}(t)}{l_{i+1}}\right\} \tag{A.29}$$

and, for $i=n$, (A.15) holds. From (A.29), and the fact that $p_i(t) > p_{i+1}(t)$, for $i=1,\ldots,n-1$, we have $\left(\frac{dm_i^g}{dt}\right)^{\mathrm{I}} > 0$. Combining (A.28) and (A.29) with (A.12) we find that for $i=1,\ldots,n-1$

$$\frac{dm_i^g}{dt} = \left(\frac{dm_i^g}{dt}\right)^{V} + \frac{\pi K_{i+1} r_{i+1}^2}{\mu_g} \upsilon_g^{-1}(p_{i+1}(t)) \left\{ \frac{p_i(t) - p_{i+1}(t)}{l_{i+1}} \right\} \tag{A.30a}$$

$$- \frac{\pi K_i r_i^2}{\mu_g} \upsilon_g^{-1}(p_i(t)) \left\{ \frac{p_{i-1}(t) - p_i(t)}{l_i} \right\}$$

and for $i = n$

$$\frac{dm_n^g}{dt} = \left(\frac{dm_n^g}{dt}\right)^{V} - \frac{\pi K_n r_n^2}{\mu_g} \upsilon_g^{-1}(p_n(t)) \left\{ \frac{p_{n-1}(t) - p_n(t)}{l_n} \right\}. \tag{A.30b}$$

If $V_i^g(t)$ denotes that volume of the i^{th} pore which contains water vapor, at time t, then

$$V_i^g(t) = \pi R_i^2 H_i(t) \tag{A.31}$$

for $i = 1,\ldots,n$; therefore,

$$m_i^g(t) = \rho_g^i(t) V_i^g(t) \equiv \upsilon_g^{-1}(p_i(t)) V_i^g(t). \tag{A.32}$$

So

$$\frac{dm_i^g}{dt} = \frac{\upsilon_g(p_i(t)) \dfrac{dV_i^g}{dt} - V_i^g(t) \dfrac{d}{dt} \upsilon_g(p_i(t))}{\upsilon_g^2(p_i(t))}$$

or, in view of (A.31),

$$\frac{dm_i^g}{dt} = \frac{\pi R_i^2 \upsilon_g(p_i(t)) \dfrac{dH_i}{dt} - \pi R_i^2 H_i(t) \left.\dfrac{d\upsilon_g}{dt}\right|_{p_i} \dfrac{dp_i}{dt}}{\upsilon_g^2(p_i(t))}.$$

Finally, for $i = 1,\ldots,n$,

$$\frac{dm_i^g}{dt} = \pi R_i^2 \left\{ \frac{1}{v_g^i(t)} \frac{dH_i}{dt} - \frac{H_i(t)}{\left(v_g^i(t)\right)^2} \left. \frac{dv_g}{dp} \right|_{p_i} \frac{dp_i}{dt} \right\}. \tag{A.33}$$

By combining (A.33) with (A.30a,b) and solving for $\left(\frac{dm_i^g}{dt}\right)^V$ we obtain the following results:

(1) For $i = 1,\ldots,n-1$

$$\left(\frac{dm_i^g}{dt}\right)^V = \pi R_i^2 \left\{ \frac{1}{v_g^i(t)} \frac{dH_i}{dt} - \frac{H_i(t)}{\left(v_g^i(t)\right)^2} \left. \frac{dv_g}{dt} \right|_{p_i} \frac{dp_i}{dt} \right\} \tag{A.34a}$$

$$+ \frac{\pi K_i r_i^2}{\mu_g} v_g^{-1}(p_i(t)) \left\{ \frac{p_{i-1}(t) - p_i(t)}{l_i} \right\}$$

$$- \frac{\pi K_{i+1} r_{i+1}^2}{\mu_g} v_g^{-1}(p_{i+1}(t)) \left\{ \frac{p_i(t) - p_{i+1}(t)}{l_{i+1}} \right\},$$

(2) For $i = n$

$$\left(\frac{dm_n^g}{dt}\right)^V = \pi R_n^2 \left\{ \frac{1}{v_g^n(t)} \frac{dH_n}{dt} - \frac{H_n(t)}{\left(v_g^n(t)\right)^2} \left. \frac{dv_g}{dt} \right|_{p_n} \frac{dp_n}{dt} \right\} \tag{A.34b}$$

$$+ \frac{\pi K_n r_n^2}{\mu_g} v_g^{-1}(p_n(t)) \left\{ \frac{p_{n-1}(t) - p_n(t)}{l_n} \right\}.$$

We now set

$V_i^w(t) \equiv$ net volume, at time t, which is occupied by water in the i^{th} pore

(A.35a)

$V_i(t) \equiv$ net volume, at time t, of the i^{th} pore (A.35b)

$V_i^f \equiv$ net volume of the fibers comprising the surface of the i^{th} pore (A.35c)

Then, if $V_i^g(t)$, as given by (A.31), is that volume of the i^{th} pore, at time t, which contains water vapor,

$$V_i(t) = V_i^g(t) + V_i^w(t) + V_i^f \tag{A.36}$$

for $i = 1,\ldots,n$. Therefore, for each i,

$$\frac{dV_i}{dt} = \frac{dV_i^g}{dt} + \frac{dV_i^w}{dt}. \tag{A.37}$$

If, in lieu of (A.31), we express $V_i^g(t)$ as

$$V_i^g(t) = m_i^g(t)v_g^i(t) \tag{A.38a}$$

where $m_i^g(t)$ is given by (A.8) and, in a similar manner write

$$V_i^w(t) = m_i^w(t)v_l^i(t) \tag{A.38b}$$

then direct substitution into (A.37) yields

$$\frac{dV_i}{dt} = m_i^g \frac{dv_g^i}{dt} + v_g^i \frac{dm_i^g}{dt} + m_i^w \frac{dv_l^i}{dt} + v_l^i \frac{dm_i^w}{dt} \tag{A.39}$$

$$= m_i^g \frac{dv_g^i}{dt} + v_g^i \frac{dm_i^g}{dt} - v_l^i \left(\frac{dm_i^g}{dt}\right)^V + \left(m_i^w(0) - \int_0^t \left(\frac{dm_i^g}{d\tau}\right)^V d\tau\right)\frac{dv_l^i}{dt}$$

for $i = 1,\ldots,n$, where we have used (A.17) and (A.21). In order to proceed, we now introduce the following notation: We set

(1) For $i = 1,\ldots,n-1$

$$\left(\frac{dm_i^g}{dt}\right)^{\#} = \frac{\pi}{\mu_g}\left[K_{i+1} r_{i+1}^2 \upsilon_g^{-1}(p_{i+1}(t))\left\{\frac{p_i(t)-p_{i+1}(t)}{l_{i+1}}\right\}\right. \tag{A.40a}$$

$$\left. -K_i r_i^2 \upsilon_g^{-1}(p_i(t))\left\{\frac{p_{i-1}(t)-p_i(t)}{l_i}\right\}\right],$$

(2) For $i = n$

$$\left(\frac{dm_n^g}{dt}\right)^{\#} = -\frac{\pi}{\mu_g} K_n r_n^2 \upsilon_g^{-1}(p_n(t))\left\{\frac{p_{n-1}(t)-p_n(t)}{l_n}\right\} \tag{A.40b}$$

so that for $i = 1,\ldots,n$, $\left(\frac{dm_i^g}{dt}\right)^{\#}$ represents the net influx of vapor into the i^{th} pore due to venting. With the definitions in (A.40a,b), the relations (A.30a,b) may be combined so as to read

$$\frac{dm_i^g}{dt} = \left(\frac{dm_i^g}{dt}\right)^{\mathrm{V}} + \left(\frac{dm_i^g}{dt}\right)^{\#} \tag{A.41}$$

for $i = 1,\ldots,n$. Using (A.41) in (A.39) we now obtain, for $i = 1,\ldots,n$

$$\frac{dV_i}{dt} = \left\{ m_i^g \left.\frac{d\upsilon_g}{dp}\right|_{p_i} + \left(m_i^w(0) - \int_0^t \left(\frac{dm_i^g}{d\tau}\right)^{\mathrm{V}} d\tau \right) \left.\frac{d\upsilon_l}{dp}\right|_{p_i} \right\} \frac{dp_i}{dt} \tag{A.42}$$

$$+(\upsilon_g^i - \upsilon_l^i)\left(\frac{dm_i^g}{dt}\right)^{\mathrm{V}} + \upsilon_g^i \left(\frac{dm_i^g}{dt}\right)^{\#}.$$

We note that as a consequence of (A.34a,b) and the definitions (A.40a,b), $\left(\frac{dm_i^g}{dt}\right)^{\mathrm{V}}$ in (A.42) may be replaced by

$$\left(\frac{dm_i^g}{dt}\right)^{\mathrm{V}} = \pi R_i^2 \left\{ \frac{1}{v_g^i(t)} \frac{dH_i}{dt} - \frac{H_i(t)}{\left(v_g^i(t)\right)^2} \left.\frac{dv_g}{dp}\right|_{p_i} \frac{dp_i}{dt} \right\} - \left(\frac{dm_i^g}{dt}\right)^{\#} \tag{A.43}$$

for $i = 1,\ldots,n$.

The expression in (A.42) will no be employed in order to write down that special form of the first law of thermodynamics which holds in the i^{th} pore under the conditions which prevail when the sheet undergoes a rapid depressurization as it exits the nip. We first express the internal energy of the i^{th} pore, at time t, as

$$U_i(t) = m_i^w(t) u_l^i(t) + m_i^g(t) u_g^i(t) \tag{A.44}$$

Differentiating (A.44) with respect to t and, again, employing (A.17), (A.21), and the splitting (A.41), we obtain

$$\frac{dU_i}{dt} = \left\{ m_i^g \left.\frac{du_g}{dp}\right|_{p_i} + \left(m_i^w(0) - \int_0^t \left(\frac{dm_i^g}{d\tau}\right)^{\mathrm{V}} d\tau \right) \left.\frac{du_l}{dt}\right|_{p_i} \right\} \frac{dp_i}{dt} \tag{A.45}$$

$$+ (u_g^i - u_l^i) \left(\frac{dm_i^g}{dt}\right)^{\mathrm{V}} + u_g^i \left(\frac{dm_i^g}{dt}\right)^{\#}$$

for $i = 1,\ldots,n$, where $\left(\frac{dm_i^g}{dt}\right)^{\mathrm{V}}$ may be replaced by (A.43) and $\left(\frac{dm_i^g}{dt}\right)^{\#}$ is given by (A.40a,b). For the rate of working of the pressure field $p_i(t)$, in the i^{th} pore, in altering the net volume of that pore, we have

$$\frac{dW_i}{dt} = p_i(t) \frac{dV_i}{dt}, \tag{A.46}$$

for $i = 1,\ldots,n$, and by the First Law, if $\frac{dQ_i}{dt}$ is the rate of change of the heat content in the i^{th} pore, during depressurization of the sheet, as it exits the nip, then

$$\frac{dQ_i}{dt} = \frac{dU_i}{dt} + p_i(t)\frac{dV_i}{dt}. \tag{A.47}$$

However, the prevailing thermodynamic conditions in the sheet, under the prevailing circumstances, are such that $dQ_i/dt \cong 0$ so that (A.47) may be replaced with the approximate relationship

$$p_i(t)\frac{dV_i}{dt} = -\frac{dU_i}{dt}, \tag{A.48}$$

for $i = 1,\ldots,n$ .Combining (A.48) with (A.42) and (A.45), and simplifying, we are led to the following equations for $i = 1,\ldots,n$:

$$\left\{ m_i^g \left(\left.\frac{du_g}{dp}\right|_{p_i} + p_i \left.\frac{dv_g}{dp}\right|_{p_i} \right) + \left(m_i^w(0) - \int_0^t \left(\frac{dm_i^g}{d\tau}\right)^{\mathrm{V}} d\tau \right) \left(\left.\frac{du_l}{dp}\right|_{p_i} + p_i \left.\frac{dv_l}{dp}\right|_{p_i} \right) \right\} \frac{dp_i}{dt} \tag{A.49}$$

$$+ (u_g^i + p_i v_g^i)\left(\frac{dm_i^g}{dt}\right)^{\#} + \left\{ (u_g^i - u_l^i) + p_i(v_g^i - v_l^i) \right\} \left(\frac{dm_i^g}{dt}\right)^{\mathrm{V}} = 0$$

In (A.49), $\left(\frac{dm_i^g}{dt}\right)^{\#}$ is given by (A.40a,b) while $\left(\frac{dm_i^g}{dt}\right)^{\mathrm{V}}$ is given by (A.43), which is equivalent to (A.41) with $m_i^g(t)$ given by (A.31) and (A.32); i.e.,

$$m_i^g(t) = \pi R_i^2 v_g^{-1}(p_i(t)) H_i(t). \tag{A.50}$$

We now employ (A.41) in (A.49), so as to eliminate $\left(\frac{dm_i^g}{dt}\right)^{V}$, and obtain, for $i = 1,\ldots,n$, the equations

$$\left\{m_i^g\left(\left.\frac{du_g}{dp}\right|_{p_i} + p_i\left.\frac{dv_g}{dp}\right|_{p_i}\right) + \left(m_i^w(0) - m_i^g(t) + \int_0^t \left(\frac{dm_i^g}{d\tau}\right)^{\#} d\tau\right)\left(\left.\frac{du_l}{dp}\right|_{p_i} + p_i\left.\frac{dv_l}{dp}\right|_{p_i}\right)\right\}\frac{dp_i}{dt}$$

$$+\left\{(u_g^i + p_i v_g^i) - (u_g^i - u_l^i) + p_i(v_g^i - v_l^i)\right\}\left(\frac{dm_i^g}{dt}\right)^{\#} \qquad \text{(A.51)}$$

$$+\left\{(u_g^i - u_l^i) + p_i(v_g^i - v_l^i)\right\}\frac{dm_i^g}{dt} = 0$$

where $m_i^g(t)$ is given by (A.50), $\frac{dm_i^g}{dt}$ by (A.33), and we have used the fact that $m_i^g(0) = 0$. Using (A.33) in (A.51), as well as (A.50), and writing $\left(\frac{dm_i^g}{dt}\right)^{\#}$ in the form

$$\left(\frac{dm_i^g}{dt}\right)^{\#} = \Phi_i(p_{i-1}(t), p_i(t), p_{i+1}(t)) \qquad \text{(A.52)}$$

where Φ_i is given by the right-hand side of (A.40a) for $i = 1,\ldots,n-1$, and by the right-hand side of (A.40b) for $i = n$, we obtain, from (A.51), the equations

$$\left\{\frac{\pi R_i^2 H_i(t)}{v_g(p_i(t))}\left(\left.\frac{du_g}{dp}\right|_{p_i} + p_i\left.\frac{dv_g}{dp}\right|_{p_i}\right) - \pi R_i^2 H_i(t)\frac{1}{v_g^2(p_i(t))}\left.\frac{dv_g}{dp}\right|_{p_i}\left[(u_g^i - u_l^i) + p_i(v_g^i - v_l^i)\right]\right.$$

$$\left.+\left[\left(m_i^w(0) - \frac{\pi R_i^2 H_i(t)}{v_g(p_i(t))} + \int_0^t \Phi(p_{i-1}(\tau), p_i(\tau), p_{i+1}(\tau))d\tau\right)\left(\left.\frac{du_l}{dp}\right|_{p_i} + p_i\left.\frac{dv_l}{dp}\right|_{p_i}\right)\right]\right\}\frac{dp_i}{dt}$$

$$+\left\{\pi R_i^2 \frac{1}{v_g(p_i(t))}\left[(u_g^i - u_l^i) + p_i(v_g^i - v_l^i)\right]\right\}\frac{dH_i}{dt} \tag{A.53}$$

$$+\left\{(u_g^i + p_i v_g^i) - \left[(u_g^i - u_l^i) + p_i(v_g^i - v_l^i)\right]\right\}\Phi(p_{i-1}(t), p_i(t), p_{i+1}(t)) = 0$$

for $i = 1,\ldots,n$. We now introduce the following notation: We set

$$a(p) = \frac{1}{v_g(p)}\left[\frac{du_g}{dp} + p\frac{dv_g}{dp}\right] \tag{A.54a}$$

$$b(p) = \frac{1}{v_g^2(p)}\frac{dv_g}{dp}\left[(u_g(p) - u_l(p)) + p(v_g(p) - v_l(p))\right] \tag{A.54b}$$

$$c(p) = \frac{du_l}{dp} + p\frac{dv_l}{dp} \tag{A.54c}$$

$$d(p) = \frac{1}{v_g(p)}\left[(u_g(p) - u_l(p)) + p(v_g(p) - v_l(p))\right] \tag{A.54d}$$

$$e(p) = \left(u_g(p) - pv_g(p)\right) - \left[(u_g(p) - u_l(p)) + p(v_g(p) - v_l(p))\right]. \tag{A.54e}$$

The functional forms of $a(p), b(p), c(p), d(p)$, and $e(p)$ may be obtained from steam tables for given values of the saturation temperature. Using (A.54a)-(A.54e) in (A.53) enables us to write these equations in the following, more compact, form:

$$\left[\pi R_i^2\left(a(p_i(t)) - b(p_i(t))\right)H_i(t) + m_i^w(t)c(p_i(t))\right]\frac{dp_i}{dt} \tag{A.55}$$

$$+\pi R_i^2 d(p_i(t))\frac{dH_i}{dt} + e(p_i(t))\Phi_i(p_{i-1}(t), p_i(t), p_{i+1}(t)) = 0$$

where

$$m_i^w(t) = m_i^w(0) - \pi R_i^2 \frac{H_i(t)}{v_g(p_i(t))} + \int_0^t \Phi_i(p_{i-1}(\tau), p_i(\tau), p_{i+1}(\tau))\, d\tau \tag{A.56}$$

with

$$\Phi_i = \frac{\pi}{\mu_g}\left[K_{i+1} r_{i+1}^2 v_g^{-1}(p_{i+1}) \left\{ \frac{p_i - p_{i+1}}{l_{i+1}} \right\} - K_i r_i^2 v_g^{-1}(p_i) \left\{ \frac{p_{i-1} - p_i}{l_i} \right\} \right] \tag{A.57a}$$

for $i = 1,\ldots,n-1$, while for $i = n$,

$$\Phi_n = -\frac{\pi}{\mu_g} K_n r_n^2 v_g^{-1}(p_n) \left\{ \frac{p_{n-1} - p_n}{l_n} \right\}. \tag{A.57b}$$

The n equations (A.55) for $p_i(t), H_i(t)$ are a direct consequence of the reduced form (A.48) of the First Law (A.47); these equations must be coupled to the n equations (A.1) where $m_i(t)$ is given by (A.2), $k_i(t)$ has the functional form (A.3), $h_i(t)$ is defined by (A.4), and $\mathcal{F}_i(t)$ by (A.5). Employing (A.2), (A.4), and (A.5) in (A.1) we find that these equations have the equivalent form

$$m_i^f \frac{d^2 H_i}{dt^2} + \frac{d}{dt}\left(m_i^w(t) \frac{dH_i}{dt} \right) + k_i(t) H_i(t) = k_i(t) H_i(0) + \pi (R_i^2 - r_i^2) p_i(t) \tag{A.58}$$

for $i = 1,\ldots,n$, where $m_i^w(t)$ is given by (A.56), (A.57a,b) and $k_i(t)$ has the form indicated in (A.3). Associated with the system of $2n$ equations (A.55), (A.58) is the specification of the function $p_0(t)$ and the $3n$ initial conditions

$$p_i(0) = p_i^0, \;\; H_i(0) = H_i^0, \;\; \dot{H}_i(0) = 0 \tag{A.59}$$

for $i = 1,\ldots,n$.

It is a straightforward matter to see that the system consisting of (A.55) and (A.58) may be written in the form

$$\alpha_i(t)\frac{dp_i}{dt}+\beta_i(t)\frac{dH_i}{dt}=\gamma_i(t), \tag{A.60a}$$

$$m_i^f\frac{d^2H_i}{dt^2}+\frac{d}{dt}\left(m_i^w(t)\frac{dH_i}{dt}\right)=-k_i(t)(H_i(t)-H_i(0))+\mathcal{A}_i p_i(t). \tag{A.60b}$$

In (A.60a) and (A.60b),

$$\alpha_i(t)\equiv\pi R_i^2\left[a(p_i(t))-b(p_i(t))\right]H_i(t)+m_i^w(t)c(p_i(t)) \tag{A.61a}$$

$$=\pi R_i^2\left\{\left[a(p_i(t))-b(p_i(t)\right]-\frac{c(p_i(t))}{v_g(p_i(t))}\right\}H_i(t)$$

$$+\left\{m_i^w(0)+\int_0^t\Phi_i(p_{i-1}(\tau,)p_i(\tau),p_{i+1}(\tau))d\tau\right\}c(p_i(t))$$

with $a(p), b(p), c(p)$, and Φ_i given, respectively, by (A.54a,b,c) and (A.57a,b). Also,

$$\beta_i(t)=\pi R_i^2 d(p_i(t)) \tag{A.61b}$$

$$\gamma_i(t)=-e(p_i(t))\Phi_i(p_{i-1}(t),p_i(t),p_{i+1}(t)) \tag{A.61c}$$

$$\mathcal{A}_i=\pi(R_i^2-r_i^2) \tag{A.61d}$$

where $d(p), e(p)$ are given by (A.54d,e) and $k_i(t), m_i^w(t)$ are given by the functional relationship (A.3) and equation (A.56), respectively.

Remarks: When $p_i(t), H_i(t)$, $i=1,\ldots,n$, $t>0$, have been determined, as solutions of the initial value problem (A.60a,b), (A.59), subject to the specification of the pressure profile $p_0(t)$, at the top of the sheet, (A.50) and (A.56) may be used to compute both

the mass of water, at time t, in the fibers comprising the later surface of the i^{th} pore and the mass of water vapor in the i^{th} pore at time t.